UNIVERSITY OF TURKU

Computational Analysis of Triply Periodic Minimal Surface Based Honeycomb Structures Under Impact Loading

Faculty of Technology, Department of Mechanical and Materials Engineering

Master's thesis

Author: Nimantha Sandaruwan Meneripitiyage Don

Supervisor: Asim Rashid

Number of pages: 104 pages

21.05.2026
Turku

Abstract

Balancing lightweight structural design with adequate crashworthiness performance remains a fundamental engineering challenge in automotive crash management. Conventional crash bars exhibit inherent limitations under dynamic loading, including localised deformation and inconsistent force transmission, motivating research into alternative cellular architectures. This thesis presents a computational investigation comparing two TPMS-derived 2D crash bar architectures, namely the G-Honeycomb and P-Honeycomb, against a conventional hollow cylindrical crash bar. Finite element models were developed in SolidWorks and analysed using Abaqus/Explicit, with all configurations assigned AA6061-T6 aluminium alloy properties via a rate-independent elastic-plastic constitutive model. Simulations were conducted at impact velocities of 40 km/h and 60 km/h under identical boundary conditions. The G-Honeycomb produced the highest crush force efficiency and the most stable, broadly distributed deformation pattern across both test velocities. The P-Honeycomb generated a substantially higher initial peak force and exhibited a reduction in energy absorption with increasing velocity, consistent with a velocity-induced change in collapse mechanism. The conventional crash bar demonstrated concentrated plastic hinge formation with limited structural participation, resulting in comparatively low force efficiency that deteriorated further at higher velocity. These results suggest that the G-Honeycomb represents a viable alternative for automotive crash bar applications and highlight the importance of dynamic validation when evaluating TPMS-derived 2D structures intended for impact-critical engineering applications.

Keywords: TPMS-derived prismatic structures, G-Honeycomb, P-Honeycomb, crashworthiness, specific energy absorption, crush force efficiency, finite element analysis, Abaqus/Explicit, AA6061-T6, automotive crash management

USE OF AI IN THESIS

I have used AI tools in my thesis:

☐ No ☒ Yes

The AI tools used in my thesis and the purpose of their use has been described below:

Names of the tools and versions: Scopus AI Elicit Claude AI (claude.ai, Sonnet 4.6)

Purpose of the use: Scopus AI was used to support the literature search process by identifying and filtering relevant academic sources on TPMS structures, crashworthiness, and finite element analysis. Elicit was used to summarize and compare research papers during the drafting of literature review sections on TPMS structures, dynamic impact behaviour, and crashworthiness performance. Claude AI was used to assist in revising thesis text based on supervisor comments and to generate schematic reference diagrams which were subsequently redrawn by the author.

Parts in which AI was used:

- Literature search: Scopus AI was used to discover and filter relevant sources for the literature review.
- Literature review writing: Elicit was used to summarize and compare research papers during the drafting of sections on TPMS structures, energy absorption metrics, and crashworthiness performance.
- Figure generation: Claude AI was used to generate schematic reference diagrams for Sections1.2, subsequently redrawn by the author.

I am aware that I am totally responsible for the entire content of the thesis, including the parts generated with AI assistance, and accept the responsibility for any violations of the ethical standards of publications.

Table of contents

GLOSSARY

Crush Force Efficiency	(CFE)
Energy Absorption	(EA)
Equivalent Plastic Strain	(PEEQ)
Fused Deposition Modelling	(FDM)
Head Injury Criterion	(HIC)
Initial Peak Crushing Force	(PCF)
Laser Powder Bed Fusion	(L-PBF)
Mean Crushing Force	(MCF)
Specific energy absorption	(SEA)
Specific Energy Absorption Volume Efficiency	(SEAV)
Triply Periodic Minimal Surface	(TPMS)

1 INTRODUCTION

1.1 Crashworthiness and Lightweight Structural Design

Vehicle structural performance during a collision is explained through the concept of crashworthiness engineering, a discipline that emerged as a formal field of study in the second half of the twentieth century in response to the escalating human and road traffic accidents. According to (*Global Status Report on Road Safety 2023*, 2023), road traffic crashes cause approximately 1.19 million deaths annually worldwide and are the leading cause of death among individuals aged 5/29 years. (European Commission, 2023) recorded that within European union, 20 640 road fatalities were recorded in 2022, with a considerable proportion of these involving frontal and rear impact collisions at speeds consistent with urban and peri urban traffic conditions. Such collisions frequently occur within the velocity range of 40/60 km/h, which is therefore selected as the focus of this study. The economic cost of road crashes in the EU is estimated at approximately 280 billion euros per year, representing nearly 2% of gross domestic product. These costs include emergency response services, medical treatment, vehicle repair and productivity losses (European Commission / European Road Safety Observatory, 2023).

In response to these safety and economic challenges, regulatory bodies have developed crash testing procedures to define the minimum structural performance required for vehicles. In Europe, the primary standards include ECE Regulations No 42, which governs low speed bumper performance at impact velocities of 4 km/h and 2,5 km/h in pendulum and barrier test. More severe crash conditions are assessed through Euro NCAP protocols, including the frontal offset deformable barrier test at 64 km/h and the full width rigid barrier test at 50 km/h. Similarly, the Insurance Institute for Highway safety applies moderate overlap and small overlap frontal crash tests at 64,4 km/h. These standards collectively define a crash management performance range approximately 40-65 km/h that the front crash management system. This system generally comprises of the bumper beam, crash bars, and other energy absorbing component designed to dissipate impact energy before it reaches the passenger compartment. Accordingly, the selected impact velocities of 40 km/h and 60 km/h used in this thesis represents suitable lower and upper bounds of the urban crash management regime.

One of the main challenges in the engineering of crash management is the simultaneous requirement for low structural mass and high energy absorption capacity. Increasing environmental regulations and market expectations have intensified the demand for lightweight vehicles with reduced CO_2 emissions. The European Union's regulation 2019/631 mandates a fleet average CO2 target of 95 g/km for new passenger cars, with further reductions to 55% below 2021 levels by 2030 and zero tailpipe emissions by 2035. Every kilogram of mass removed from a vehicle reduces fuel consumption and reduces lifecycle emissions. However, mass reduction introduces a significant engineering limitation in crash safety. The crash management system which consists of front and rear energy absorbing structures such as bumper beams, crash bars and longitudinal members represents approximately 8-12% of the total structural mass of a vehicle, must absorb substantial impact energy without proportional reductions in its size or mass. Balancing between lightweight design and crashworthiness performance is the core engineering problem that motivates the search for architected cellular materials with enhanced specific energy absorption.

1.2 Conventional Honeycomb Crash Management Systems

The front crash management system of a modern passenger vehicle includes a transverse bumper beam made from high strength aluminium or steel, that is connected to the longitudinal members of the vehicle through crash bars. Crash bars are short, prismatic structures designed to collapse progressively to dissipate energy in a controlled manner during low to moderate speed frontal impacts. In higher end vehicles and battery electric vehicles with greater front end packaging availability, increase crush stroke is required that cannot be achieved by the standard bumper beam and crash bar arrangement. A supplementary cellular energy absorber is therefore installed between the bumper beam and crash bars to increase the effective crush stroke and enhance overall energy absorption capacity of the front crash management system. Aluminium hexagonal honeycomb structures are commonly selected for this purpose due to the predictability of its collapse behaviour and its high specific stiffness relative to other cellular structures.

The performance of a conventional aluminium honeycomb crash bar is characterised by initial peak crushing force (PCF), mean crushing force (MCF), and crush force efficiency (CFE), metrics defined in Chapter 2. A well-designed aluminium honeycomb

crash bar typically achieves CFE values of 0,65-0,85 and Specific Energy Absorption (SEA) values of 10-25 kJ/kg depending on cell density, wall thickness and alloy selection.

While honeycombs have been shown to achieve optimal energy absorption in axial tests, their performance drops significantly at oblique test angles. Another limitation of hexagonal honeycombs is that their mechanical properties are governed by a small number of discrete parameters, making it challenging to achieve a smooth gradient and density. Furthermore, there is a notable research gap on their dynamic material behaviour of honeycombs for the 40-60 km/h range, which is the typical range for the urban crashes.

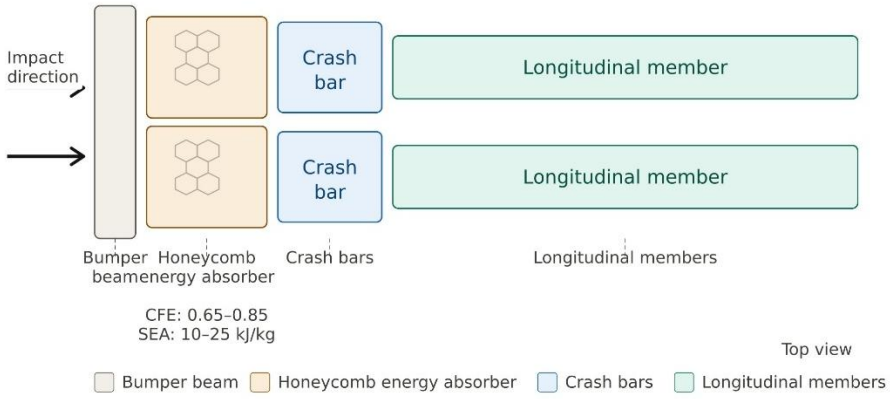

Figure 1 - Conventional honeycomb crash management system layout (top view)

1.3 TPMS-Derived Prismatic Structures

Triply Periodic Minimal Surface (TPMS) structures are a class of mathematically defined geometries that repeat periodically in three independent spatial directions and maintain zero mean curvature at every point on their surface (Hossain et al., 2025). In this study, however, TPMS lattices periodic in all three spatial dimensions are not employed. Instead, 2D cross-sectional profiles derived from TPMS level-set equations are extruded longitudinally to produce the crash bar core geometries studied here. These TPMS-derived prismatic structures retain the smooth, continuous wall profiles of the parent surface while remaining distinct from volumetric TPMS lattices. The smooth, continuous wall profiles distribute stress more gradually along the structure compared to conventional geometries with sharp node connections and straight struts,

reducing localised stress concentrations (Guo et al., 2019; Hossain et al., 2025). This continuity makes the profiles more resistant to premature local buckling, resulting in a more stable and incremental failure process (Yin et al., 2020).

Among the different TPMS topologies, the Schwarz Primitive (P), Schoen Gyroid (G), and Schwarz Diamond (D) are the most widely studied in the engineering applications. But the focus of this thesis is on the Primitive and Gyroid topologies. The differences of these topologies strongly influence stiffness, strength, and energy absorption, which are key parameters for crashworthiness performance.

TPMS-derived 2D structures, generated by extruding TPMS level-set cross-sections, have emerged as a promising class of crash bar core geometries. Their smooth, continuous wall profiles produce more uniform stress distribution compared to conventional hexagonal honeycombs with sharp node junctions. This is considered an advantage over traditional honeycombs which perform differently depending on load orientation. Advances in additive manufacturing have made using these complex geometries in engineering-grade materials increasingly practical. Quasi-static studies further support their potential, showing energy absorption comparable to honeycombs and better performance under off-axis loading conditions.

Experimental testing across a wide range of design parameters is both resource intensive and time consuming. This study therefore adopts a finite element modelling approach using Abaqus/Explicit, based on previously validated methodologies. This allows for efficient evaluation of structural response under crash relevant loading conditions.

1.4 Identification of the Research Gap

Despite significant growth in TPMS research during the past decade, five principal gaps remain between existing knowledge and the level of understanding required for engineering deployment of TPMS-derived 2D crash bars as alternatives to conventional honeycomb crash bars in automotive applications. These gaps are central to determining whether TPMS-inspired honeycombs specifically the G-Honeycomb and P-Honeycomb studied here, can be reliably considered as viable alternatives to conventional aluminium honeycomb crash bars.

A review of the published literature indicates that no published study has evaluated G-Honeycomb and P-Honeycomb topologies under identical conditions at impact velocities representative of automotive crash testing, nor has any work directly benchmarked a TPMS-derived prismatic crash bar against a conventional aluminium honeycomb crash bar under equivalent automotive boundary conditions. Whether a topology-dependent interaction exists between structural performance and impact velocity within the 40-60 km/h range also remains unexamined. TPMS crashworthiness data for AA6061-T6, which is the wrought aluminium alloy most used in extruded automotive crash bars, are similarly scarce in the literature. Finally, the computational TPMS impact literature lacks systematic field-level analysis of stress and plastic strain distributions, limiting the ability to explain topology-dependent performance differences or guide design optimisation.

Collectively, these five gaps define the scope and motivation of this study. A full review of the supporting evidence for each gap is provided in Chapter 2.

1.5 Research Objectives

This study aims to address the five research gaps identified above using a systematic computational approach. The scope of the work is defined by these objectives.

The first objective is to develop finite element models of the G-Honeycomb, P-Honeycomb, and conventional hexagonal honeycomb crash bar geometries manufactured from AA6061-T6 aluminium alloy using Abaqus/Explicit. Model validation is carried out against published experimental results for comparable TPMS structures tested under equivalent loading conditions.

The second objective is to evaluate and compare the crashworthiness performance of the three architectures under identical boundary conditions, using geometries of identical external dimensions but differing internal topology and mass, at impact velocities of 40 km/h and 60 km/h. Specific Energy Absorption (SEA) is used as the primary mass-normalised performance metric to account for differences in structural mass.Performance is evaluated by total energy absorption, specific energy absorption, peak crushing force, mean crushing force, and crash force efficiency.

The third objective of this study is to examine the deformation behaviour of both G-Honeycomb and P-Honeycomb crash bars under crash simulation conditions. The

analysis is topology focused and covers von Mises stress development, equivalent plastic strain progression, and how energy absorption is spatially distributed at selected impact intervals.

The fourth objective is to evaluate the velocity-topology performance interaction by comparing the crashworthiness metric rankings of the G-Honeycomb, P-Honeycomb, and conventional honeycomb at 40 km/h vs 60 km/h, and to test whether the quasi-static performance hierarchy is preserved, amplified, or reversed at automotive-relevant impact velocities. The fifth objective is to provide an engineering assessment of the viability of TPMS-derived 2D crash bars in automotive bumper systems, based on quantitative performance margins across all studied metrics at both impact velocities.

1.6 Research Questions

The research objectives above give rise to four specific research questions that the study is designed to answer.

1. Which TPMS-derived 2D structure (G-Honeycomb or P-Honeycomb) exhibit superior crashworthiness performance, as measured by SEA, CFE, and PCF, at impact velocities of 40 km/h 60 km/h?

2. Does the relative performance ranking between the G-Honeycomb and P-Honeycomb change as a function of impact velocity between 40 km/h and 60 km/h, and if so, in which direction and by what magnitude?

3. By what quantitative margin do the TPMS-derived 2D crash bars (G-Honeycomb and P-Honeycomb) outperform or underperform the conventional aluminium honeycomb crash bar in terms of SEA, PCF, and CFE at each of the two test velocities?

4. What deformation mechanisms, identifiable through stress and plastic strain field analysis, underlie the observed differences in crashworthiness performance between the G-Honeycomb and P-Honeycomb, and how do these mechanisms evolve with increasing impact velocity?

1.7 Scope and Delimitations

The scope of this study is defined by the intersection of the identified research gaps, the available computational tools. The following inclusions and exclusions set the study boundaries.

The study scope includes G-Honeycomb and P-Honeycomb crash bar cores, generated from 2D level-set cross-sections derived from TPMS equations and extruded longitudinally, at a uniform relative density of approximately 0.25, modelled as homogeneous specimens for controlled comparison, a hexagonal aluminium honeycomb crash bar of equivalent external bounding dimensions as the performance benchmark, with mass differences between configurations addressed through SEA-based normalisation, AA6061-T6 material behaviour represented by a Johnson-Cook elasto-viscoplastic constitutive law without fracture initiation, explicit dynamic FEA in Abaqus/Explicit at impact velocities of 40 km/h and 60 km/h with a 1000 kg rigid impactor, and crashworthiness evaluation through EA, SEA, PCF, MCF, CFE, and densification strain, supported by deformation sequence and stress field analysis.

The following are excluded from the scope of this study. Experimental fabrication and physical impact testing, functionally graded or hybrid TPMS architectures, multi axial, oblique or lateral loading, thermal effects and adiabatic heating, fatigue and cyclic deformation, full vehicle system level simulation and fracture or ductile damage initiation modelling. These exclusions are acknowledged as limitations and are identified as key directions for future work in chapter 6.

This study also assumes idealised geometries without manufacturing defects. As shown by (Bahrami Babamiri et al., 2020) and (Özen et al., 2024), such defects may reduce performance by 10-25%. Results therefore represent upper bound estimates.

1.8 Thesis Structure

This thesis is structured into six chapters. Chapter 2 reviews energy absorbing cellular structures, TPMS behaviour under different loading conditions, comparisons with honeycomb structures, and numerical modelling approaches, concluding with the identification of five research gaps. Chapter 3 describes the computational methodology, including mathematical definition and CAD generation of G-Honeycomb,

P-Honeycomb, and conventional honeycomb geometries, material modelling of AA6061-T6 aluminium alloy, FE model setup, loading conditions, and validations. Chapter 4 presents simulation results, while Chapter 5 provides a detailed discussion of the results, interpreting deformation behaviour, comparing with the literature and evaluating implications for automotive crash management systems. Chapter 6 concludes the thesis by addressing the research questions, summarising main findings and contributions and outlining future work.

2 LITERATURE REVIEW

2.1 Energy Adsorption Metrics and Fundamentals

Crashworthiness engineering addresses the ability of structures and systems to safeguard occupants and critical components during impact events through controlled dissipation of kinetic energy into mechanisms such as plastic deformation, fracture, and heat generation. Since the emergence of structural energy management concepts in automative design during the mid twentieth century, crashworthiness engineering has expanded from simple thin-walled tubes to highly architected cellular materials designed for specific loading conditions. Although notable advances have been made, the central design problem remains unresolved. Maximizing energy absorption efficiency and minimizing peak force transmission are competing demands, and finding the right balance between them continues to drive research in this area.

Several performance indicators are commonly used to evaluate crashworthy structures. EA measures the total energy absorbed during impact, calculated as the integral of the force-displacement curve in joules. SEA normalizes EA by structural mass, providing a mass-efficiency metric in kJ/kg making it useful for lightweight design comparisons. PCF indicates the highest force reached during impact, expressed in kilonewtons, and is a key safety parameter. Regulations such as FMVSS 208 set deceleration limits that effectively define acceptable PCF limits.

The crush force efficiency (CFE) is defined by the ratio between the MCF to PCF. It indicates how stable the deformation behaviour is throughout the crushing process. MCF is derived by dividing EA by the total crush displacement. Densification strain (εD) defines the transition to full compaction where stiffness increases significantly. Structures with a higher εD are preferred, as they maintain effective energy absorption over a longer deformation range.

In a study by (Shinde et al., 2022), failure mechanisms in AlSi10Mg cellular structures were examined under quasi static compression. This study was aimed to understand their relationship with energy absorption. TPMS lattice variants including the Gyroid topology, outperformed the other architectures overall. Their curved wall geometry supported gradual deformation than sudden fracture, producing more stable plateau behaviour and densification. The study identified geometry and relative density as key

factors shaping collapse mode, including buckling, shear banding, or wall folding. The authors concluded that TPMS structures are well suited for crash energy management applications.

Mass based metrics have traditionally dominated crashworthiness evaluation, but specific energy absorption by volume (SEAV) is increasingly used as a complementary measure. Unlike SEA, SEAV normalizes energy absorption against external structural volume rather than mass. In automotive design, where packaging space is often as constrained as weight, this distinction can provide a more practical basis for comparison, especially in bumper systems and front-end crumple zones. The difference becomes clearer when structures of varying densities are compared. A low-density TPMS may yield a high SEA due to its reduced mass, yet its SEAV can remain modest if the absolute energy absorbed per unit volume is low. This study therefore considers both metrics where available in the literature, enabling a more complete assessment of structural performance.

2.2 Conventional Honeycomb Structures in Automotive Crash Management

2.2.1 Structural Mechanics of Hexagonal Honeycombs

In energy absorption studies, the hexagonal honeycomb is widely used due to its predictable axial compression response. Deformation begins at wall junctions through plastic hinge formation and develops progressively through the structure. The response typically follows a clear pattern of elastic deformation, peak force, a stable plateau, and final densification.

The plateau flatness, quantified by CFE, generally lies between 0,6-0,85 for well-designed hexagonal aluminium honeycombs under axial loading. The exact values depend on cell wall aspect ratio, geometry, material strain hardening, and behaviour of the parent material.

The theoretical framework for honeycomb mechanics was established in (“L.J. Gibson and M.F. Ashby, Cellular Solids,” 1989), where scaling laws that relate relative density to elastic modulus, plastic collapse stress, and energy absorption capacity were derived. For a regular hexagonal honeycomb with cell wall thickness t and cell edge length l, the relative density is given by $\frac{\rho}{\rho_s} = \frac{2t}{I\sqrt{3}}$. As summarised by (Ashby, 2006),

the governing deformation mode determines the scaling behaviour. Bending dominated architectures follow $E^* \propto \left(\frac{\rho}{\rho s}\right)^2$ and $\sigma^* pl \propto \left(\frac{\rho}{\rho s}\right)^{1,5}$, whereas stretch dominated structures exhibit a linear dependence on relative density. These relationships have been widely validated for metallic honeycombs and remains a useful design guidance for preliminary sizing. However, they do not account for effects such as manufacturing induced imperfections or dynamic loading conditions.

2.2.2 Limitations of Conventional Honeycombs

Conventional hexagonal honeycombs, while highly effective under axial compression, are associated with several limitations that reduce their applicability in realistic crash loading conditions. A key limitation of conventional honeycomb structures is their strong mechanical anisotropy. Although they perform well under axial loading, energy absorption capacity drops noticeably when loads are applied in the transverse or oblique direction. In practice, automotive crash events rarely involve purely axial loading. Oblique, pole, and rear-offset impacts introduce shear and lateral forces. Honeycomb structures are not well suited to handle these conditions, making their sensitivity to loading direction a major limitation in crashworthiness design.

Loading rate strongly influences the progressive folding response of these structures. At quasi-static rates, deformation is stable and consistent, yielding repeatable force-displacement behaviour. Once impact velocities exceed around 30 to 50 m/s, cell wall inertia begins to influence fold formation. Micro-inertia effects then enhance plateau stress dynamically, which can increase the force transmitted through the structure. In the velocity range of 40-60 km/h corresponding to automotive regulatory testing, the dynamic response of conventional honeycombs is not well documented. Furthermore, no systematic dataset documents how PCF and SEA vary across this range. This gap is identified as one of the main motivations for this study.

Another limitation of conventional honeycombs is their poor adaptability to functionally graded or hybrid designs. Unlike TPMS structures, conventional honeycombs depend on discrete geometric changes in geometries. The manufacturability of graded conventional honeycombs is significantly more challenging than producing uniform designs, thereby limiting their industrial adoption despite reported performance benefits in the literature.

2.3 Triply Periodic Minimal Surface (TPMS) Structures and TPMS-Derived 2D Honeycombs

2.3.1 Mathematical Foundations

A TPMS is a surface that repeats periodically in three independent spatial directions while maintaining zero mean curvature at every point. The zero mean curvature condition requires that the principal curvatures satisfy $K_1 + K_2 = 0$ across the entire surface, which means that the surface locally achieves minimum area under the geometric constraints of its topology and periodic repetition. TPMS structures are represented using implicit level set functions of the form $F\ (x, y, z) = c$, where, F is a sum of trigonometric functions with periods equal to the unit cell dimensions, and the constant c defines the isovalue at which the surface is extracted, thereby controlling wall thickness and the relative density of the resulting cellular solid. The two most widely studied TPMS geometries in the engineering literature are the Schwartz Primitive (P-surface) and the Schoen Gyroid (G-surface), whose level set approximations are given by:

$$\textbf{Schwartz Primitive } (\mathbf{P}) : \cos(\mathrm{x}) + \cos(\mathrm{y}) + \cos(\mathrm{z}) = \mathrm{c}$$

$$\textbf{Scheon Gyroid } (\mathbf{G}) : \sin(\mathrm{x})\cos(\mathrm{y}) + \sin(\mathrm{y})\cos(\mathrm{z}) + \sin(\mathrm{z})\cos(\mathrm{x}) = \mathrm{c}$$

For CAD generation, a thickened sheet network solid is extracted by replacing the equality with an inequality of the form $-t \leq F(x,y,z) \leq t$, where t controls wall thickness and therefore relative density.

These expressions are practical trigonometric approximations of the exact minimal surfaces rather than closed-form analytical solutions. The Gyroid, first described mathematically by Alan Schoen in a NASA technical report in 1970, has no known closed-form analytical expression, but the level set approximation is widely used in engineering applications because it is computationally tractable and reproduces the key topological features of the true surface with high fidelity.

The two topologies differ substantially in their structural character. The Primitive surface has cubic symmetry and forms a structure with two interpenetrating open channels aligned with the principal axes, giving it a relatively high proportion of walls oriented perpendicular to the loading direction. The Gyroid surface has a chiral,

bicontinuous topology with no straight channels in any direction, a feature that distributes stress more uniformly and is considered responsible for its resistance to shear band localisation.

From level set equations, two different solid architectures can be formed. In a sheet-network TPMS, material is distributed as a thin shell centred on the zero-level surface, forming two interconnected voids. In a skeletal-network TPMS, the solid phase instead occupies one of the two volumes separated by the surface, producing a strut-like geometry. Sheet network architectures are widely studied for crashworthiness applications due to their higher surface area, more uniform wall thickness, and greater resistance to localised buckling. In this thesis, the three-dimensional TPMS level-set equations described above are applied in a reduced form: a 2D cross-sectional profile is extracted at a fixed parameter plane and extruded longitudinally to produce the crash bar core. The resulting TPMS-derived 2D structures retain the smooth wall profiles and topological character of the parent surface but are distinct from full three-dimensional TPMS lattice implementations.

2.3.2 Relative Density and Functional Grading

In TPMS architectures, relative density can be varied spatially by, modifying the level set constant c cross the structure. This enables functionally graded designs with smooth, mathematically defined density gradients, avoiding stress concentrations from discrete geometric changes.(Yu et al., 2019) showed this experimentally using linearly graded Schwarz Primitive structures made from stereolithography. The graded structures collapsed in a layer-by-layer manner, converting the flat plateau into a progressively increasing mean force. Total energy absorption improved by approximately 50% over the uniform equivalent. This confirmed functional grading as a practical strategy for enhancing TPMS crashworthiness.

Instead of exhibiting a single stress plateau, the graded structures displayed two distinct plateau regions occurring at different stress levels. Collapse initiated in the thinner section and subsequently propagated into the thicker region in a sequential manner. Both the magnitude of the stress levels and the duration of each plateau were found to be tunable by modifying the wall thickness ratio as well as the position of the barrier layer. This demonstrates that a single architecture can incorporate multiple force-displacement responses within a continuous structural design. Such dual-stage

energy absorption behaviour provides a level of design flexibility that is not achievable in homogeneous structures and is particularly advantageous for crashworthiness applications that require progressive or staged energy dissipation.

2.3.3 Fabrication Methods and Their Influence on mechanical Performance

The practical manufacture of TPMS structures for engineering applications is presently dominated by powder bed fusion additive manufacturing processes, particularly laser powder bed fusion (L-PBF), also commonly referred to as selective laser melting (SLM) or LPBF. This process enables the layer-by-layer solidification of metallic powders into complex geometries with sufficient resolution to replicate TPMS wall thickness in the range of 0,3-1,5 mm. Polymer TPMS structures are typically fabricated by fused deposition modelling (FDM) or stereolithography (SLA).

(Shinde et al., 2022) studied six cellular structure types, including Gyroid and Schwarz-Primitive TPMS, fabricated from AlSi10Mg by L-PBF, and related their failure mechanisms to energy absorption metrics, finding that TPMS structures, including Gyroid, outperformed beam lattice and auxetic structures across multiple performance criteria.

The choice of fabrication method significantly influences TPMS mechanical performance. (Özen et al., 2024) compared AlSi10Mg Gyroid structures (full three-dimensional TPMS lattices, distinct from the G-Honeycomb studied in this thesis) produced by investment casting and L-PBF, finding that L-PBF structures exhibited approximately 150% greater specific energy absorption, while cast structures provided around 25% higher crush force efficiency due to lower peak stresses at the onset of crushing.Cast structures deformed by ductile plastic folding whereas printed structures exhibited brittle fracture, differences attributed to the finer and more homogeneous microstructure produced by rapid -PBF solidification compared to the coarser dendritic structure of cast parts.

Geometric imperfections inherent to L-PBF also cause as-built structures to deviate from idealized CAD geometry. (Bahrami Babamiri et al., 2020) showed using XCT that strut diameters in SLM fabricated Inconel 718 lattices were 10-20% larger than nominal, with joint fillet radii nearly twice the design values, causing as built relative density to exceed the CAD value by a factor of approximately 1,1. Simulations based

on idealized geometry consequently underpredicted experimental stiffness and flow stress, and the study further identified that L-PBF induced plastic anisotropy, manifesting as different yield strengths under tension versus compression, cannot be captured by conventional isotropic plasticity models.

2.4 Mechanical Performance of TPMS Structures Under Quasi-Static Loading

2.4.1 Compressive Response and Energy Absorption

The compressive behaviour of full three-dimensional sheet-based TPMS lattices under quasi-static loading, as reported in the literature, is characterised by four stress-strain response stages: linear elasticity, elastic-plastic transition, plateau deformation, and densification with rapidly rising stress as cell walls contact each other (Maskery et al., 2017; Zhang et al., 2024). These findings provide indicative benchmarks for the TPMS-derived 2D structures investigated in this thesis, though direct equivalence cannot be assumed due to the geometric differences between extruded 2D cross-sections and volumetric lattice architectures.

Literature commonly shows that sheet-based TPMS lattices outperform equivalent density strut based lattices in SEA. (Maskery et al., 2017) found that heat treated AlSi10Mg double gyroid lattices produced by selective laser melting absorbed about three times more energy per unit volume than BCC lattices at a volume fraction of 0,22 up to 50% strain. The authors connected this improved mechanical behaviour to the continuous shell morphology of the gyroid. This geometry improved stress distribution and delayed local cracking and diagonal shear localization seen in as-built conditions.

The role of post-build heat treatment significantly changed the response. Untreated specimens failed at strains of just 0.14, while heat-treated counterparts exhibited an extended, nearly flat plateau consistent with Gibson-Ashby behaviour. This result shows that TPMS mechanical performance is governed by more than topology and relative density and strongly influenced by process-induced microstructure from fabrication thermal history.

The comparative performance of different TPMS topologies has been systematically characterized in literature. (Yin et al., 2020) investigated four sheet-based TPMS types (Primitive, FRD, IWP, and Gyroid) fabricated from 316L stainless steel by selective

laser melting, under quasi static axial loading. Among the topologies considered, the Gyroid demonstrated a progressive collapse with a relatively smooth plateau response, although its SEA was lower than that of FRD. Primitive was the least stable, showing X shaped failure patterns and a plateau response governed by localized shear band formation. Overall, these results show that topology has a stronger effect on crushing behavior than small changes in thickness or relative density.

Hybrid and functionally graded TPMS designs have also been explored in the literature and demonstrate promising performance gains but fall outside the scope of this study. A reliable dynamic baseline for uniform G-Honeycomb and P-Honeycomb configurations must first be established before the additional variables introduced by hybridisation or grading can be systematically evaluated.

The energy absorption efficiency of a cellular structure depends strongly on how it deforms under load, which is governed by its architecture. Structures that deform primarily through bending of their walls, known as bending-dominated architectures, tend to absorb energy more gradually and exhibit a stable, extended plateau in their stress-strain response. In contrast, stretch-dominated architectures resist deformation through axial tension and compression of their walls, giving them higher initial stiffness but also making them prone to a sharp, sudden peak force before the plateau is reached. These two deformation modes produce different relationships between relative density and specific energy absorption (SEA), with bending-dominated structures generally offering more efficient and progressive energy absorption at lower relative densities (Ashby, 2006). Abdulhadi et al. (2023) identified the Primitive topology as stretch-dominated at low relative densities, which explains its characteristically high initial stiffness and sharp peak force response under axial loading

The observations suggest two main principles for TPMS crashworthiness design. Firstly, topology is the dominant factor governing deformation mode and plateau stability. The Gyroid produces progressive distributed collapse while the Primitive shows localised and unstable response. Secondly, relative density is a key performance variable for both topologies, with SEA increasing consistently with densification. This confirms that crashworthiness performance can be tuned through geometric parameters.

2.5 Dynamic and Impact Behaviour of TPMS Structures

2.5.1 Strain Rate Effects and Dynamic Enhancement

The dynamic mechanical response of TPMS structures under impact loading differs from quasi static behaviour due to micro inertia of cell walls, stress wave propagation, and strain rate dependent material properties. These mechanisms combine to produce a dynamic enhancement factor, defined as the ratio of dynamic to quasi static plateau stress that increases with impact velocity and depends on topology and relative density.

(AlMahri et al., 2021) characterised full three-dimensional TPMS lattice structures under strain rates from 10^{-3} to 10^{3} s^{-1} using AlSi10Mg Gyroid and Primitive specimens. While these are distinct from the TPMS-derived 2D structures (G-Honeycomb and P-Honeycomb) studied in this thesis, their findings provide relevant context for understanding topology-dependent dynamic behaviour. They reported dynamic enhancement factors of 1,15- 1,45, with the P topology showing the highest values due to greater perpendicular wall orientation and micro inertia effects. Deformation transitioned from progressive collapse at low rates to diffuse densification above 500 s-1, with an intermediate shock front regime. This transition reduced CFE due to reduced deformation localisation efficiency. SEA also increased under dynamic loading conditions across tested topologies. However, the study was limited to a single strain rate and employed metallic specimens only, and the authors noted that additional studies are needed to evaluate performance across a wide range of strain rates and loading conditions.

(Novak et al., 2023) extended TPMS dynamic testing over a wide strain rate range (0.005–11,000 s^{-1}) using full three-dimensional Gyroid and Primitive TPMS lattice topologies, among others, manufactured from 316L stainless steel. Similar to (AlMahri et al., 2021), only moderate hardening was found at low rates, caused mainly by material rate sensitivity and micro-inertia. Strong hardening occurred above the second critical velocity, where shock collapse increased SEA significantly across the highest-performing topologies. However, neither study examined Gyroid-inspired or Primitive-inspired topology performance specifically within the automotive crash velocity range

of 40–60 km/h, nor did either study use structures equivalent to the G-Honeycomb or P-Honeycomb defined in this thesis.

While the majority of dynamic TPMS studies focus on very high strain rates (above 500 s^{-1}) achievable with split Hopkinson pressure bars, the automotive crashworthiness regime of 40-60 km/h (approximately 11-17 m/s) corresponds to significantly lower strain rates in the range of 50-200 s^{-1} for typical crash bar geometries. This intermediate regime has received comparatively limited systematic investigation.

(Cai et al., 2025) examined TPMS deformation across quasi static and low to medium velocity impacts and identified a critical velocity threshold of approximately 8-12 m/s, below which deformation behaviour closely resembles quasi static response and above which inertial effects begin to suppress layer by layer collapse. The results show that 40 km/h marks a transition regime in which both quasi-static deformation and inertial effects are active. At 60 km/h, the response shifts towards fully dynamic behaviour, especially for low-density TPMS structures. This suggests that quasi-static optimisation alone may not be sufficient for accurate crashworthiness design.

(Ma & Guo, 2024) studied functionally graded TPMS meta-structures under dynamic loading conditions and reported that gradient direction has a stronger effect on PCF at strain rates above approximately 100 s^{-1}. However, the total energy absorption showed limited sensitivity to gradient orientation. Similarly (Liang et al., 2024) identified that the gradient directions needed to minimise PCF and maximise SEA are incompatible. This introduced a design conflict that must be resolved through multi objective optimization. These findings suggest that TPMS topology and grading strategies must be evaluated at target impact velocities rather than extrapolated from quasi static or extreme high-rate regimes.

2.6 Comparative Analysis of G-Honeycomb and P-Honeycomb

2.6.1 Quasi Static Comparison

The Gyroid and Primitive topologies have been widely compared in the literature on full three-dimensional TPMS lattice structures. The following review synthesises their behavioural tendencies to provide a basis for predicting the relative performance of the G-Honeycomb and P-Honeycomb, which are the TPMS-derived 2D structures studied

in this thesis. Conclusions vary between studies due to differences in relative density, constituent material, and loading conditions. constituent material and loading scenarios. At low relative densities (below 0,159), the P surface typically exhibits greater initial stiffness as its open channel topology aligns a larger proportion of cell walls with the loading direction. However, the same topology is more prone to shear band formation and layer by layer brittle fracture, which reduces CFE and total EA at post yield displacements. By contrast, the Gyroid topology deforms through a more distributed bending mechanism that generates a smoother, more progressive stress strain response.

(Özen & Aslan, 2023) examined Gyroid TPMS lattices fabricated from AlSi10Mg through powder bed fusion under quasi-static compression. The Gyroid exhibited shear dominated and folding damage mechanisms that produced greater stress fluctuations in the plateau region and more abrupt post peak load drops. In terms of crashworthiness, CFE reached maximum values of 51% for Gyroid, reflecting the relative brittle fracture behaviour of AlSi10Mg under the tested conditions. SEA increased clearly with relative density, suggesting improved energy absorption with densification strategies.

Additional experimental support comes from (Abueidda et al., 2019), who examined Gyroid, Primitive, IWP, and Neovius TPMS structures produced from PA 2200 by selective laser sintering. At relative densities between 14 and 15%, the Gyroid reached a compressive strength of 2.4 MPa against 1.5 MPa for the Primitive and absorbed more energy at 60% compressive strain. The Primitive consistently underperformed across all measured parameters. The Gyroid's improved mechanical response was linked to its continuous surface morphology, which encourages more uniform stress distribution and limits localized collapse. The smoother plateau response also indicates a more stable deformation process. This is valuable in crash scenarios that require predictable force transmission. Overall, these results support a performance ranking of Gyroid > Primitive for quasi-static AlSi10Mg behaviour, consistent with the findings of (Özen & Aslan, 2023).

(Wagner et al., 2025) provided supporting evidence through quasi static compression testing of polymer TPMS structures with DIC-based strain measurement. The Gyroid showed higher strength to density ratios and greater failure strain than the Primitive.

This suggests that it can sustain more deformation before fracturing. For metallic systems, (Sombatmai et al., 2024) further showed that the Gyroid performs better than the Primitive under maximum stress constraints relevant to crash design. The Primitive structure displayed unstable plateau behaviour and macroscopic shear banding at higher relative densities, reflecting its known interlayer collapse mechanism.

Across these three studies, the Gyroid consistently outperforms the Primitive, in energy absorption efficiency, plateau stability, and deformation capacity, making it the more suitable topology for crashworthiness applications, where controlled progressive crushing beneath a defined force ceiling is required.

2.6.2 Dynamic Comparison and Velocity Sensitivity

(AlMahri et al., 2021) tested five sheet-based TPMS topologies (full three-dimensional lattice structures manufactured from stainless steel SS316L) using a Direct Impact Hopkinson Bar at a strain rate of 2057 s^{-1}, representing one of the highest strain rates reported in the literature. All five topologies exhibited enhanced plateau stress and SEA under dynamic loading relative to quasi static conditions, with dynamic increase factors for plateau stress ranging from 1,10 to 1,36. The authors concluded that this improvement was mainly caused by the strain rate sensitivity of the SS316L material, rather than structural inertial effects.

(Yılmaz et al., 2024) examined cell-size-graded sheet-based Gyroid and Primitive TPMS structures, triply periodic in all three spatial dimensions produced from a photopolymer resin under deformation rates between 6 mm/min and 500 mm/min, representing lower strain-rate conditions more relevant to intermediate-velocity loading events. Their findings indicated that collapse initiation stress, plateau stress, densification strain, and SEA generally increased with deformation rate for all three topologies, a trend again attributed to the strain rate sensitivity of the base material, above which susceptibility to brittle failure increased markedly. The authors also identified a critical strain rate of 0,7 s^{-1} for the resin material, beyond which the tendency for brittle fracture increased significantly. The Primitive topology showed a significant reduction in plateau stress and SEA at the highest deformation rate of 500 mm/min (approximately 0,008 m/s), while the Gyroid maintained more stable performance, consistent with its progressive deformation behaviour observed under quasi static conditions. While these findings provide useful insight into rate dependent

behaviour trends, the tested velocity range does not approach the conditions relevant to automotive crash management, limiting the direct application of the results to this study.

Overall, these studies show that the topology hierarchy observed under quasi static conditions, with Gyroid outperforming Primitive in SEA, is generally maintained under dynamic conditions. They further suggest that dynamic improvements are mainly attributed to base material strain rate sensitivity (Yılmaz et al., 2024). However, neither study offers a direct, velocity dependent comparison of Gyroid and Primitive topologies at automotive crash velocities, which remains a principal gap addressed by this study.

2.7 TPMS Structures Compared to Conventional Honeycomb in Crashworthiness

The directional dependence identified in section 2.3 was quantified by (Wagner et al., 2025), who conducted direct quasi static compression testing SLA printed Gyroid and Primitive TPMS lattices (triply periodic in all three spatial dimensions, distinct from the TPMS-derived prismatic structures investigated in this thesis) against conventional honeycomb. Under axial loading, honeycomb achieved a strength to density ratio of 26,144 N $kg^{-1}m^3$, significantly higher than both Gyroid (5,692 N $kg^{-1}m^3$) and Primitive (5,182 N $kg^{-1}m^3$). However, under transverse loading this advantage inverted with honeycomb dropping to 1,008 N $kg^{-1}m^3$, below both variants. These results indicate that the more isotropic response of TPMS lattices is advantageous in crash events involving off axis loading.

(Zhou et al., 2024) (Zhou et al., 2024) extended this comparison to SLM-fabricated Ti-6Al-4V specimens, thereby addressing the material transferability limitation associated with earlier polymer-based studies. Their Gyroid honeycomb (a three-dimensional TPMS-based structure in that study, distinct from the G-Honeycomb defined in this thesis) demonstrated in-plane energy absorption 34.8% higher than a truss honeycomb of equivalent volume fraction under quasi-static compression. Importantly, this advantage was maintained and, in some cases, amplified under dynamic loading. At compressive velocities of 1 ms^{-1} and 10 ms^{-1}, the Gyroid honeycomb absorbed 69% and 47% more energy per unit volume, respectively than the truss equivalent. These findings obtained from metallic system representative of crashworthiness applications, provide stronger grounds for considering TPMS derived geometries as viable

alternatives to conventional honeycomb structures in automotive energy absorbing components.

Their Gyroid honeycomb (a three-dimensional TPMS-based structure in that study, distinct from the G-Honeycomb defined in this thesis) demonstrated in-plane energy absorption 34.8% higher than a truss honeycomb of equivalent volume fraction under quasi-static compression. Importantly, this advantage was maintained and, in some cases, amplified under dynamic loading. At compressive velocities of 1 ms^{-1} and 10 ms^{-1}, the Gyroid honeycomb absorbed 69% and 47% more energy per unit volume, respectively than the truss equivalent. These findings obtained from metallic system representative of crashworthiness applications, provide stronger grounds for considering TPMS derived geometries as viable alternatives to conventional honeycomb structures in automotive energy absorbing components.

A major limitation of the comparative literature reviewed is that performance is mostly evaluated under a quasi-static loading rates and against simplified honeycomb geometries rather than crash bar configurations used in real automotive bumper systems. The automotive crash bar is a constrained component with defined attachment points, wall thickness calibrated for specific regulatory impacts, and an established progressive folding pattern that has been optimised over decades of development. Accordingly, comparison between a laboratory-scale TPMS specimen and a generic honeycomb under quasi-static loading cannot substitute for a simulation or physical test in which a TPMS-derived prismatic crash bar (such as the G-Honeycomb or P-Honeycomb) and a conventional crash bar are evaluated under identical automotive loading and boundary conditions.

2.8 Numerical Methods for Finite Element Analysis

2.8.1 Explicit FEA for Impact Simulation

Explicit FEA is the standard numerical tool for predicting the crash and impact response of cellular materials. The explicit central difference scheme advances the solution incrementally in time without requiring assembly and inversion of the global stiffness matrix at each increment, thereby making it well suited to problems involving large deformation, complex contact interactions, and material nonlinearity, all of which are characteristic of crash events. Abaqus/Explicit and LS-DYNA are the most used

commercial solvers in the TPMS literature, with Abaqus/Explicit used in the majority of recent metallic TPMS impact studies.

The governing equation of the motion is integrated explicitly as:

$$u(t + \Delta t) = u(t) + \Delta t \cdot \dot{u}(t) + \left(\frac{\Delta t^2}{2}\right) \cdot \ddot{u}(t)$$

The stable time increment (Δt) must satisfy the Courant-Friedrichs-Lewy (CFL) criterion:

$$\Delta t \leq \frac{L_{min}}{c_s}$$

Where L_{min} denotes the minimum element size and c_s is the wave speed in the material. As TPMS models often require fine meshes, stable increments can become extremely small. To mitigate this, mass scaling and artificial damping are commonly introduced. Mass scaling increasing effective element density to enlarge the allowable time increment but must be controlled to avoid non-physical inertia effects. Most studies use scaling factors between 10 and 1000 and check that kinetic energy remains below 10% of internal energy.

2.8.2 Mesh Generation and Sensitivity

Finite element meshing of TPMS structures presents significant numerical challenges due to smooth, doubly curved geometry of minimal surfaces. Volumetric meshing using 3D solid elements, such as C3D10 tetrahedra, captures the full wall volume. It also represents through thickness deformation and contacts between opposing walls during densification. This approach was used instead of shell elements, which are less computationally demanding but cannot fully capture these effects

(Rezapourian et al., 2025) demonstrated that mesh density is the single most influential numerical parameter in TPMS FEA, with coarse meshes overpredicting plateau stress by as much as 20% relative to experimentally validated refined meshes. They recommended a minimum of four elements through the wall thickness for solid models and a maximum surface element size of $t/4$,where t is wall thickness.

(Sun et al., 2025) further reported that, for AlSi10Mg TPMS lattices, plateau stress converged. Within 2% of the reference solution at an approximate maximum element size of 0,1mm for wall thickness between 0,4 and 0,8 mm.

2.8.3 Material Modelling

The material model employed in TPMS impact simulations must capture elastic deformation, yielding plastic flow, strain hardening and strain rate sensitivity. For aluminium alloys, one of the most widely adopted approaches is the piecewise linear plasticity formulation, which uses experimentally derived true stress-true strain data and may incorporate strain-rate effects through Cowper-Symonds or Johnson-Cook rate dependence.

The Johnson-Cook constitutive model formation is commonly expressed as:

$$\sigma = (A + B\varepsilon^{n})(1 + C\ ln\left(\frac{\varepsilon}{\varepsilon_0}\right)(1 - T^{*m})$$

where A is the initial yield stress, B and n define strain hardening behaviour, C is the strain rate sensitivity coefficient, ε_0 is the reference rate, T^* is the homologous temperature, and m is the thermal softening exponent. For AA6061-T6 aluminium alloy, which is used as the structural material in this study, validated Johnson-Cook parameters are available in the literature and have been correlated against impact experiments. In this study, both the strain rate sensitivity term $(1 + C\ ln\left(\frac{\varepsilon}{\varepsilon_0}\right)$ and the thermal softening term $(1 - T^{*m})$ are excluded from the material model. Only the strain hardening term is activated, consistent with the rate independent elastic plastic formulation described in section 3.2. This simplification is acceptable as the strain rate effects are considered to result from inertia, not from material rate dependence, and thermal effects fall outside the defined scope of this study.

2.8.4 Validation Strategies and Surrogate Modelling

The validation of FEA models for TPMS structures typically involves comparison of force-displacement curves. Total absorbed energy and deformation patterns between simulation and physical experiment. A model is generally considered validated, if it predicts the experimental plateau force within ±10%, the total EA within ±8%, and

reproduces the correct qualitative deformation sequence, such as progressive deformation versus catastrophic failure.

The validity of Abaqus/Explicit models for TPMS crushing simulation has been discussed in the literature. (Wan et al., 2023) validated Abaqus/ Explicit models against physical crushing experiments for TPMS structures, achieving force-displacement predictions within 8% of measured results throughout the plateau regime. Based on this and similar studies, a maximum deviation of 10% in plateau force and absorbed energy is adopted as the validation limit in this study.

2.9 Research Gaps

As shown in Sections 2.1 to 2.8, five specific gaps remain between current understanding of TPMS structures and the requirements for engineering deployment of TPMS-derived prismatic crash bars as alternatives to conventional honeycomb crash bars in automotive applications. Addressing these gaps is essential, as they form an interconnected set of unresolved issues that currently restrict the adoption of G-Honeycomb and P-Honeycomb architectures in automotive crash management systems.

The most significant gap is the lack of controlled comparative studies between TPMS geometries at impact velocities relative to real automotive crash scenarios. Most dynamic characterization of TPMS structures has been carried out using Split Hopkinson Pressure Bar experiments, where strain rates in the range of 10^2-10^3 s^{-1}.

For crash bars of 80-200 mm impacted at 40-60 km/h, strain rates of approximately 50-200 s^{-1} are generated. This intermediate range is not addressed by quasi-static studies and is not directly represented in the high-rate literature. (AlMahri et al., 2021)) measured dynamic increase factors of 1.10-1.36 across five TPMS topologies at 2057 s^{-1}. The rate-dependent enhancement was linked to the material behavior of SS316L rather than inertial effects. Neither the automotive velocity range nor a direct G-Honeycomb vs P-Honeycomb comparison was included. (Yılmaz et al., 2024)) approached automotive-relevant conditions but equally did not deliver a controlled comparison between these topologies. The quasi-static ranking, in which the Gyroid has broadly outperformed the Primitive in SEA and CFE, therefore lacks dynamic validation.

The second gap arises from the absence of validated, direct performance comparisons between TPMS-derived 2D crash bars and traditional honeycomb crash bars under realistic crash scenarios. Existing studies, including (Wagner et al., 2025), mainly evaluate simplified geometries under quasi-static conditions instead of integrated structural systems at automotive impact velocities. This limitation is important as crash performance is influenced by topology and geometric scaling, end constraints, and strain-rate effects. These are not fully represented in quasi-static testing frameworks. A conclusion that TPMS structures outperform honeycomb in specific energy absorption under quasi-static laboratory compression does not constitute evidence that a TPMS-derived 2D crash bar would outperform a honeycomb crash bar in a regulatory frontal impact test, and the engineering literature does not yet contain a study that bridges this gap.

The third gap concerns the interaction between impact velocity and topology-dependent crashworthiness performance. (AlMahri et al., 2021) and (Novak et al., 2023) both report that dynamic enhancement of plateau stress and SEA is topology-dependent, with certain structures exhibiting substantially higher strain-rate hardening than others. If this topology-dependent enhancement extends into the automotive crash velocity range, the relative performance ranking of the G-Honeycomb and P-Honeycomb may not be stable across velocities. A topology selection based on quasi-static or low-rate data may therefore be unreliable for a crash bar application where the design velocity is fixed by regulatory requirements. Whether the performance ranking between the G-Honeycomb and P-Honeycomb shifts, inverts, or remains stable between 40 km/h and 60 km/h has not been examined in any study identified in this review.

The fourth gap concerns the limited availability of TPMS crashworthiness data for AA6061-T6, the wrought aluminium alloy most widely used in extruded automotive crash bars. The dominant material choices in the TPMS impact literature are AlSi10Mg and Ti-6Al-4V, both of which differ substantially from AA6061-T6 in yield strength, strain hardening behaviour, ductility, and strain-rate sensitivity. These differences have direct consequences for crashworthiness predictions. The Johnson-Cook strain-rate sensitivity parameter C for AA6061-T6 is substantially lower than that reported for AlSi10Mg processed by L-PBF, meaning that dynamic enhancement effects observed in AlSi10Mg-based TPMS studies cannot be directly transferred to AA6061-T6

structures. Similarly, the higher yield strength and lower ductility of Ti-6Al-4V produce failure modes that are not representative of wrought aluminium behaviour under automotive crash loading. As a result, existing TPMS crash performance data, even where well validated for their respective material systems, cannot be reliably extended to automotive production materials without dedicated experimental or computational investigation using AA6061-T6.

Another important gap is the lack of deformation mechanism analysis in computational TPMS crash studies. As discussed in Sections 2.7 and 2.8, most finite element work reports only macroscopic force-displacement behaviour and summary performance indicators, without resolving the internal stress-strain evolution during collapse. This is a major limitation, as key indicators such as peak crushing force, plateau stress, and crushing force efficiency are governed by microscale processes, including stress redistribution and localisation. These internal processes govern energy absorption but are not captured by global response curves. As a result, the influence of geometry on crash behaviour cannot be fully explained or predicted under changing conditions. This thesis addresses this limitation through detailed contour-based analysis across deformation stages and loading velocities.

3 METHODOLOGY

A computational method was used to compare the crashworthiness of crash bars incorporating TPMS-derived 2D structures against a conventional crash bar under impact loading. The dynamic crushing behaviour of these TPMS-derived 2D structures and a conventional crash bar was investigated using the commercial finite element analysis software Abaqus/Explicit. A consistent method to develop the models was adopted ensuring reproducibility and consistency. First, TPMS-derived 2D structures and the conventional structure were designed with controlled parameters in SolidWorks. Then, material properties, boundary conditions, and loading cases are applied uniformly using Abaqus Explicit. Finally, performance metrics including energy absorption, peak crushing force, and deformation behaviour are extracted for comparison. All models were analysed under identical boundary conditions and loading to ensure a consistent comparison. However, the structures differ in mass due to their internal topology, and therefore the comparison is not strictly mass equivalent.

3.1 Geometry Modelling

Geometry modelling is a critical step in this study, as the structural configuration directly influences energy absorption and deformation behaviour. The geometries of the TPMS derived 2D structures (Gyroid and Primitive variants) and the conventional structure were developed with controlled parameters to ensure a fair comparison.

3.1.1 TPMS Geometry Definition

The structures used in this thesis are generated from 2D cross-sectional patterns derived from TPMS level set equations, which define continuous periodic surfaces. Two TPMS-derived structures are considered: a Gyroid derived structure and a Primitive derived structure. These 2D cross sectional profiles were developed and visualised using the Desmos mathematical tool, allowing direct control over geometric parameters. It is important to note that these are not full three-dimensional TPMS lattice implementations; the cross-sectional topology is derived from TPMS level-set equations and subsequently extruded longitudinally to produce the three-dimensional crash bar core geometry. These geometries are developed and visualised using the Desmos mathematical tool, allowing direct control over geometric parameters.(Peng et al., 2023)

The G-Honeycomb is generated from the following trigonometric implicit level set function:

$$-t \leq \sin(x)\,cos(y) + \sin(y)\cos(n) + \sin(n)\cos(x) \leq t$$

where t is a level set constant that controls the relative density of the structure. By adjusting t, the thickness of the solid region changes, which directly affects porosity and mass distribution.

In this implementation, n serves the equivalent role of z in the standard level set equation, controlling periodic variation within the 2D cross-sectional plane. The inequality form −t ≤ ... ≤ t extracts a solid region of controlled thickness centred on the zero-surface, consistent with the sheet-network architecture described in Section 2.3.1.

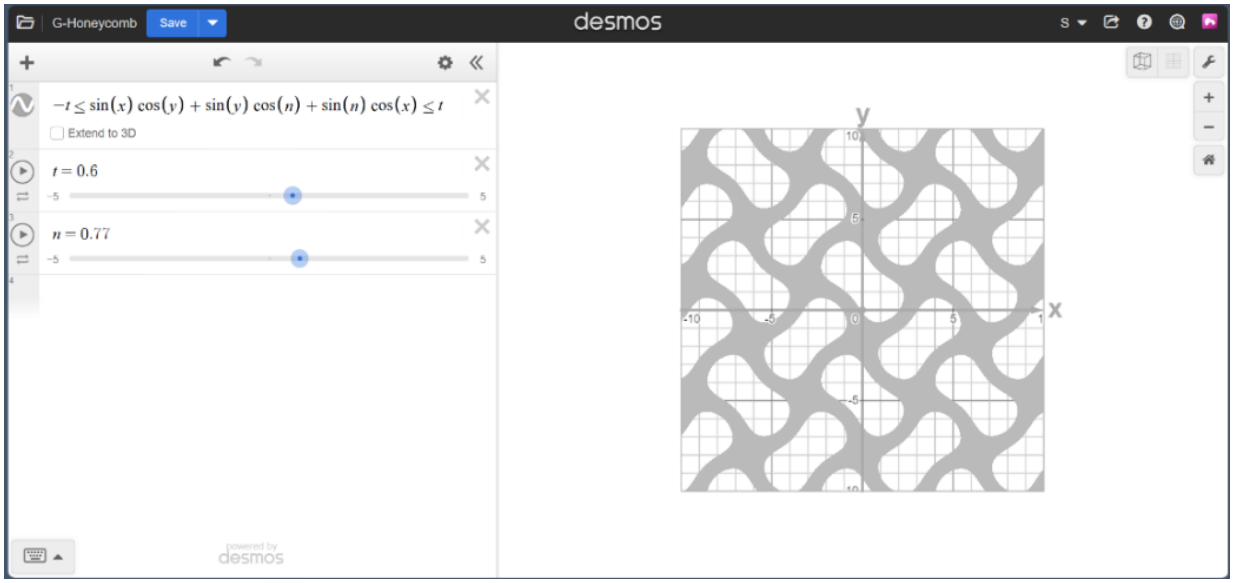

Figure 2 - 2D cross-sectional profile of the G-Honeycomb generated in Desmos

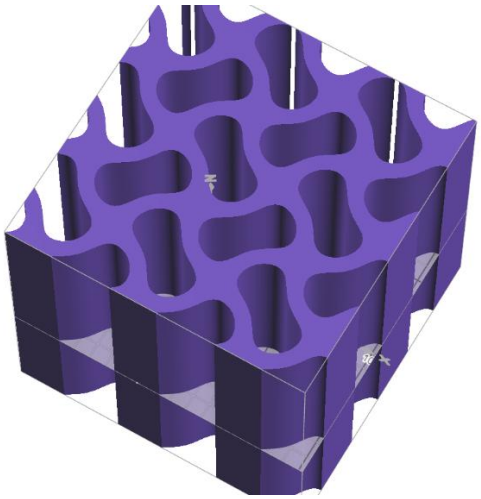

Figure 3 - Extruded 3D crash bar geometry of the G-Honeycomb

These parameters are tuned in Desmos to obtain a stable and manufacturable geometry with the desired density.

The Primitive surface is defined using the following implicit equation:

$$\cos(a - x) + \cos(b - y) - c \leq m$$

Where a, b, and c are geometric shift and scaling parameters, and m defines the solid region threshold. The parameters used for this structure are, a = −2.8, b = −3.8, c = −0.8, m = 0.

The P-Honeycomb was constructed from a 2D cross-sectional pattern generated from this implicit equation in Desmos and subsequently extruded along the longitudinal Z-axis in SolidWorks to produce the three-dimensional crash bar core. This produces a prismatic structure whose cross-sectional topology is inspired by the open-channel, cubic-symmetric character of the Schwartz P surface. While this approach differs from a fully three-dimensional level-set implementation, TPMS-derived 2D structures of this type represent an established approach in the crashworthiness literature, where the primary loading direction is axial and the cross-sectional topology governs deformation behaviour.

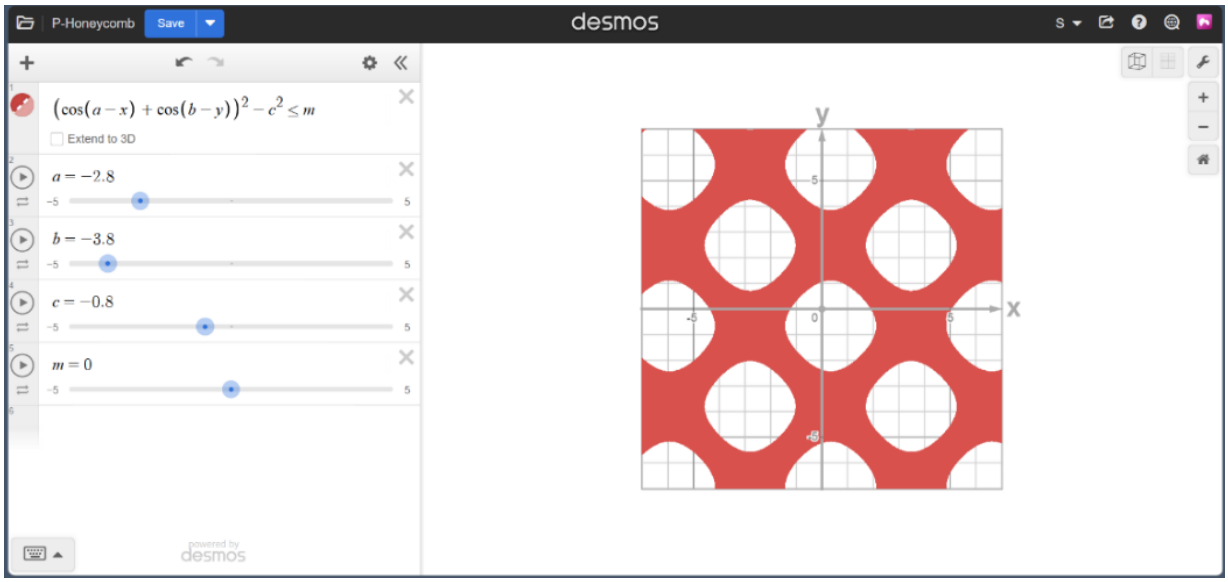

Figure 4 - 2D cross-sectional profile of the P-Honeycomb generated in Desmos

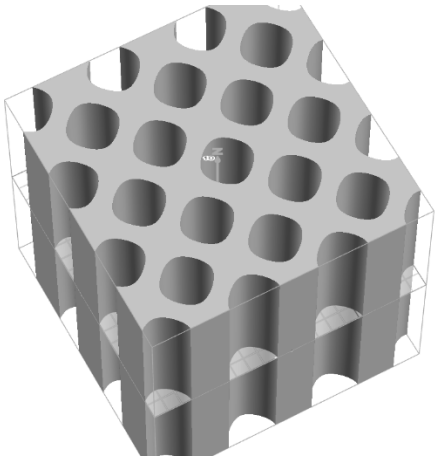

Figure 5 - Extruded 3D crash bar geometry of the P-Honeycomb

The parameters a, b, c, and m control the spacing, orientation, and size of the repeating unit cells. By modifying these values, the geometry can be adjusted to get the optimal relative density and structural behaviour.

Both the G-Honeycomb and P-Honeycomb were designed as periodic unit cells in the cross-sectional plane and built longitudinally through extrusion to form the complete crash bar geometry. The use of implicit level-set functions ensures smooth wall profiles in both structures, which promotes more uniform stress distribution during deformation.

The Desmos-based approach provides a simple and effective means of visualising and adjusting the 2D cross-sectional profiles of the G-Honeycomb and P-Honeycomb before exporting them into CAD and finite element environments.

3.1.2 CAD Model Generation

The G-Honeycomb and P-Honeycomb geometries were created using a multi-step digital process to transform the 2D level-set cross-sectional profiles into manufacturable solid models suitable for finite element analysis.

Implicit level-set equations for the G-Honeycomb and P-Honeycomb were implemented in the Desmos mathematical tool to visualise the 2D cross-sectional patterns and control the geometry through variables t, n, and phase-shift constants. These 2D cross sectional patterns were then exported from the app as SVG vector graphics files. The SVG files were then imported into Inkscape for preprocessing, the geometries were cleaned, scaled, and converted into closed profiles ready for import into CAD software. The files were then saved as DXF (Drawing Exchange Format), which is widely supported for CAD import.

The DXF files were imported into SolidWorks. The 2D cross-sectional profiles of the G-Honeycomb and P-Honeycomb were then extruded along the longitudinal direction to form the internal core structures. These cores were then Incorporated within a predefined crash bar geometry.

Two types of TPMS-based structures were developed:

- G-Honeycomb (G) structure

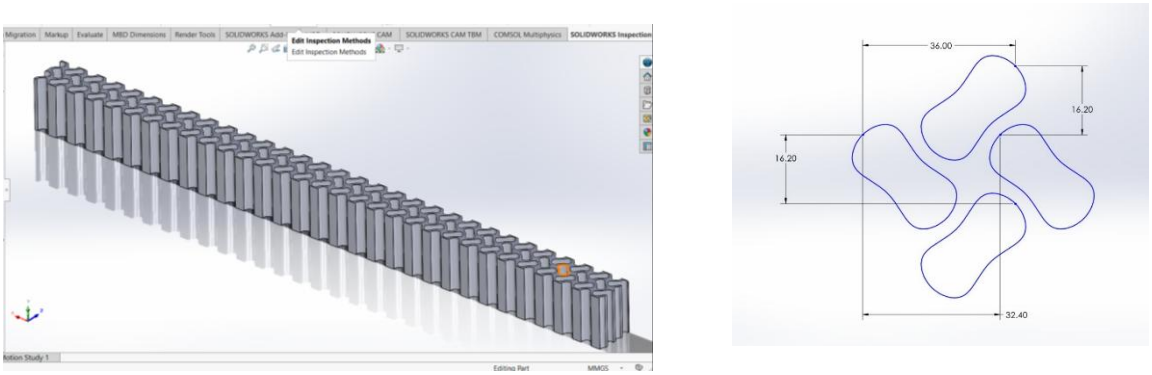

Figure 6 – G-Honeycomb crash bar core design

- P-Honeycomb (P) structure

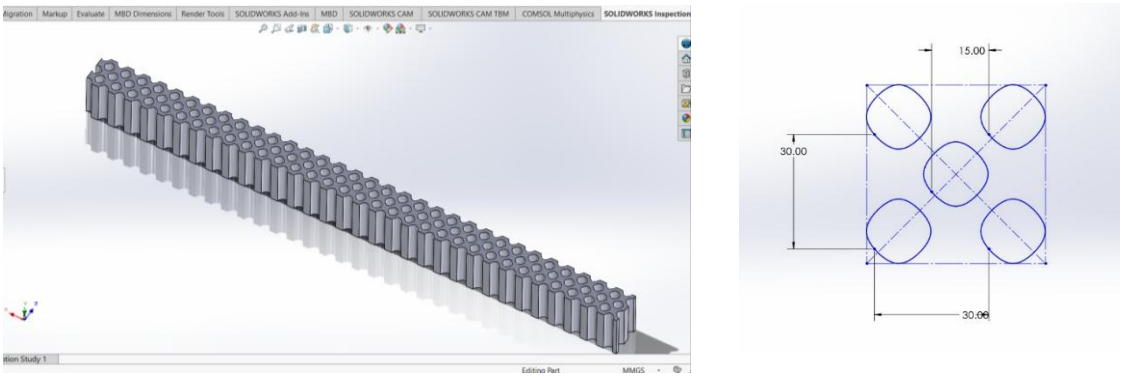

Figure 7 – P-Honeycomb crash bar core design

Both the G-Honeycomb and P-Honeycomb crash bar cores were modelled with the following identical external dimensions:

- Length = 1200 mm
- Width = 80 mm
- Height = 80 mm

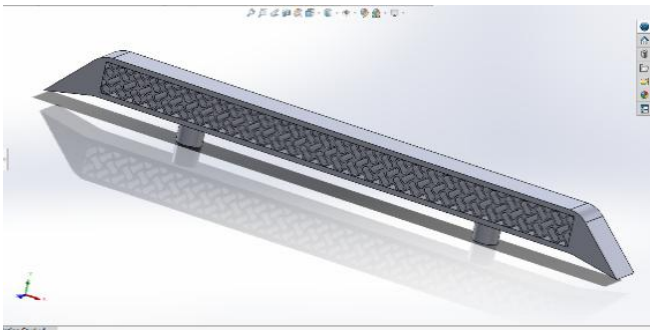

Figure 9 - G-Honeycomb crash bar

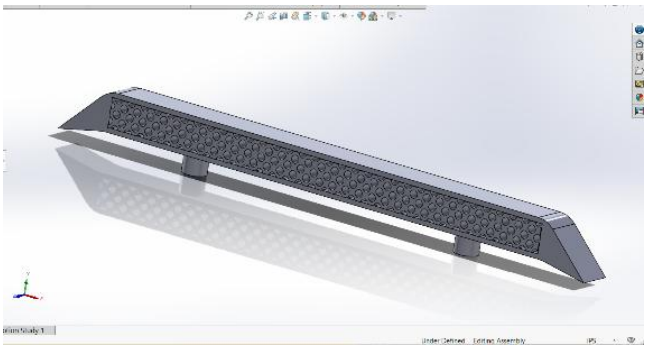

Figure 8 - P-Honeycomb crash bar

The individual cross-sectional unit cell patterns of the G-Honeycomb and P-Honeycomb were repeated along the length of the crash bar through longitudinal extrusion to form the complete internal core geometry. This ensured geometric consistency and allowed direct comparison between the two topologies.

To enable a comparison, a conventional crash bar was also modelled in SolidWorks. The conventional crash bar model consists of a hollow cylindrical tube with a diameter of 40 mm.

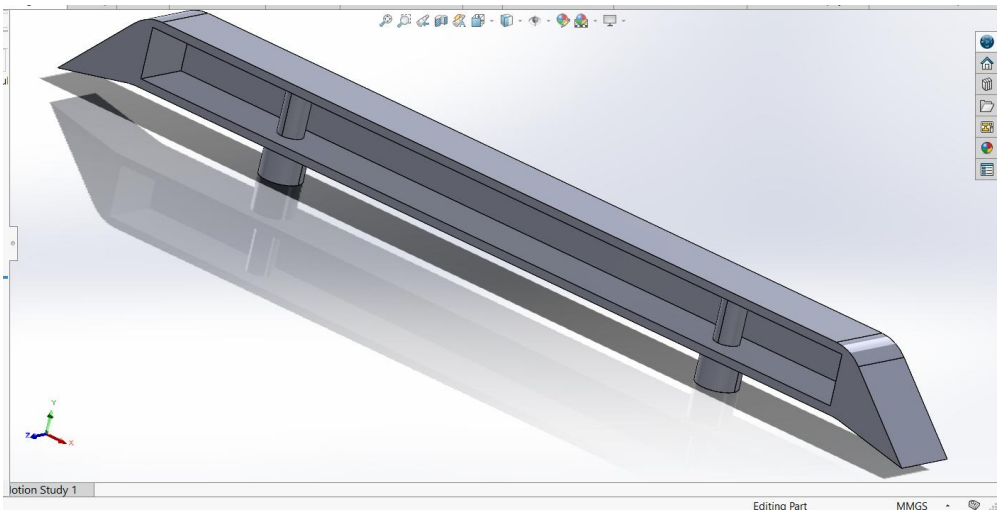

Figure 10 - Conventional crash bar

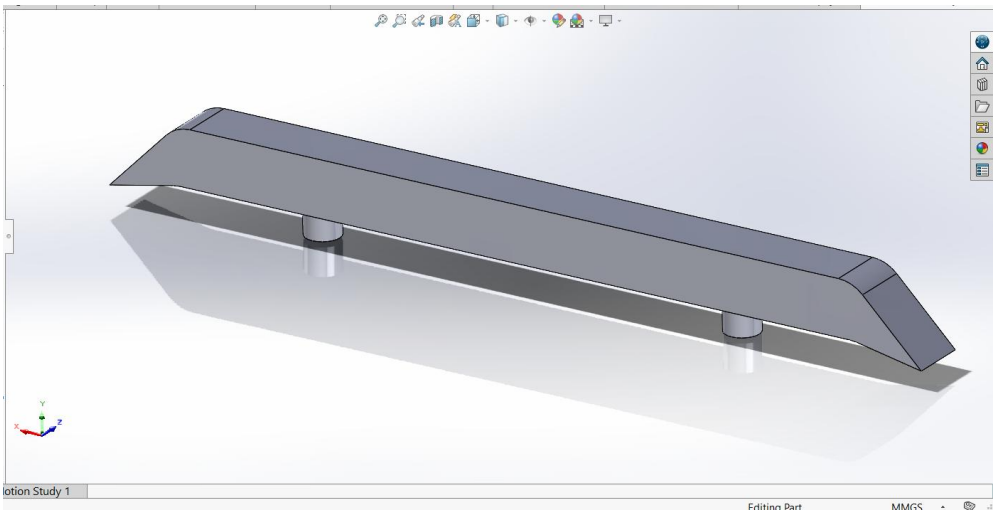

Figure 11 - Conventional crash bar

For a fair comparison, the conventional crash bar maintains the same external dimensions as the G-Honeycomb and P-Honeycomb designs.

3.2 Material Properties

Accurate prediction of deformation and energy absorption for dynamically loaded structures requires a robust material model. In the present work, the widely used automotive crash component material aluminium alloy AA6061-T6 was adopted for all geometries, owing to its well documented mechanical properties.

AA6061-T6 aluminium alloy is suited for use in lightweight structural applications where a good balance of strength, ductility, and manufacturability is required. It is widely applied in automotive crash structures such as bumper beams and energy absorbers.

Another advantage of this alloy is the availability of reliable material data in the literature, which supports accurate numerical modelling. In addition, AA6061-T6 is compatible with modern manufacturing techniques, including additive manufacturing, making it a suitable material choice for the G-Honeycomb and P-Honeycomb designs should physical fabrication be pursued.

The mechanical properties used in the simulations are taken from standard references and are summarised in Table 1 (MatWeb LLC, 2024).

Table 1 - Material properties of AA6061-T6

Property	Value
Density (ρ)	2700 kg/m³
Young's Modulus (E)	68.9 GPa
Poisson's Ratio (v)	0.33
Yield Strength (σ_Y)	276 MPa
Ultimate Tensile Strength	310 MPa

These properties are used to define the elastic and plastic behaviour of the material in the finite element model.

The material model is defined as rate-independent elastic-plastic. Strain-rate effects are not included in this thesis. Therefore, any variation in force response with impact velocity is attributed to inertial effects and increased kinetic energy, rather than strain-rate-dependent material behaviour. The elastic region is defined using Young's modulus and Poisson's ratio, while plastic behaviour is described using a stress-strain curve based on available experimental data.

In this study, the selected material model assumes isotropic behaviour and uniform properties throughout the structure. Thermal effects or material damage are not considered. Which simplifies the analysis while still capturing the main deformation characteristics.

3.3 Finite Element Model

Finite element models of the G-Honeycomb, P-Honeycomb, and conventional crash bar were analysed under dynamic impact loading. Abaqus/Explicit was used to analyse high-speed deformation, complex contact interactions, and nonlinear material behaviour of the G-Honeycomb, P-Honeycomb, and conventional crash bar.

3.3.1 Software selection.

The numerical analysis has been performed using the Abaqus/Explicit software. The explicit dynamic solver in Abaqus/Explicit has been chosen to simulate the dynamic impact problem efficiently.

A methodology is demonstrated to accurately predict the force-displacement response and energy absorption characteristics of the G-Honeycomb, P-Honeycomb, and conventional crash bar.

3.3.2 Model Import and Assembly Setup

All the developed models have been exported from SolidWorks CAD system in the form of STEP files (.step). These STEP files were then imported into Abaqus/Explicit. A consistent unit system has been adopted throughout the simulation. In this simulation, all dimensions of models were described in millimetres, masses in tonnes and time in seconds.

All inputs, including geometry dimensions, material properties and boundary conditions, are provided within this consistent unit system to avoid scaling errors and ensure accurate simulation results.

The conventional, G-Honeycomb, and P-Honeycomb crash bar configurations were modelled as deformable bodies while the impactor has been modelled as a discrete rigid body to reduce computational cost. An isotropic inertia corresponding to a mass of 0.2 tons (200 kg) has been assigned to the rigid body of the impactor. This simplifies the model while maintaining realistic impact behaviour. The reference point of the rigid body is then used to apply velocity and boundary conditions.

All components, including the crash bar and impactor were assembled and within the Abaqus assembly module. Proper positioning and alignment were ensured to maintain

consistent contact interaction during simulation. Distance between crash bar and impactor is 5 mm.

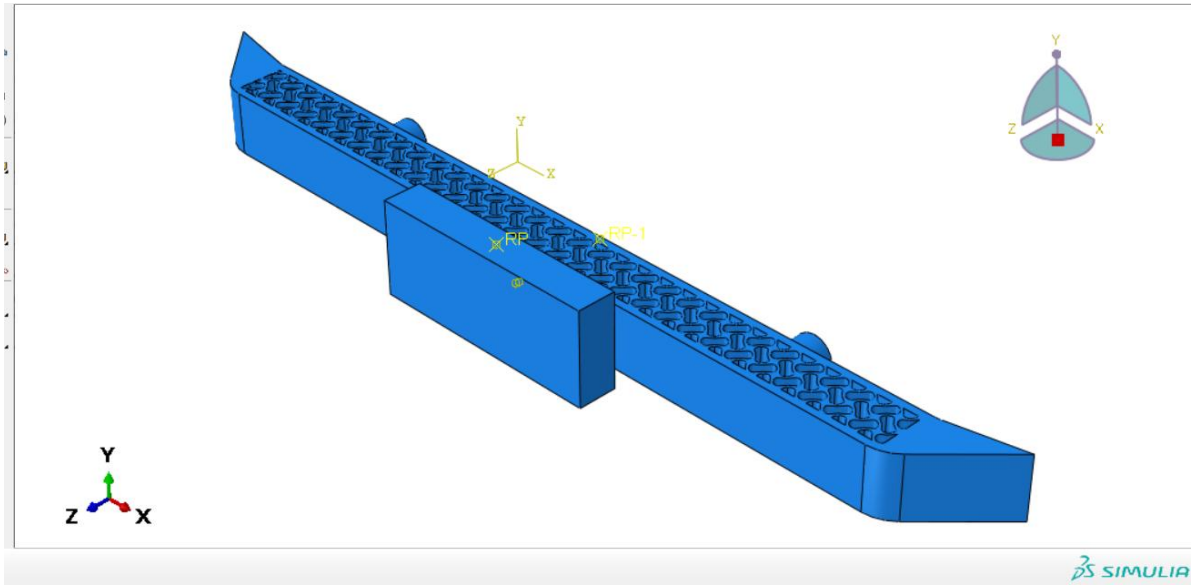

Figure 12 - Assembled G crash bar and impactor in Abaqus

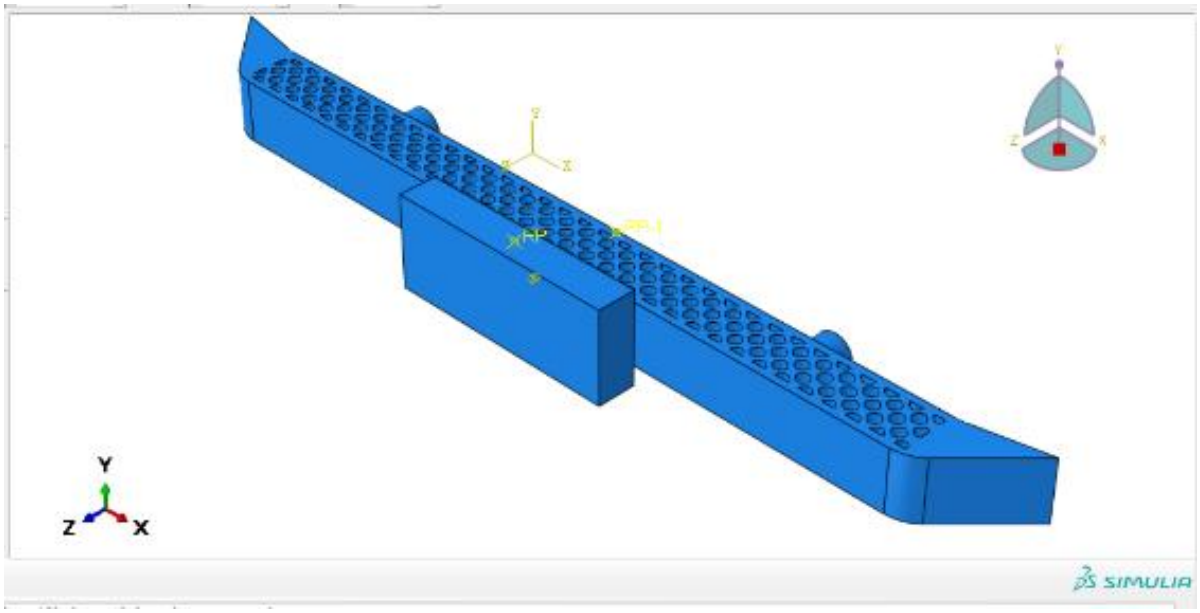

Figure 13 - Assembled P crash bar and impactor

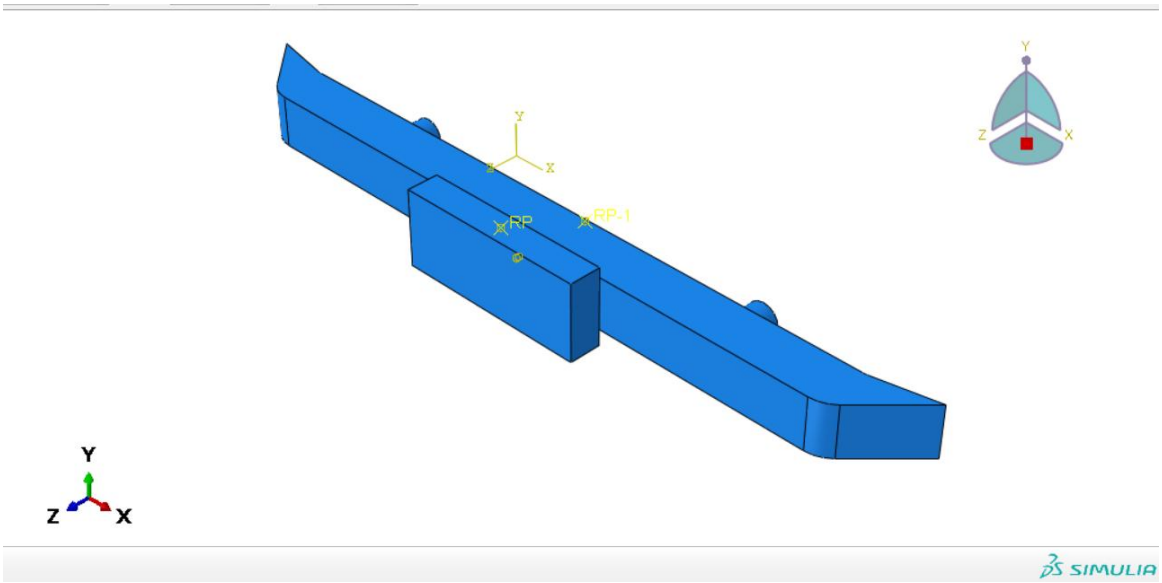

Figure 14 - Assembled traditional crash bar and impactor

3.3.3 Material Assignment

The material properties of AA6061-T6 were assigned to all crash bar models. The mass of each structure differs due to its internal geometry, as summarised below:

- Traditional crash bar**:** 10.1 kg
- G-honeycomb crash bar**:** 11.4 kg
- P-honeycomb crash bar: 13.5 kg

These mass differences arise due to variations in internal topology and material distribution. Despite having identical external dimensions, the internal structures influence the overall mass and, consequently, the energy absorption behaviour.

As the three structures differ in mass due to their internal topology, direct comparison of total energy absorption (EA) alone is not considered valid. All primary conclusions are therefore drawn from mass-normalised and efficiency-based metrics, specifically Specific Energy Absorption (SEA) and Crush Force Efficiency (CFE).

3.3.4 Dynamic Explicit Analysis

After defining the geometry and assembly, the analysis step was created using the Dynamic, Explicit procedure in Abaqus. This step is specifically designed for problems

involving high-speed events, such as impact and crash simulations (Ogmaia & Tasel, 2015).

The Dynamic Explicit solver is selected because it can efficiently handle:

- Large deformations
- Complex contact interactions
- Nonlinear material behaviour
- Short-duration dynamic events

Unlike implicit methods, the explicit solver does not require iterative convergence at each increment. This makes it more stable and computationally efficient for impact problems. (Ogmaia & Tasel, 2015)

In this study, the loading event occurs over a very short time period, time period of simulation is 5 milliseconds. Therefore, the explicit dynamic step is suitable for accurately capturing the transient response of the crash bar during impact.

3.3.5 Mesh Strategy

A finite element mesh was generated for all crash bar models to accurately capture the deformation behaviour during impact. Due to the complex internal geometry of the G-Honeycomb and P-Honeycomb, a tetrahedral free-meshing technique was adopted.

For the Gyroid (G) and Primitive (P) honeycomb structures, a finer mesh was applied within the internal honeycomb core region to accurately represent the complex topology. A detailed mesh size of 8 mm was applied to the internal G-Honeycomb and P-Honeycomb core regions, with a slightly coarser mesh size of 10 mm applied to the outer crash bar shell. This approach balances accuracy and computational efficiency. This approach balances accuracy and computational efficiency.

A 3D stress element type of C3D10M with quadratic tetrahedral formulation was selected. This element type is well suited for solving problems which include large deformation as well as complex geometrical features.

The mesh quality and size for each model are summarised as follows:

- G-Honeycomb crash bar

- Number of elements: 148,404
- Analysis errors: 0 (0%)
- Analysis warnings: 149 (0.10%)

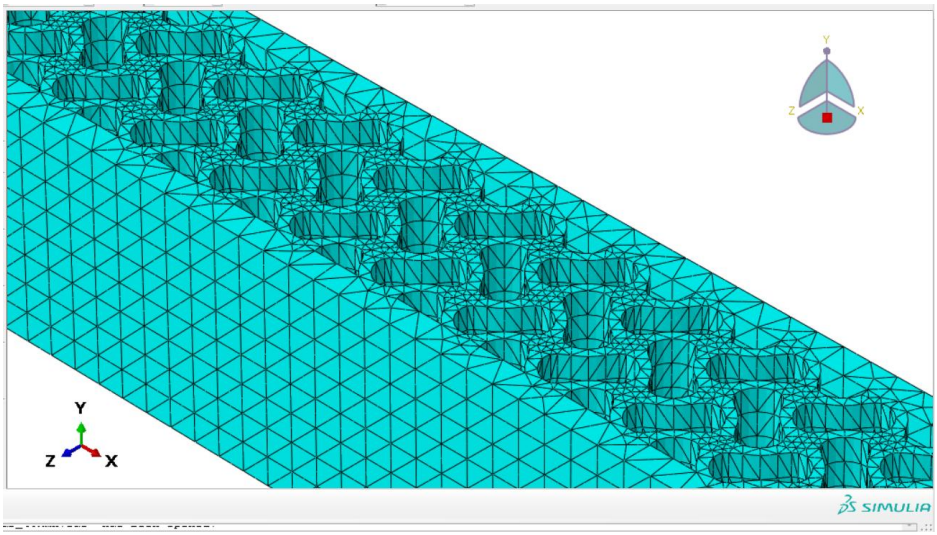

Figure 15 - Finite element mesh of the G-Honeycomb crash bar

- P-Honeycomb crash bar
  - Number of elements: 158,171
  - Analysis errors: 0 (0%)
  - Analysis warnings: 1506 (0.95%)

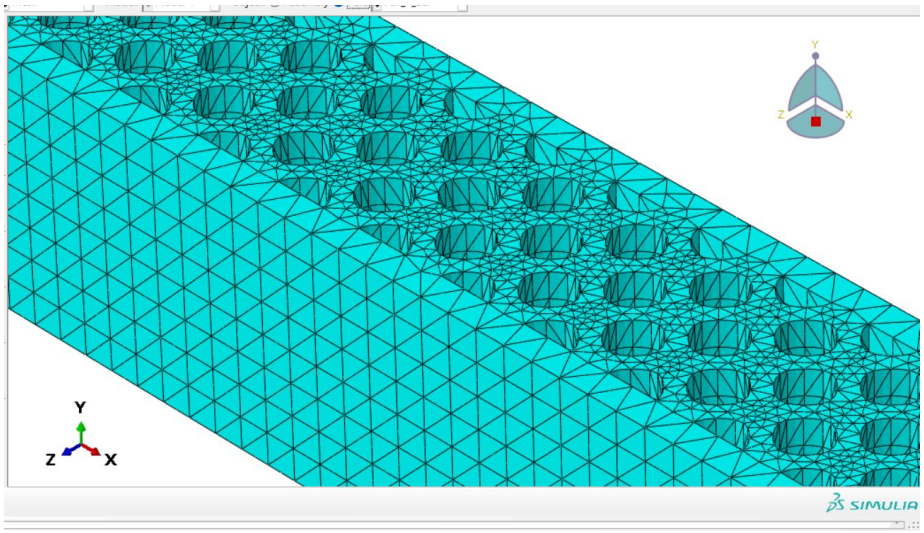

Figure 16 - Finite element mesh of the P-Honeycomb crash bar

- Traditional crash bar
  - Number of elements: 25,666

- Analysis errors: 0 (0%)
- Analysis warnings: 0 (0%)

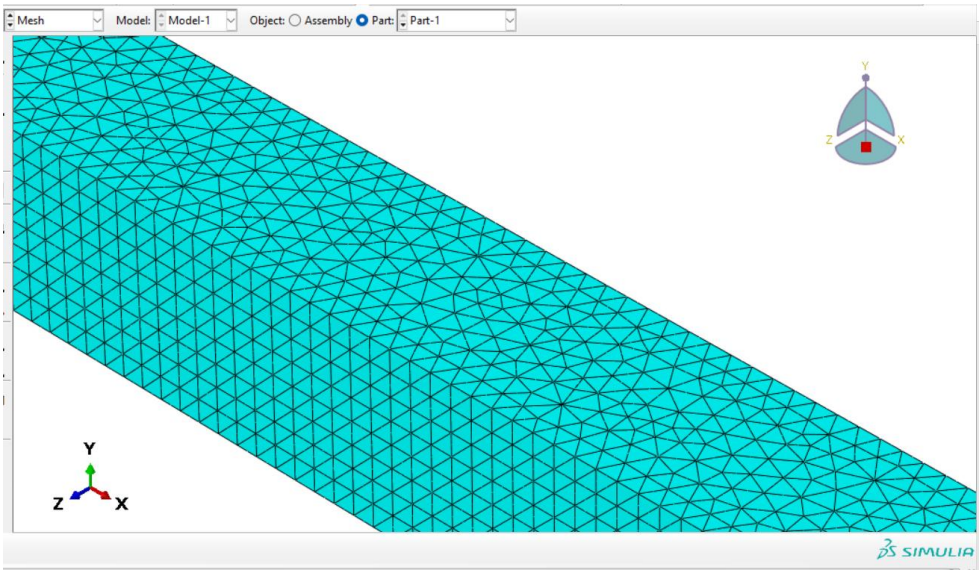

Figure 17 - Meshed traditional bar

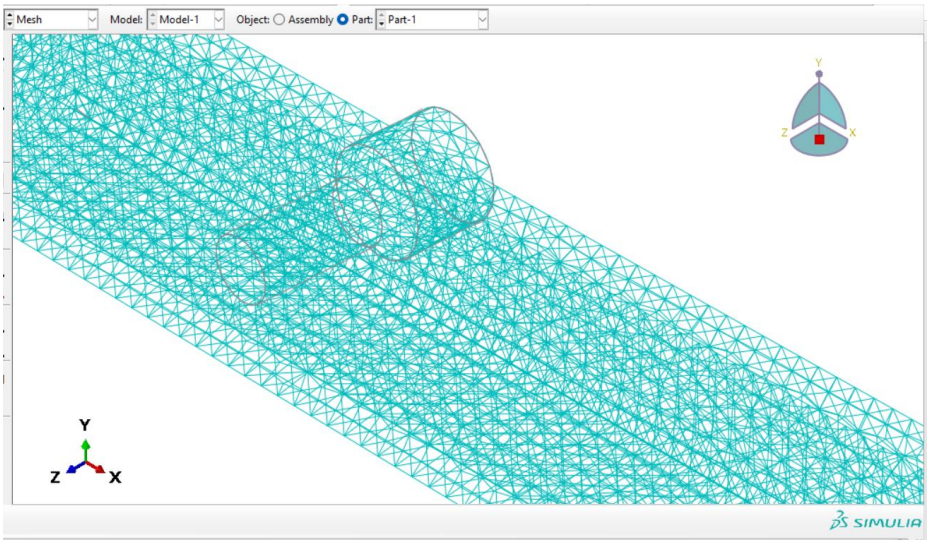

Figure 18 - Meshed traditional bar (wireframe style)

Figures 17 and 18 present the finite element mesh of the conventional hollow cylindrical crash bar. Figure 17 shows the overall element distribution across the outer cylindrical wall, while Figure 18 provides a wireframe view revealing the internal void region and the uniform element distribution through the wall thickness.

In contrast to the conventional crash bar, the G-Honeycomb and P-Honeycomb have more complex internal geometries, requiring a greater number of elements to achieve adequate discretisation.

The rigid parts were meshed using a quadrilateral-dominated free mesh. Since these parts are defined as rigid bodies, a coarse mesh is sufficient and does not significantly affect the accuracy of the results.

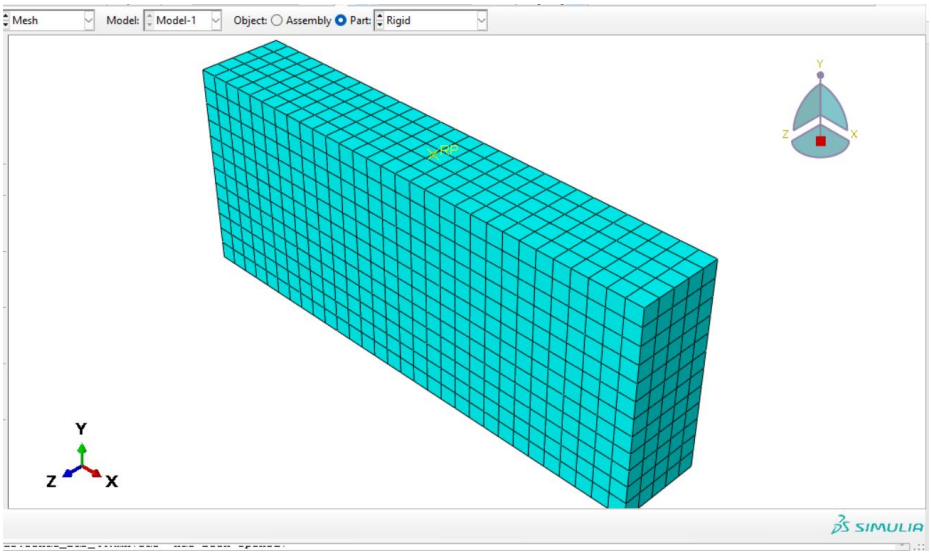

Figure 19 - Meshed rigid impactor

A formal mesh convergence study was not conducted due to the high computational cost of the complex G-Honeycomb and P-Honeycomb geometries. Confidence in the selected mesh size is however supported by zero analysis errors across all models, element distortion warnings ranging from 0% to 0.95% across the three structures, and artificial energy ratios well below the accepted 5% threshold in all simulations. Based on these findings, the adopted mesh quality is considered acceptable for accurately capturing the overall deformation and energy absorption behaviour, The absence of a formal convergence study is nonetheless acknowledged as a limitation.

3.3.6 Interaction Definition

In the numerical model, contact interactions between all components were modelled using the General Contact (Explicit) algorithm available in Abaqus/Explicit. This algorithm allows automatic detection of contact between multiple surfaces and is particularly well suited to the complex internal geometries of the G-Honeycomb and P-Honeycomb.

The contact behaviour was defined using the following parameters:

- Contact type: General contact (Explicit)
- Tangential behaviour: Penalty formulation with a friction coefficient of 0.3 (Liu et al., 2022).
- Normal behaviour: Hard contact.

The friction coefficient used in the simulation is representative of aluminium to aluminium contact conditions and allows realistic simulation of sliding resistance during deformation. Hard contact in the normal direction was enforced in order to ensure that surfaces do not penetrate each other during impact.

3.4 Boundary Conditions and Loading

Boundary conditions and loading configuration were defined in order to represent the dynamic impact behaviour of the crash bar. The simulations were carried out with consistent boundary conditions and loading parameters to ensure a controlled comparison between different structural configurations.

3.4.1 Impact Setup

For the rigid impactor in the model, the encastre boundary condition was applied at the reference point to fully constrain all translational and rotational degrees of freedom.

U1=U2=U3=UR1=UR2=UR3=0

Above, U1 - displacement along X-axis; U2 - displacement along Y-axis; U3 - displacement along Z-axis; UR1 - rotation about X-axis; UR2 - rotation about Y-axis; UR3 - rotation about Z-axis.

As a result, the rigid impactor is held completely fixed during the simulation and serves as a stable reference point through which loads are transferred.

For the crash bar, displacement and rotation boundary conditions were applied. In the initial step, all translational and rotational degrees of freedom of the entire crash bar body were constrained to maintain the initial positioning and prevent any unintended motion before the loading is applied.

The impact loading was applied in the Dynamic Explicit step by assigning a velocity to the crash bar in the Z-direction (U3). The velocity was applied along the Z-direction (U3 ≠ 0), while the other directions were constrained:

U1 = 0, U2 = 0

UR1 = UR2 = UR3 = 0

Where U1 is displacement in X- direction, U2 is displacement in Y- direction, U3 is displacement in Z- direction, UR1 is rotation about X-axis, UR2 is rotation about Y-axis, and UR3 is rotation about Z-axis.

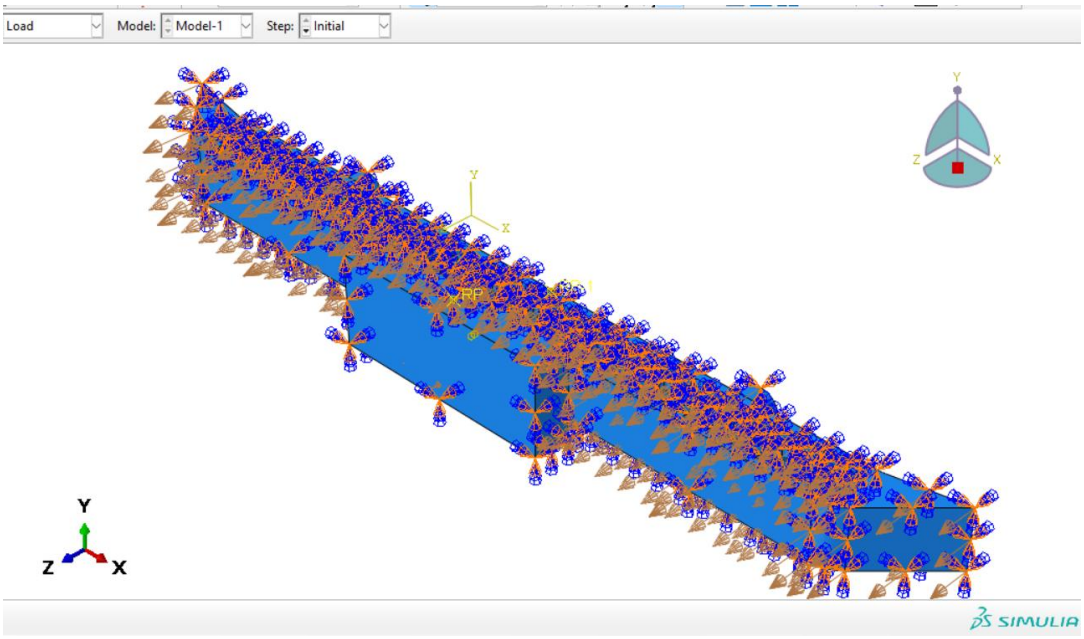

Figure 20 - Apply boundary condition to simulation

Two different impact velocities were considered to evaluate performance under varying crash conditions:

- 40 km/h = 11.11 m/s = 11,110 mm/s
- 60 km/h = 16.67 m/s = 16,670 mm/s

The encastre condition is used for rigid impactor to simulate a fully fixed boundary, which is commonly assumed in crash simulations.

In the idealised impact scenario used in this study, the crash bar moves directly toward a fixed rigid surface. It is recognised that in real vehicle systems, the crash bar is connected to deformable components such as crush cans, which also contribute to

energy absorption during impact. As such, this simplification may result in a slightly stiffer response compared to real-world conditions.

3.4.2 Output Requests

The performance of the structures is evaluated based on several output parameters recorded during the simulation. The reaction force at the rigid body is presented as a force-displacement curve, from which energy absorption as well as other performance metrics can be determined.

Three types of energies: internal energy, kinetic energy, and plastic dissipation energy (ALLIE, ALLKE, ALLPD) are monitored during analysis for simulation accuracy and stability verification. The loading conditions are realistic, consistent, and suitable for evaluating crash performance. (Demirci et al., n.d.)

3.5 Performance Metrics

To evaluate the crashworthiness of the structures, several quantitative performance metrics are defined based on the force-displacement response obtained from the simulations. These metrics allow a consistent comparison between the G-Honeycomb, P-Honeycomb, and conventional crash bar under identical loading conditions.

3.5.1 Energy Absorption (EA)

Crash bars on vehicles primarily absorb and dissipate kinetic energy. As the front part of the vehicle they are the first to come into contact with impact loading during a crash. Therefore the material used to manufacture the bars is subjected to significant deformation during use. Typically this is in the form of controlled plastic deformation of the material through bending, folding or crushing, rather than operating in a completely rigid state. Through this deformation process, the vehicle's kinetic energy is converted into deformation energy, thereby protecting the occupants and other critical vehicle components from the severity of the impact forces.

It is calculated as the area under the force-displacement curve up to the densification point.

$$EA = \int_0^{\delta_D} F(\delta) d\delta$$

Where F(δ) is the crushing force, dδ is the incremental displacement, and δD is the displacement at densification. (Xia et al., 2023)

Higher Energy Absorption means the bar can absorb more impact energy before it reaches the vehicle frame. A structure with higher EA therefore gives better occupant protection.

Densification is the point during an impact event where the cellular or thin-walled structure has fully collapsed, cell walls have made contact, and the material acts as a solid, resulting in a rapid increase in stress. It marks the end of the energy-absorbing plateau region.

Before densification, structure deforms and absorbs energy efficiently. After densification, structure becomes stiff and force increases rapidly. It is therefore desirable for densification to occur as late as possible, allowing the crash bar to absorb the maximum amount of energy before the onset of full compaction.

3.5.2 Specific Energy Absorption (SEA)

Specific energy absorption is defined as the energy absorbed per unit mass of the structure. This metric is important for lightweight design applications.

$$SEA = \frac{EA}{m}$$

where m is the mass of the structure. Vehicles need to stay lightweight. A crash bar with high SEA (Specific Energy Absorption) absorbs a large amount of energy with a minimal amount of material. In cases where two designs absorb the same amount of energy, the lighter one is preferable.

3.5.3 Peak Crushing Force (PCF)

The peak crushing force is defined as the highest force value observed during the initial stage of impact, and is a critical crashworthiness indicator used to determine the severity of force transmitted to the occupants during a collision event. It represents the maximum force experienced by the structure prior to the onset of buckling or progressive folding and is therefore of direct relevance in assessing the safety risk posed to the occupants of the vehicle.

$$PCF = \max\left(F(\delta)\right)$$

This value gives a direct indication of the high peak forces that can occur during an impact. High peak forces translate into severe impact loads, which represent a critical safety risk to the vehicle structure and its occupants. High PCF means a sudden large force which can damage the chassis and cause serious injury to the occupants of the vehicle. A well designed crash bar is therefore one that minimises these high PCF values to reduce the risk of injury during a collision.

3.5.4 Mean Crushing Force (MCF)

The mean crushing force represents the average force during deformation and provides an indicator of how efficiently a structure can dissipate kinetic energy during a collision event.

$$MCF = \frac{EA}{\delta_D}$$

The mean crushing force (MCF) is a measure of the overall load carrying capacity of the structure. A higher MCF with controlled PCF means the crash bar is consistently absorbing energy throughout the deformation process, rather than failing prematurely.(Jackowski et al., 2023).

3.5.5 Crush Force Efficiency (CFE)

Crush force efficiency is defined as the ratio of the mean crushing force to the peak crushing force, measuring how consistently a structure absorbs energy during a collision event.

$$CFE = \frac{MCF}{PCF}$$

A higher CFE (closer to 1 or 100%) will lead to improved consistency in terms of energy absorption and reduced peak forces. This will result in reducing the structural impact severity and the risk of injuries to occupants. In addition, a high CFE indicates more effective and stable progressive collapsing behavior. Such performance metrics will allow complete assessment and comparison of different structural configurations investigated within this research. (Sebaey, 2020)

3.6 Model Validation and Assumption

3.6.1 Model Validation

The proposed approach in this study is purely computational, therefore no experimental validation is performed for the proposed finite element models. The modelling methodology was, however, validated using available literature data where similar simulation methods, material systems, and experimental testing conditions were utilised. This approach is consistent with established practice in the TPMS crashworthiness literature, where Abaqus/Explicit models are validated against experimental results from prior studies before being applied to novel structural configurations. (Rezapourian et al., 2025; Wan et al., 2023)

The numerical models were established by using the finite element analysis method, where C3D10M (modified quadratic tetrahedral solid element) was adopted in the models. General contact with penalty friction coefficient of 0.3 was applied. A rate-independent elastic-plastic constitutive model was used to define the deformation behaviours of the AA6061-T6 alloy. The adopted finite element models for TPMS impact simulation in the paper have been validated and their accuracy was confirmed by relevant existing research works. Wan et al., 2023 demonstrated that Abaqus/Explicit models with equivalent contact definitions and mesh densities predicted force-displacement responses within 8% of experimental measurements throughout the plateau regime. Therefore, the maximum error of 10% of the plateau stress and total energy absorption was taken as the acceptance criterion for the developed models in the study.

The G-Honeycomb model showed consistent, distributed crushing with a stable plateau consistent with the layer-by-layer folding reported in the literature for Gyroid TPMS lattices (AlMahri et al., 2021; Novak et al., 2023), providing qualitative correspondence despite the geometric differences between the extruded 2D cross section used in this thesis and volumetric TPMS implementations.. The P-Honeycomb model showed localised collapse predominantly in a shear mode with pronounced post-peak force variation, consistent with the interlayer failure behaviour documented for Primitive TPMS lattices (Abueidda et al., 2019; Sombatmai et al., 2024). These qualitative correspondences confirm that the models reproduce physically representative deformation modes for each topology.

For the numerical validation of the obtained results the energy balance of the analyzed models has been checked. The artificial strain energy (ALLAE) remained below 5% of the total internal energy (ALLIE) throughout all simulations. The internal energy (ALLIE) increased steadily and remained closely matched to the plastic dissipation energy (ALLPD), confirming that the dominant energy pathway was permanent plastic deformation. This is the physically expected behaviour for a crashworthy structure. From a mechanical point of view valid results have been achieved; from a numerical point of view the results are reliable.

3.6.2 Assumption And Simplifications

Numerical simulations were performed on the basis of several assumptions and simplifications. Firstly, a perfect CAD model of the crash bar structures was created without accounting for any manufacturing errors or geometric imperfections/surface roughness. The crash bar structures were designed with a constant wall thickness. Additionally, a homogenous and isotropic material assumption was made for all crash bar structures (G-Honeycomb, P-Honeycomb and Traditional). This means that a constant material property was assumed for all crash bar structures. The dynamic simulations did not account for any temperature rise and subsequent thermal softening during an impact event.

Boundary conditions and contact definitions were defined such that the impactor was modelled as rigid without any deformation. General contact with constant friction coefficient was defined between the impactor and sample. Surface interactions were assumed to behave uniformly and were not expected to introduce any differences. Mass scaling was used to speed up the computations, and was not expected to cause significant errors.

The G-Honeycomb and P-Honeycomb were created from 2D cross-sectional patterns extruded along the longitudinal axis, rather than from a fully three-dimensional level-set implementation. Consequently, the curved wall profile characteristic of the TPMS level-set equations is retained only within the cross-sectional (XY) plane, while the structure extends as straight prismatic walls along the Z-direction. This may result in a higher axial stiffness relative to a true three dimensional TPMS lattice. However, TPMS-derived 2D structures of this type represent an established approach in the crashworthiness literature where the primary loading is axial and cross-sectional

topology governs deformation behaviour; this simplification is therefore considered acceptable for the present study.

4 RESULTS

A total of six finite element simulations were performed to evaluate the crashworthiness performance of three different crash bar configurations under dynamic impact loading conditions. The structures considered include the conventional crash bar, the G-Honeycomb crash bar, and the P-Honeycomb crash bar. Each structure was analysed under two impact velocities, namely 40 km/h and 60 km/h.

The results presented in this chapter are based entirely on numerical simulations conducted using Abaqus/Explicit. The outputs analysed include force-displacement response, energy absorption characteristics, deformation patterns, and velocity sensitivity.

4.1 Force - displacement Response (40km/h)

The force-displacement behaviour of the crash bars is used to evaluate the crushing performance under impact loading. The reaction force was obtained from the rigid component and plotted against displacement.

4.1.1 G-Honeycomb Crash Bar

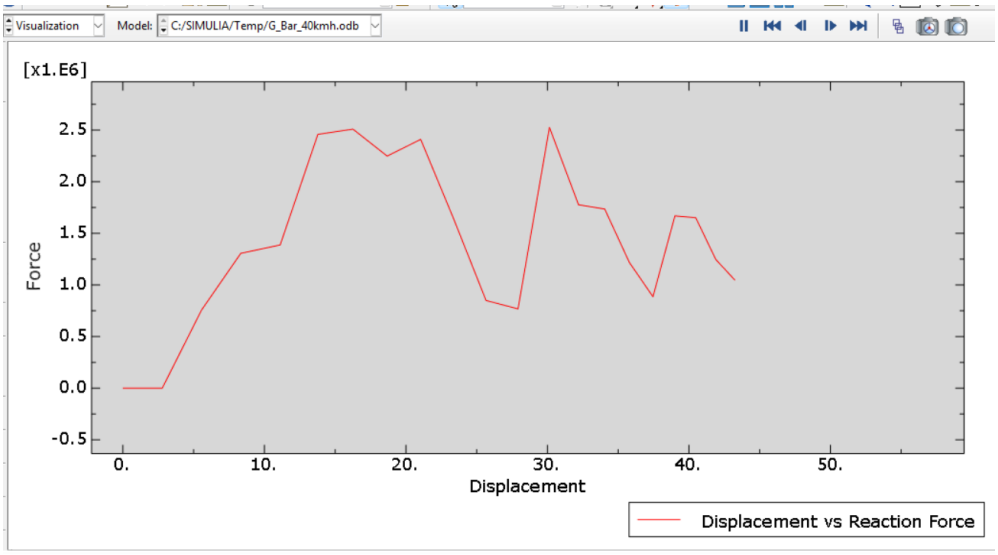

Figure 21 - G-Honeycomb force-displacement 40km/h Graph

Figure 21 - Force-displacement response of the G-Honeycomb crash bar under impact loading at 40 km/h, showing the initial peak crushing force, plateau region, and progressive deformation behaviour. The steadily increasing line in this chart indicates

the material is beginning to deform. The initial peak was 2.51MN at 16.26mm displacement. A fluctuating plateau stage followed between 15 mm and 35 mm displacement, during stable and progressive crushing of the internal G-Honeycomb core, after which the force decreased gradually. The maximum peak crushing force (PCF) was 2.53MN at 30.14mm. The post peak drop is smooth with oscillations in force until the final displacement of 43.25 mm where continuous folding and energy dissipation occur. The relatively smooth plateau region suggests efficient load distribution and stable deformation behaviour.

4.1.2 P-Honeycomb Crash Bar

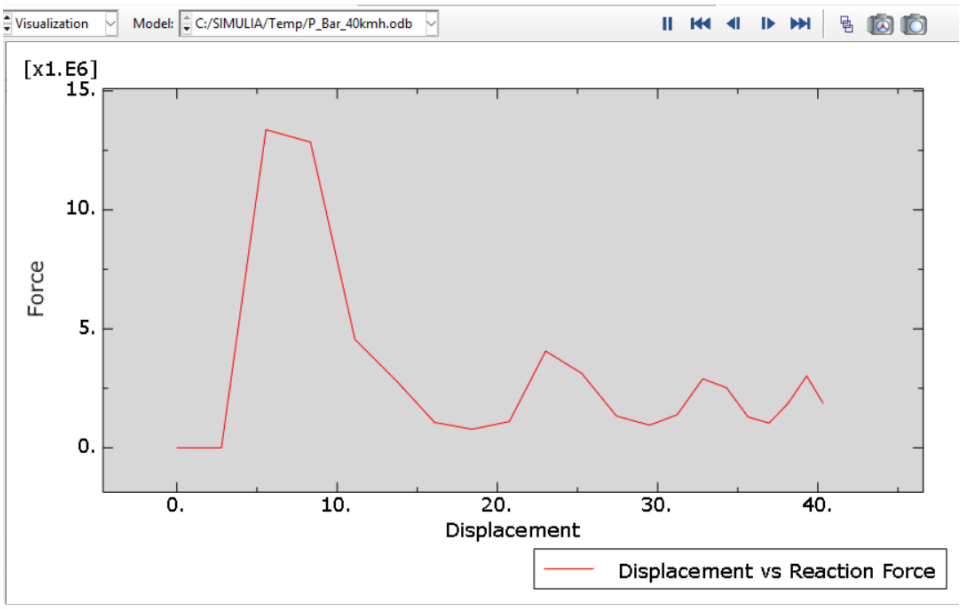

Figure 22 – P-Honeycomb force-displacement Graph (40km/h)

The P-Honeycomb crash bar demonstrated a significantly different response. The force profile for this product exhibited a very high initial peak force of approximately 13.4 MN occurring at 5.56 mm, indicating a stiff initial response. The force then drops very quickly showing unstable crushing. The post peak response is then characterised by irregular variations throughout the deformation process. There are several secondary peaks with the largest two occurring late in the deformation with forces of 4.06 MN and 3.02 MN. (Figure 22). On closer inspection however, one can observe localised deformation and uneven energy absorption compared to the Gyroid structure. The Primitive structure does not contain a stable plateau and as such, does not undergoing progressive collapse efficiently.

4.1.3 Traditional crash Bar

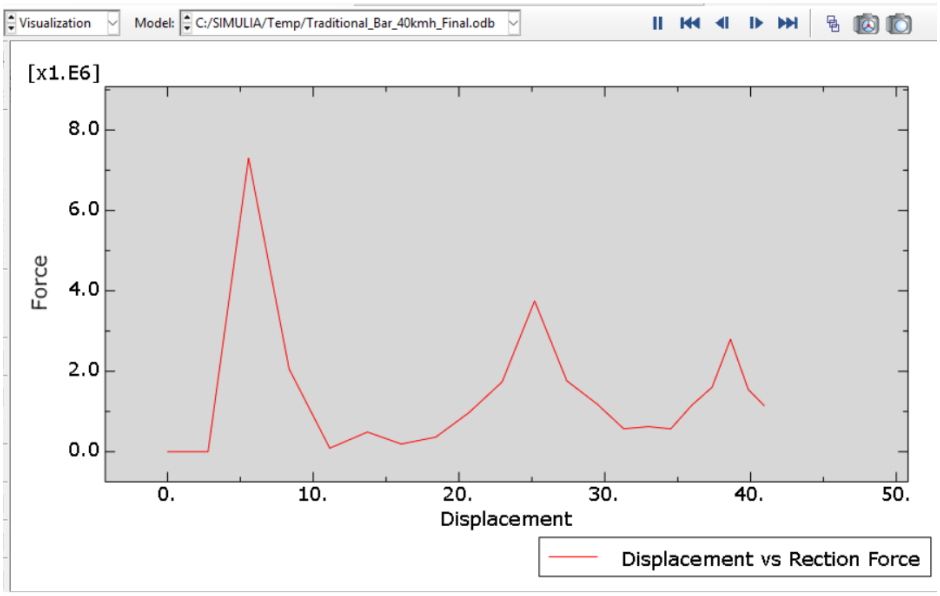

Figure 23 - Traditional force-displacement Graph (40km/h)

The standard crash bar studied here showed a sharp highest point at the initial stage of impact with an axial force of approximately 7.30 MN at 5.57 mm. The force reduced steadily down a straight pull with some small oscillations, indicating limited load carrying capacity during progressive deformation. There were a few secondary peaks the highest being 3.75 MN at 25.19 mm and the last at 2.80 MN at 38.62 mm. The observed deformation behaviour results in less uniform deformation and lower crush force efficiency (CFE = 0.21) compared to the G-Honeycomb (CFE = 0.58) and P-Honeycomb (CFE = 0.26).

4.2 Force - Displacement Response (60Km/h)

4.2.1 G-Honeycomb Crash Bar

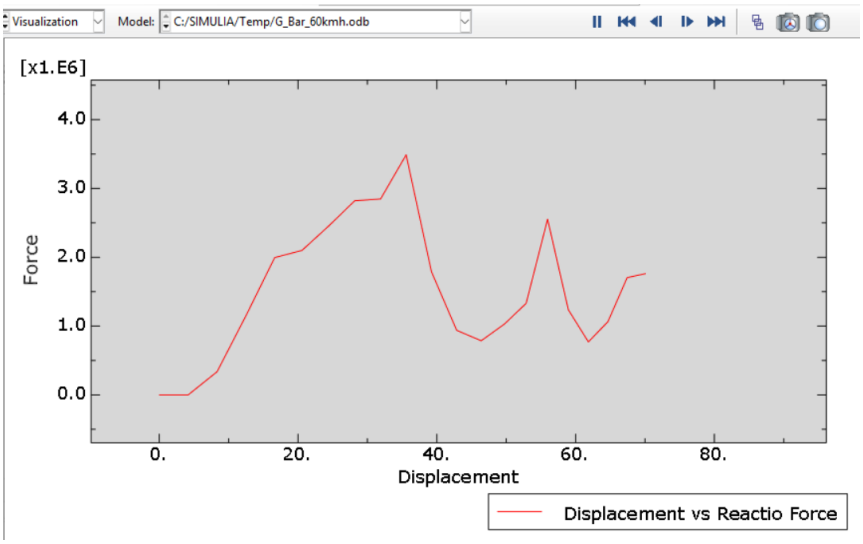

Figure 24 – G-Honeycomb force-displacement 60km/h Graph

The force displacement response of the G-Honeycomb crash bar at 60 km/h begins with a gradually increasing force due to the progressive collapse of the internal honeycomb core, increases steadily up to the PCF of 3.49 MN at 35.58 mm. This is higher than the PCF at the lower test velocity of 40 km/h due to increased impact energy and inertia. The force then decreases and fluctuates between 0.7 MN and 2.5 MN as further progressive collapse occurs until maximum deformation of approximately 70 mm. This is significantly greater than the deformation seen at 40 km/h. The slow increasing section of force followed by a long plateau section indicates stable energy absorption and uniform crush bar deformation.

4.2.2 P-Honeycomb Crash Bar

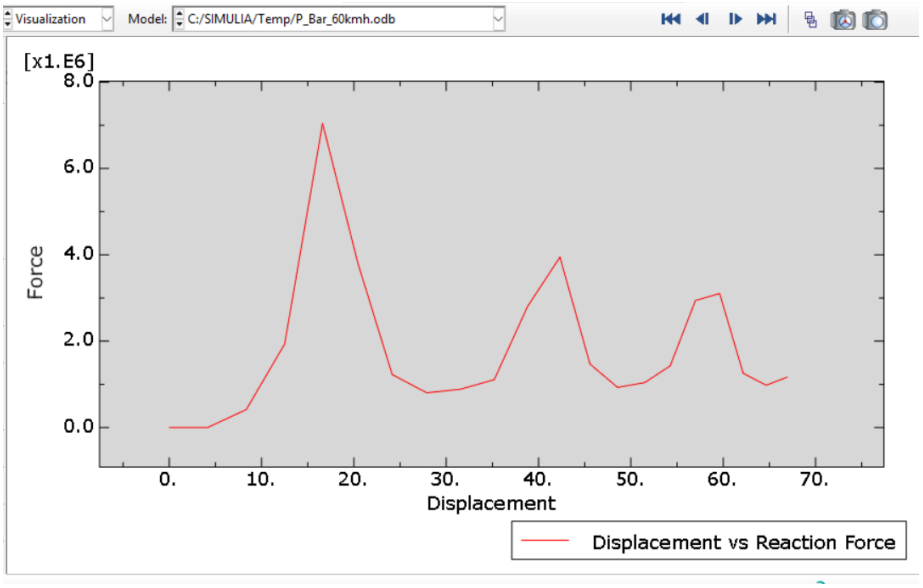

Figure 25 - Primitive Force displacement 60km/h Graph

Dynamic Unloading Force data for the P-Honeycomb sample crash test revealed an unusual high initial peak force of 7.04 MN at 16.61 mm, which is significantly higher than the G-Honeycomb.

The force drops rapidly, followed by irregular fluctuations. There are two secondary peaks of approximately 3.95 MN and 3.10 MN. The crushing behaviour is unstable and localised. This suggests early dynamic structural collapse compared to the 40 km/h test. The force-time history does not have a consistent plateau region and therefore the load is not efficiently transferred across the structure.

4.2.3 Traditional Crash Bar

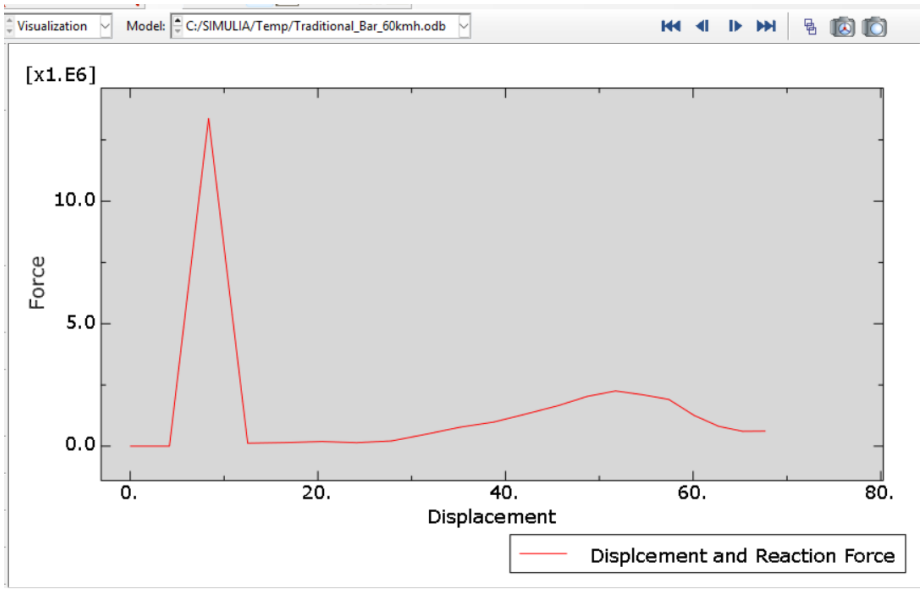

Figure 26 - Traditional Force displacement 60km/h Graph

The load-displacement curve of the standard crash bar starts at a very high force of about 13.4 MN at a displacement of 8.35 mm. The force then decreases immediately and strongly and only shows a weak increase reaching values around 2.25 MN before decreasing again in the later stages of deformation. The structure is stiff and rigid at the beginning, then changes to a weak progressive deformation. The load-carrying capacity after the first impact is limited and there is no well-defined plateau.

4.3 Energy Absorption Metrics (40km/h)

The energy absorption capability of the structures was evaluated based on the simulated force displacement response. The key crashworthiness parameters calculated include SEA, PCF, MCF, CFE, EA (Specific Energy Absorption, Peak Crushing Force, Mean Crushing Force, and Crush Force Efficiency, Energy Absorption) were evaluated. EA was calculated from the area under the force displacement curve by the numerical trapezoidal rule. (Ha et al., 2024)

$$EA = \sum \left(\frac{F_i + F_{i+1}}{2} \right) \times (\delta_{i+1} - \delta_i)$$

Three different structures with the same external dimensions were analysed using finite element simulations. Although they have the same dimensions, they have

different mass, therefore the comparison is not mass-equivalent; instead, specific energy absorption (SEA) is used as the primary metric for performance comparison.

Symbol	Meaning
EA	Total energy absorbed by the structure
$\sum$	Summation over all data intervals
F_i	Force at the i-th data point
F_{i+1}	Force at the next data point
δ_i	Displacement at the i-th data point
δ_{i+1}	Displacement at the next data point

4.3.1 G-Honeycomb Crash Bar

The G-Honeycomb showed well balance of crashworthiness at 40 km/h collision test results of collision resistance. The absorbed energy is 63.3 kJ with small peak force of 2.53 MN. The corresponding SEA value is 5.55 kJ/kg with moderate energy absorption efficiency relative to its mass.

The mean crushing force (MCF) for the G-Honeycomb structure simulated was 1.46 MN. The structure had a crush force efficiency (CFE) of 0.58. The G-Honeycomb structure performed well dissipating energy steadily and safely up to the average crush strength.

Table 2 illustrates the parameters of G-Honeycomb crash bar at 40 km/h with their respective values.

Table 2 - Parameters of Gyroid Crash Bar at 40 km/h with their respective values

Parameter	Value (with Unit)
Energy Absorbed (EA)	63.3 kJ
Mass	11.4 kg
Specific Energy Absorption (SEA)	5.55 kJ/kg
Peak Crushing Force (PCF)	2.53 MN
Mean Crushing Force (MCF)	1.46 MN
Crushing Force Efficiency (CFE)	0.58

4.3.2 P-Honeycomb Crash Bar

For the P-Honeycomb structure the energy absorption achieved was 139.4 kJ at 40 km/h. The average specific energy absorption (SEA) for this test was 10.3 kJ/kg, indicating excellent energy absorption capability. The corresponding peak crushing force was 13.4 MN.

The mean crushing force for the test specimen Primitive was found to be 3.45 MN. However the mean crush force efficiency was found to be only 0.26. This indicates a very high initial peak force and subsequent unstable deformation. Despite the high energy absorbed, Primitive is less suitable under these test conditions.

Table 3 illustrates the parameters of P-Honeycomb crash bar at 40 km/h with their respective values.

Table 3 - Parameters of Primitive Crash Bar at 40 km/h with their respective values

Parameter	**Value**
Energy Absorption	139.4 kJ
Mass	13.5 kg
Specific Energy Absorption	10.3 kJ/kg
Peak Crushing Force	13.4 MN
Mean Crushing Force	3.45 MN
Crush Force Efficiency	0.26

4.3.3 Traditional Crash Bar

It is observed that the existing design can absorb an impact energy of 61.8 kJ; however it is lower than both the G-Honeycomb and P-Honeycomb. The Specific Energy Absorption of the existing design is found to be 6.1 kJ/kg. Moreover, the peak crushing force remains relatively high at 7.30 MN.

Average crushing force was 1.5 MN, comparable to the Gyroid structure; while CFE was merely 0.21, indicating inefficient energy distribution, which does not exhibit stable progressive collapse, resulting in lower overall crashworthiness performance.

Table 4 illustrates the parameters of traditional crash bar at 40 km/h with their respective values.

Table 4 - Parameters of Traditional Crash Bar at 40 km/h with their respective values

Parameter	Value
Energy Absorption	61.8 kJ
Mass	10.1 kg
Specific Energy Absorption	6.1 kJ/kg
Peak Crushing Force	7.30 MN
Mean Crushing Force	1.5 MN
Crush Force Efficiency	0.21

4.4 Energy Absorption Metrics (60km/h)

4.4.1 G-Honeycomb Crash Bar

At 60 km/h, the gyroid structure exhibits significantly enhanced energy absorption of 109.2 kJ with an SEA of 9.6 kJ/kg. The peak crushing force is increased only moderately to 3.49 MN. MCF (1.6 MN) and CFE (0.46) confirm that the structure maintains stable and controlled deformation at higher speeds. The G-Honeycomb structure achieves a well-balanced performance in terms of stiffness, energy absorption, and peak force.

Table 5 illustrates the parameters of G-Honeycomb crash bar at 60 km/h with their respective values.

Table 5 - Parameters of G-Honeycomb Crash Bar at 60 km/h with their respective values

Parameter	Value
Energy Absorption	109.2 kJ
Mass	11.4 kg
Specific Energy Absorption	9.6 kJ/kg
Peak Crushing Force	3.49 MN
Mean Crushing Force	1.6 MN
Crush Force Efficiency	0.46

4.4.2 P-Honeycomb Crash Bar

Test results show 127 kJ of absorption at 60 km/h with an SEA of 9.4 kJ/kg (indicating high energy absorption capability). The peak crushing force decreased to 7.04 MN, which is still relatively high. The mean crushing force was found to be greater than that of the G-Honeycomb sample at 1.9MN, however the Crush Force Efficiency (CFE) was only 0.27. The results show that the structure still experiences unstable deformation, although the reduction in peak force suggests earlier structural collapse at higher velocity.

Table 6 illustrates the parameters of P-Honeycomb crash bar at 60 km/h with their respective values.

Table 6 - Parameters of Primitive Crash Bar at 60 km/h with their respective values

Parameter	**Value**
Energy Absorption	127 kJ
Mass	13.5 kg
Specific Energy Absorption	9.4 kJ/kg
Peak Crushing Force	7.04 MN
Mean Crushing Force	1.9 MN
Crush Force Efficiency	0.27

Notably, the energy absorption of the P-Honeycomb decreased from 139.4 kJ at 40 km/h to 127 kJ at 60 km/h, which is counterintuitive as higher impact velocity is generally expected to increase energy absorption. This anomalous trend is discussed further in Section 4 (Discussion).

4.4.3 Traditional Crash Bar

The traditional crash bar at 60 km/h absorbed 108.6 kJ of energy, with a high SEA of 10.75 kJ/kg. The peak crushing force of 13.4 MN is undesirable for crash safety.

The traditional crash bar achieved an average 1.6 MN mean crushing force, however its average CFE was only 0.12, indicating a poor CFE. The structure proved effective in energy absorption but had poor stability during crushing.

Table 7 illustrates the parameters of traditional crash bar at 60 km/h with their respective values.

Table 7 - Parameters of Traditional Crash Bar at 60 km/h with their respective values

Parameter	Value
Energy Absorption	108.6 kJ
Mass	10.1 kg
Specific Energy Absorption	10.75 kJ/kg
Peak Crushing Force	13.4 MN
Mean Crushing Force	1.6 MN
Crush Force Efficiency	0.12

The change in performance metrics between 40 km/h and 60 km/h is presented below.

Table 8 - Performance metrics for the G-Honeycomb, P-Honeycomb, and conventional crash bar at 40 km/h and 60 km/h.

Structure	Velocity (km/h)	EA (kJ)	Mass (kg)	SEA (kJ/kg)	PCF (MN)	MCF (MN)	CFE
Gyroid (G)	40	63.3	11.4	5.55	2.53	1.46	0.58
Primitive (P)	40	139.4	13.5	10.3	13.4	3.45	0.26
Traditional	40	61.8	10.1	6.1	7.30	1.5	0.21
Gyroid (G)	60	109.2	11.4	9.6	3.49	1.6	0.46
Primitive (P)	60	127	13.5	9.4	7.04	1.9	0.27
Traditional	60	108.6	10.1	10.75	13.4	1.6	0.12

The Gyroid structure, energy absorption increases from 63.3 kJ to 109.2 kJ, and specific energy absorption increases from 5.55 kJ/kg to 9.6 kJ/kg. The peak crushing force increases from 2.53 MN to 3.49 MN, while the mean crushing force increases slightly from 1.46 MN to 1.6 MN. The crush force efficiency decreases from 0.58 to 0.46.

The Primitive structure, energy absorption decreases from 139.4 kJ to 127 kJ, and specific energy absorption decreases from 10.3 kJ/kg to 9.4 kJ/kg. The peak crushing force decreases from 13.4 MN to 7.04 MN, and the mean crushing force decreases from 3.45 MN to 1.9 MN. The crush force efficiency shows a slight increase from 0.26 to 0.27.

The traditional structure, energy absorption increases from 61.8 kJ to 108.6 kJ, and specific energy absorption increases from 6.1 kJ/kg to 10.75 kJ/kg. The peak crushing force increases from 7.30 MN to 13.4 MN, while the mean crushing force increases slightly from 1.5 MN to 1.6 MN. The crush force efficiency decreases from 0.21 to 0.12.

4.5 Deformation Behaviour

4.5.1 Von Mises stress Distribution (40 km/h)

Figure 27-35 present the von Mises stress distribution for the G-Honeycomb, P-Honeycomb and Traditional crash bars at different deformation stages under 40 km/h impact. For direct comparison of all plots, a consistent colour scale was used.

G-Honeycomb crash bar

The G-Honeycomb exhibits well-distributed deformation along the length of the crash bar, with the internal honeycomb core transferring force along multiple load paths during crushing.

Most regions actively participate in deformation, which results in progressive crushing instead of localized failure, stable collapse, and consistent energy absorption. Furthermore, the peak force is only moderate. (Dagdeviren et al., 2016)

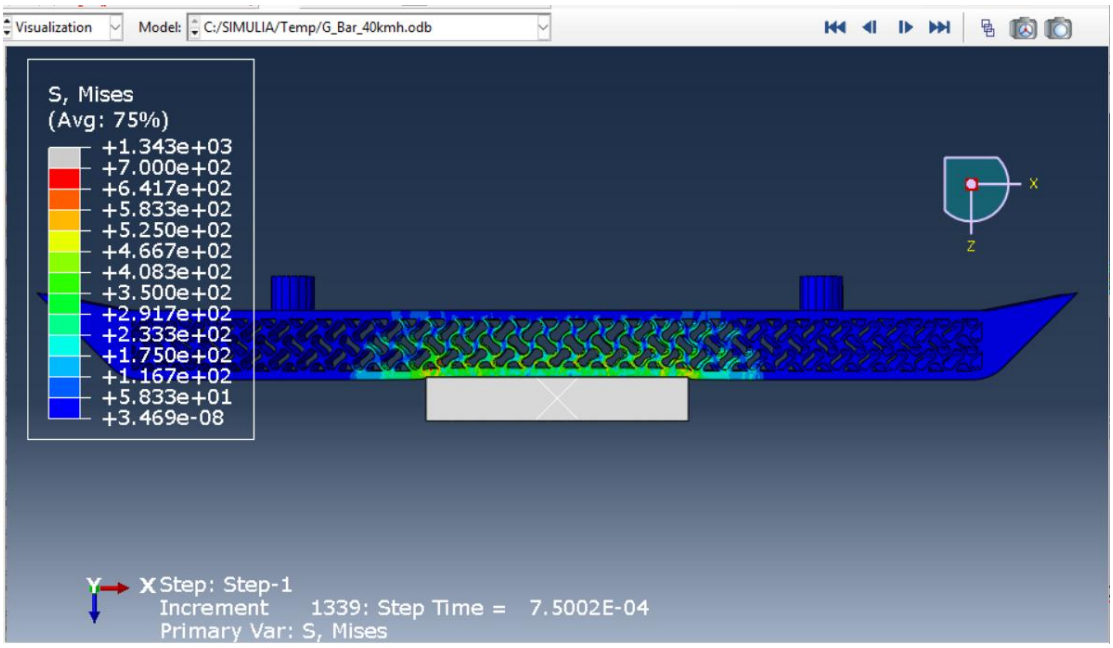

Figure 27 - von Mises Stress Distribution of the Gyroid Structure at 40 km/h

Figure 27 - von Mises stress distribution of the G-Honeycomb crash bar at the onset of impact under 40 km/h loading, showing initial stress development at the contact region.

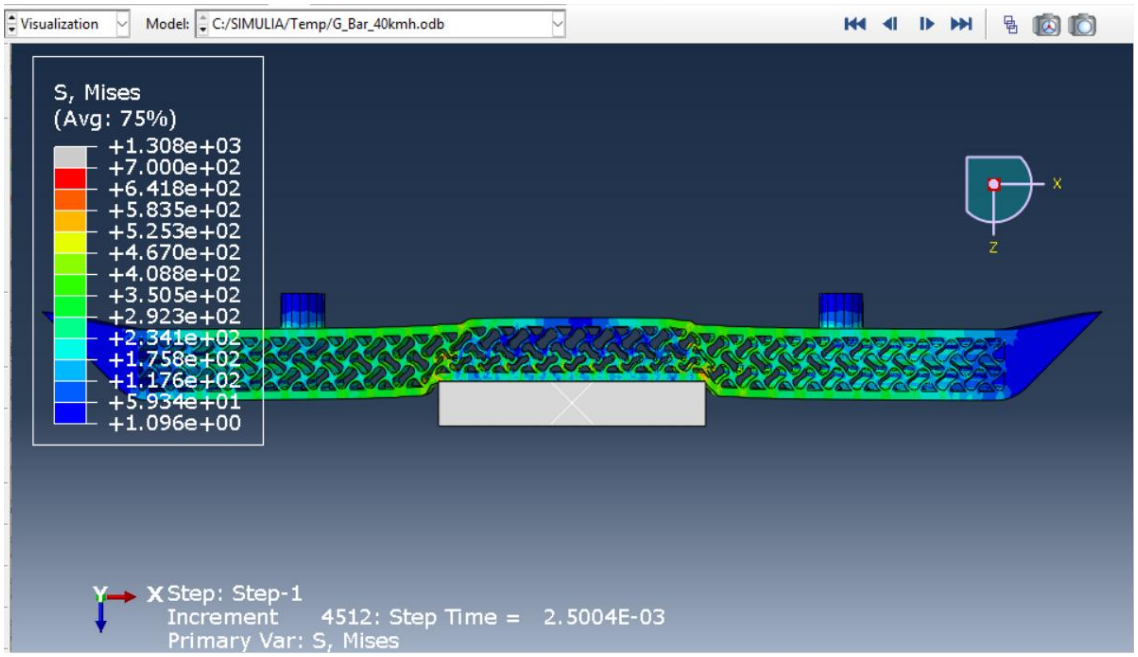

Figure 28 - von Mises Stress Distribution of the Gyroid Structure at 40 km/h

Figure 28 - von Mises stress distribution of the G-Honeycomb crash bar at intermediate deformation stage under 40 km/h loading, showing progressive stress redistribution across the internal core.

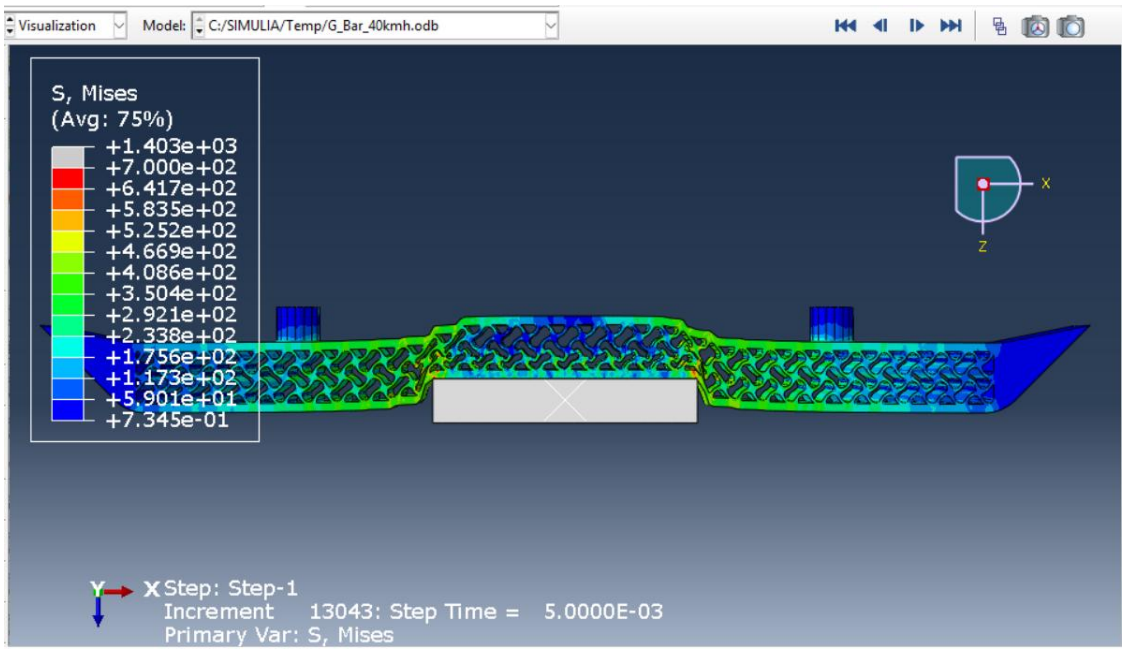

Figure 29 - von Mises Stress Distribution of the Gyroid Structure at 40 km/h

Figure 29 - von Mises stress distribution of the G-Honeycomb crash bar at the onset of densification under 40 km/h loading, showing fully developed stress field and maximum deformation extent.

P-Honeycomb crash bar

The primitive structure shows partially distributed deformation but the behaviour is less uniform than that of the G-Honeycomb, with high stress concentrations appearing early in specific regions, causing localized collapse zones.

The structure absorbs a large amount of energy but the deformation is not as smooth, and there are sharp peaks in the force. This indicates an unstable crushing behaviour where certain regions deform rapidly while others remain less engaged. Figures 30-32 show deformation behaviour of the P-Honeycomb crash bar.

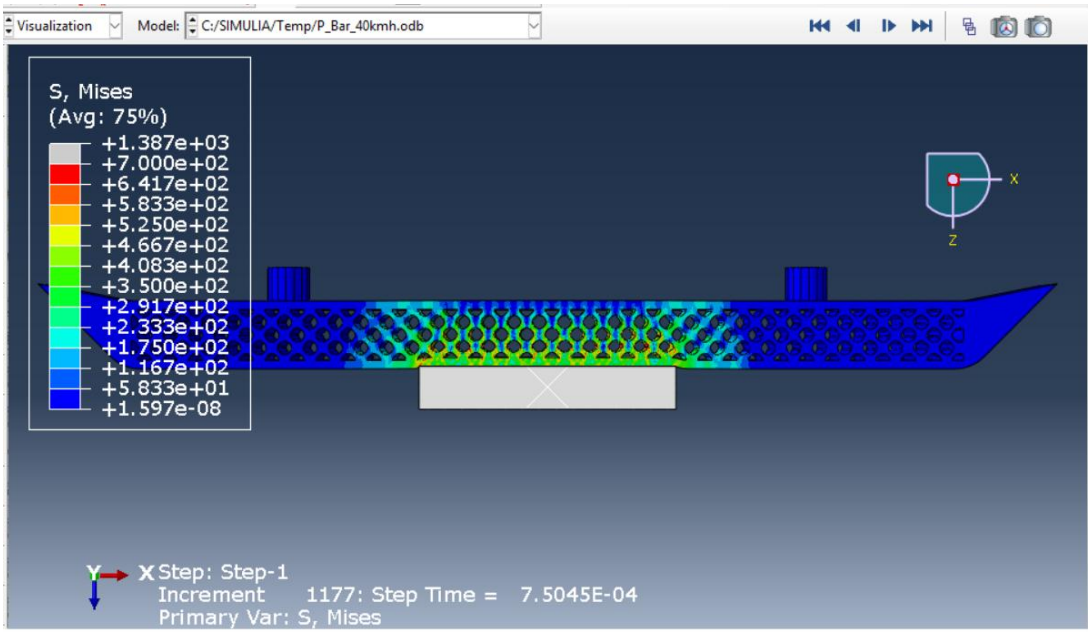

Figure 30 - von Mises Stress Distribution of the Primitive Structure at 40 km/h (Initial Contact Point)

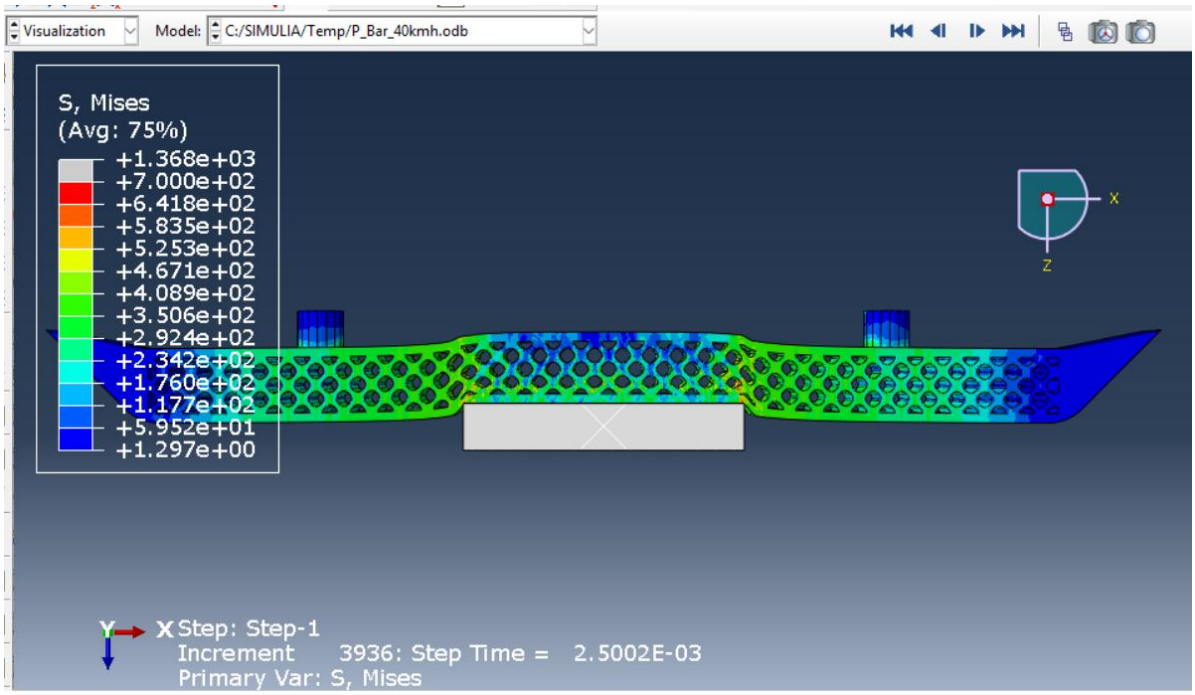

Figure 31 - von Mises Stress Distribution of the Primitive Structure at 40 km/h (Middle Point)

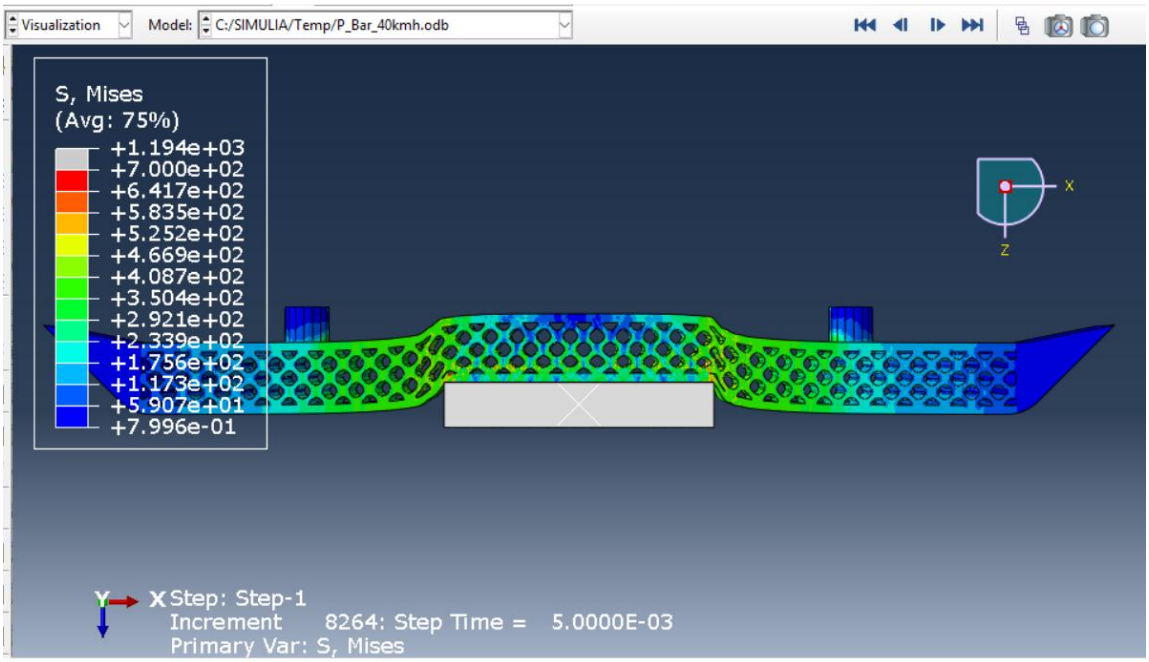

Figure 32 - von Mises Stress Distribution of the Primitive Structure at 40 km/h (Final Point)

Traditional crash bar

The traditional crash bar shows highly localised deformation, mainly at the central impact region. The absence of an internal lattice limits stress redistribution, so only a small portion of the structure undergoes significant deformation.

The majority of the section of the bar is still relatively undeformed and the failure mechanism is dominated by both bending and local yielding. This results in less efficient use of the structure for energy absorption.

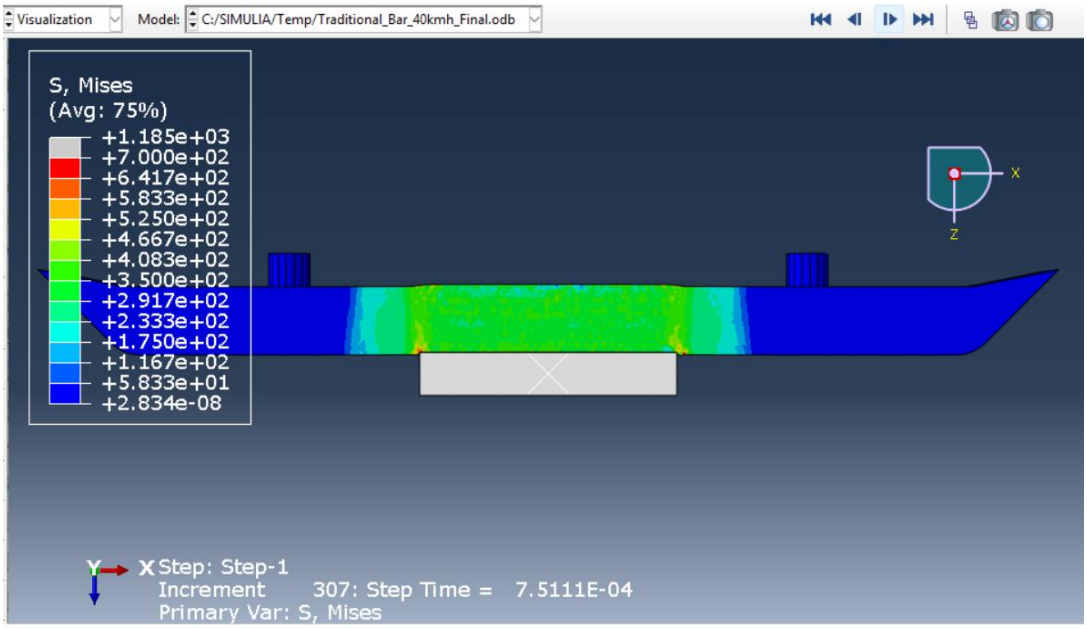

Figure 33 - von Mises Stress Distribution of the Traditional Structure at 40 km/h (Initial Contact Point)

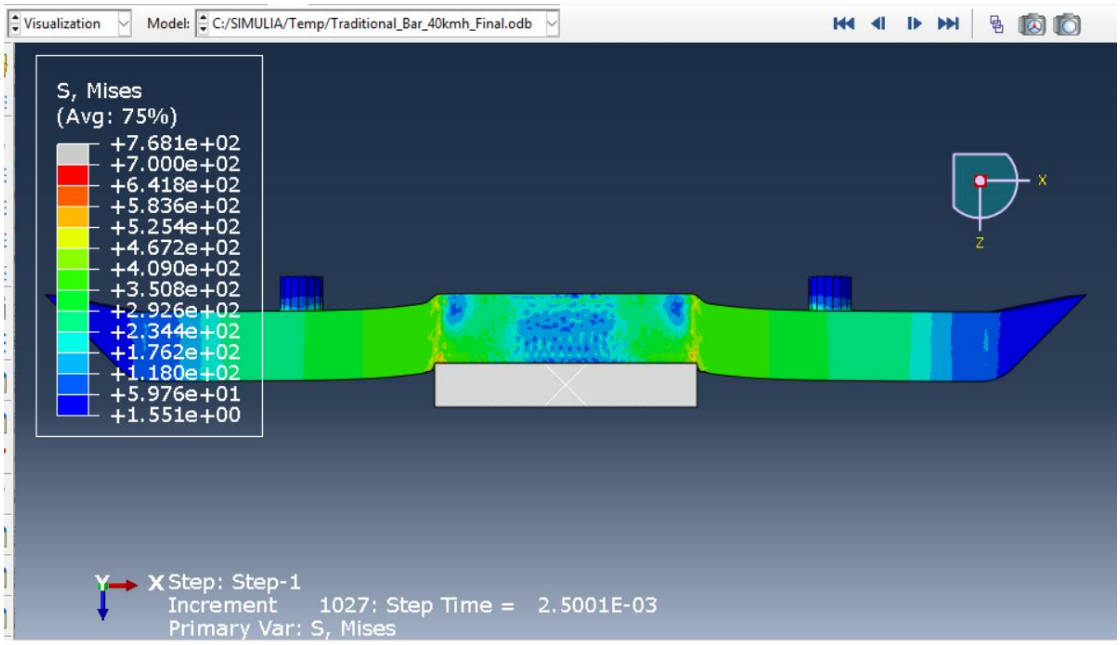

Figure 34 - von Mises Stress Distribution of the Traditional Structure at 40 km/h (Middle Point)

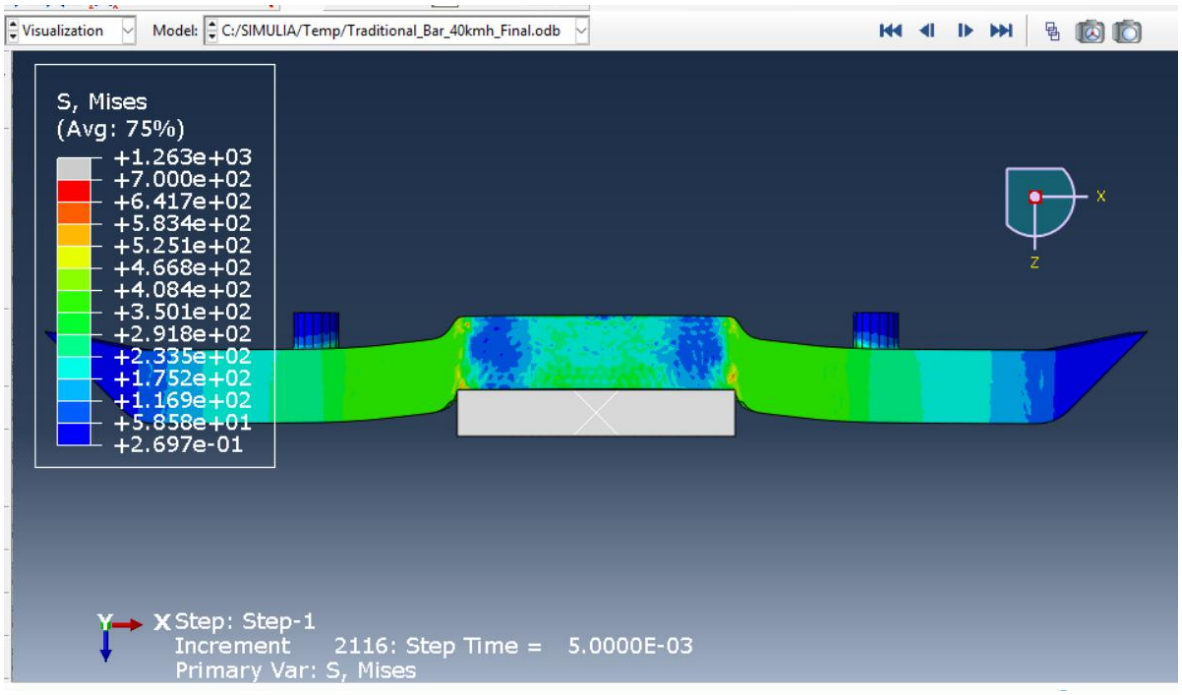

Figure 35 - von Mises Stress Distribution of the Traditional Structure at 40 km/h (Final Point)

4.5.2 Von Mises Stress Distribution at 60km/h

Figures 36 to 43 display the von Mises stress distribution for the G-Honeycomb, P-Honeycomb, and Traditional crash bars under 60 km/h impact loading.

G-Honeycomb crash bar

In the case of the G-Honeycomb structure, progressive and widely distributed deformation is observed at 60 km/h. Stress initially appears at the contact region during the initial stages of deformation and subsequently spreads throughout the G-Honeycomb core as the deformation increases.

At higher deformation a smooth crushing zone forms at the centre of the structure, with surrounding regions also participating in deformation. The stress distribution remains relatively uniform with no extreme concentration at a single point. This indicates that the G-Honeycomb structure maintains stable deformation even at higher velocity allowing efficient load redistribution.

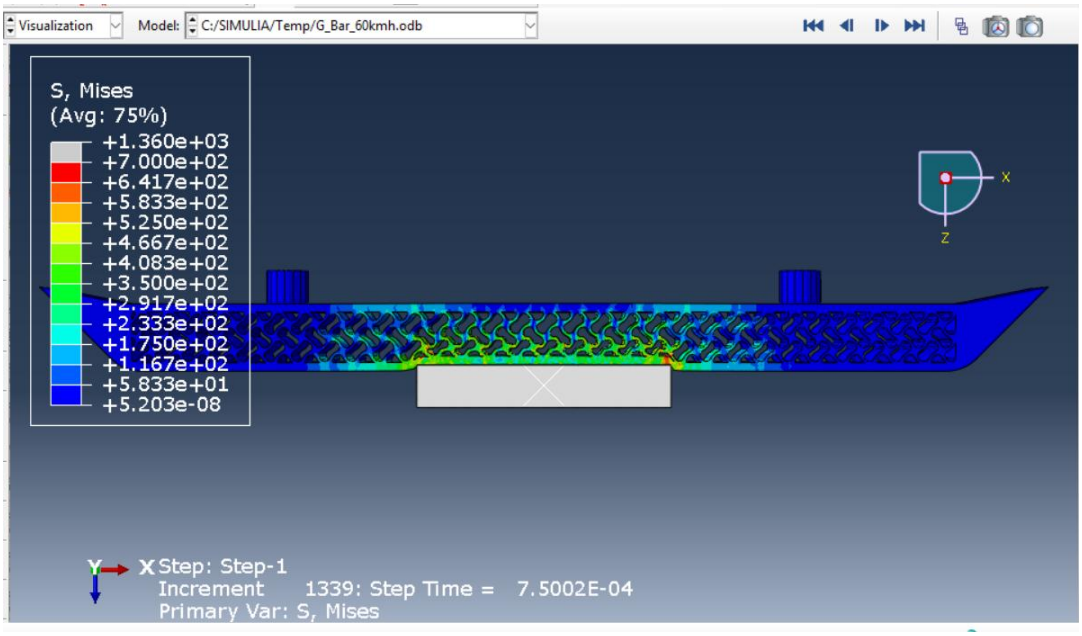

Figure 36 - von Mises Stress Distribution of the Gyroid Structure at 60 km/h (Initial Contact Point)

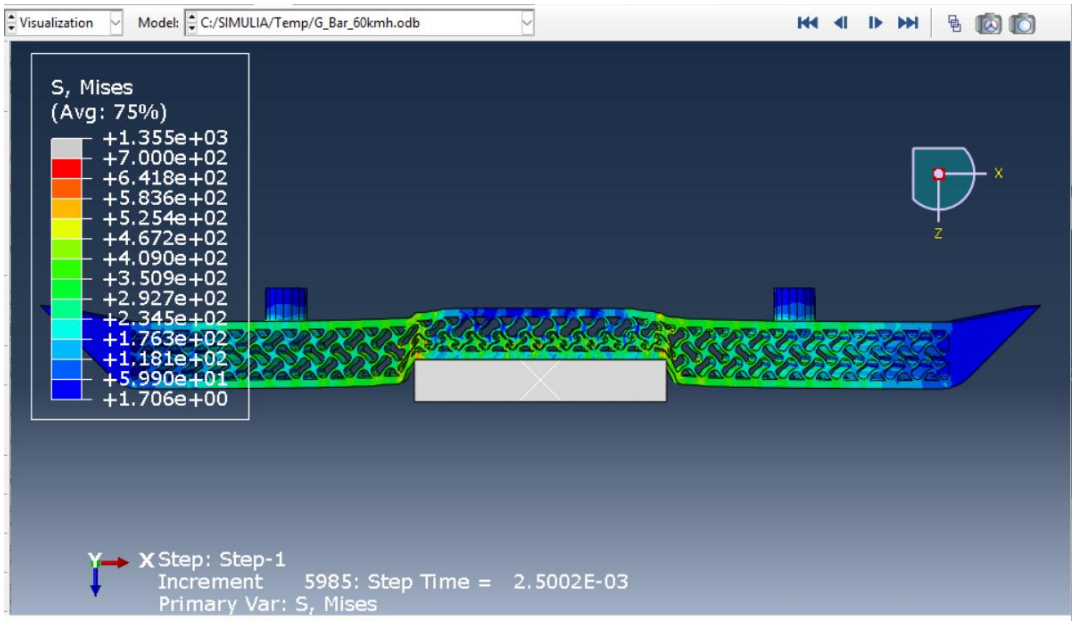

Figure 37 - von Mises Stress Distribution of the Gyroid Structure at 60 km/h (Final Point)

P-Honeycomb crash bar

The P-Honeycomb structure shows a strong stress concentration at the initial impact region, which is higher than the G-Honeycomb structure. Multiple stress regions appear especially near the center as deformation progresses.

The collapse behavior was not uniform, where localized zones were observed with higher deformation while other areas were less active. Even at later stages, stress is not evenly distributed across the structure.

This confirms that the P-Honeycomb structure undergoes localized and less stable deformation, especially under higher impact velocity.

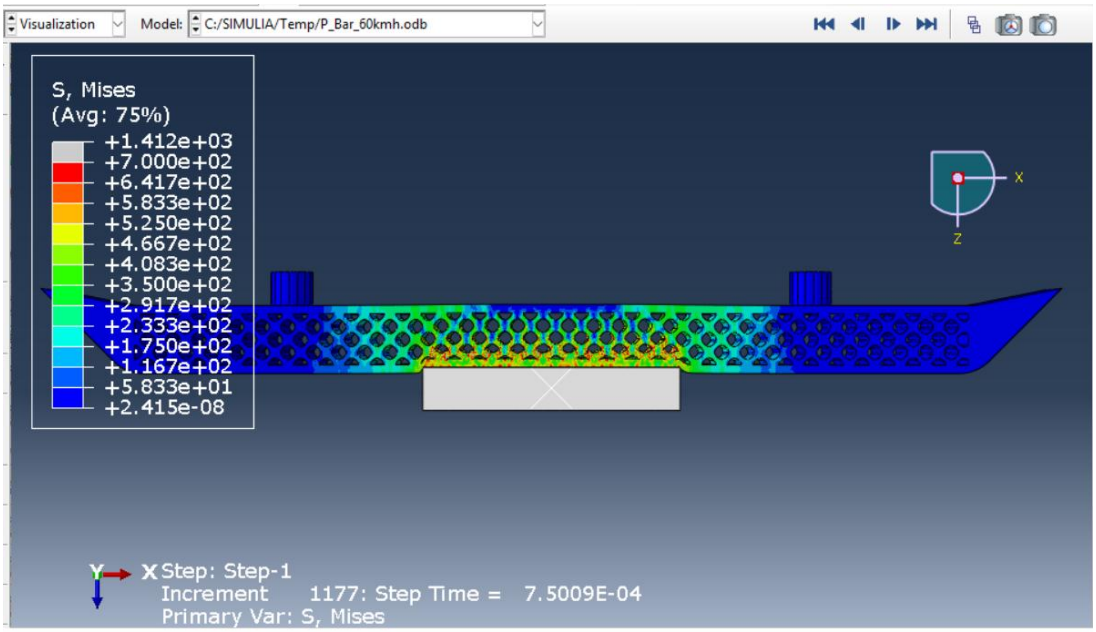

Figure 38 - von Mises Stress Distribution of the Primitive Structure at 60 km/h (Initial Contact Point)

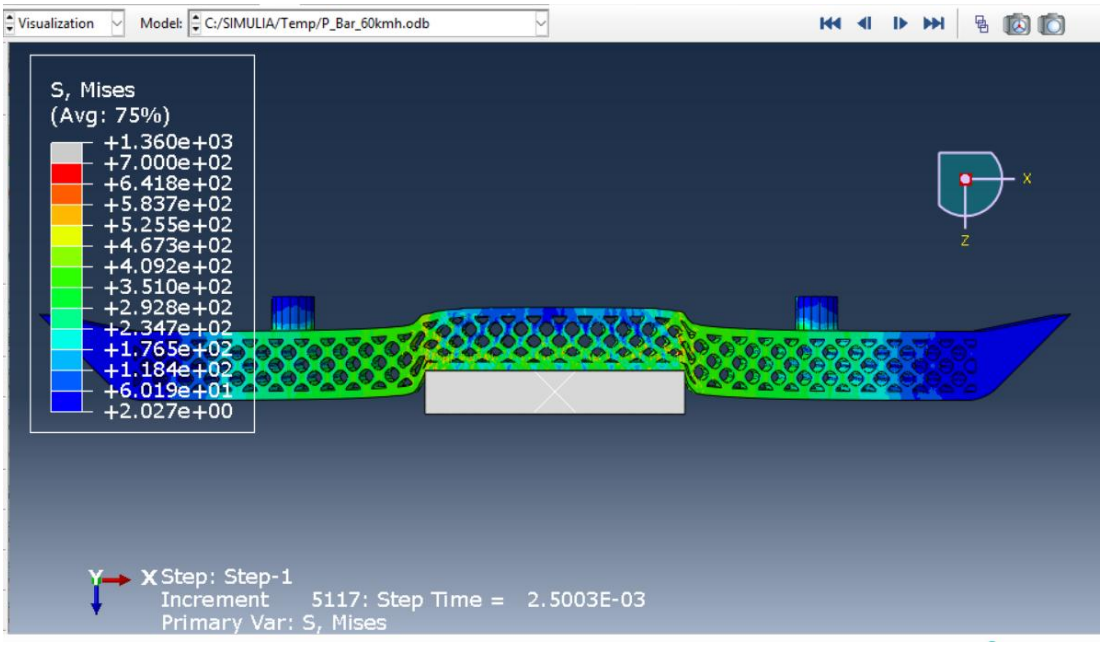

Figure 39 - von Mises Stress Distribution of the Primitive Structure at 60 km/h (Middle Point)

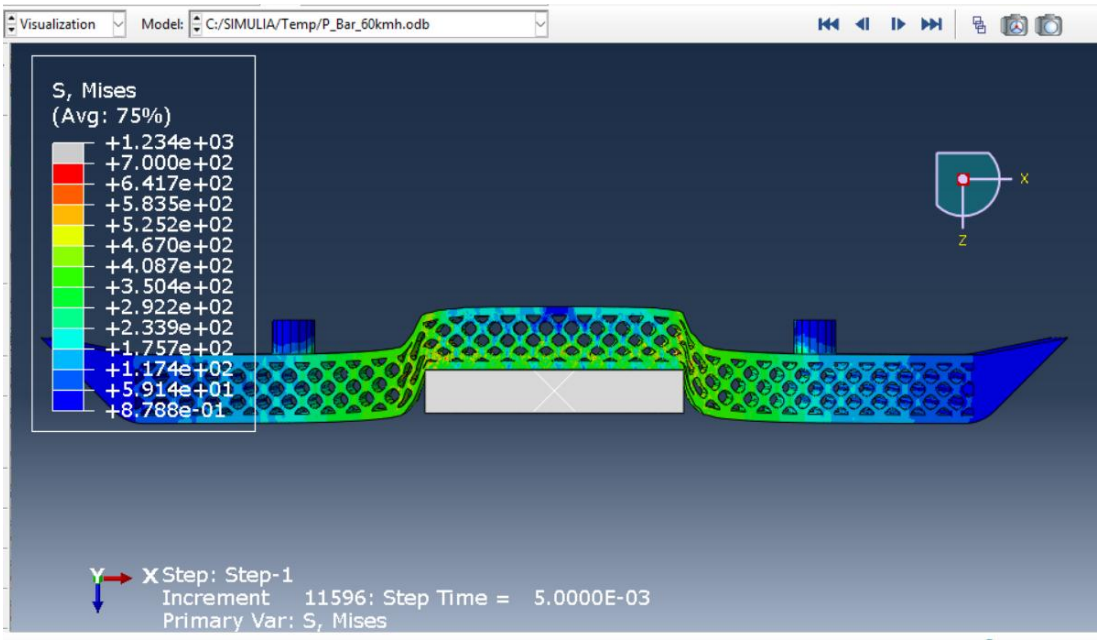

Figure 40 - von Mises Stress Distribution of the Primitive Structure at 60 km/h (Final Point)

Traditional crash bar

The traditional crash bar exhibits highly localized deformation at the center. At the initial stage, stress is concentrated directly above the rigid body. As deformation progresses, the structure mainly undergoes bending and compression in a limited region, while the outer sections remain relatively undeformed. Even at higher displacement, stress distribution does not spread significantly along the length.

This shows that the traditional structure has poor stress distribution capability under high-speed impact.

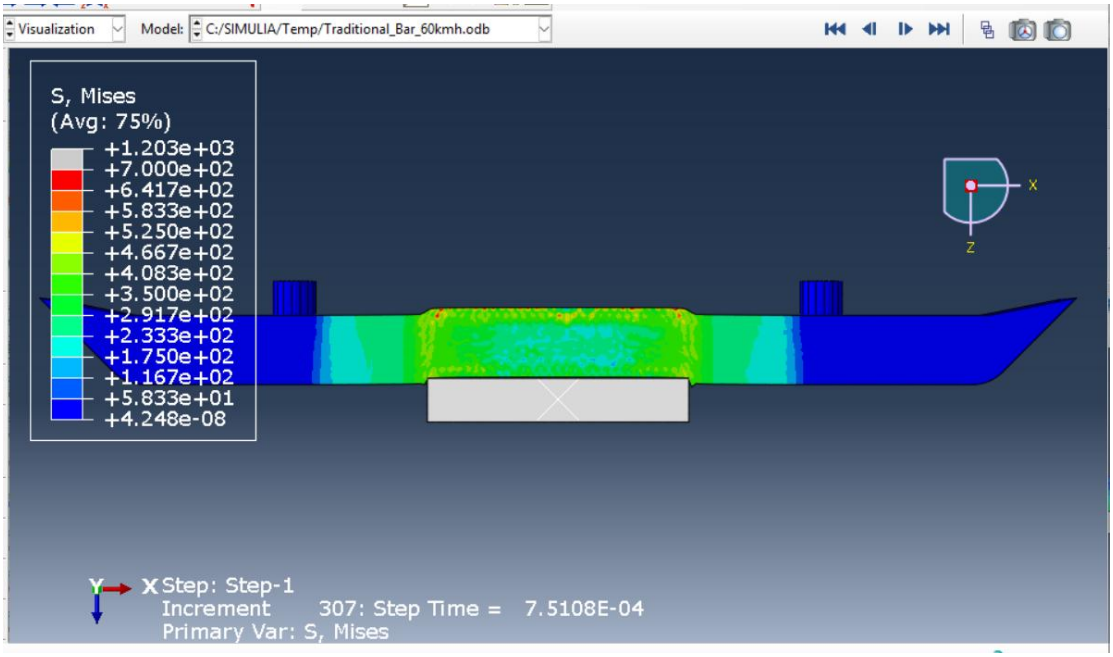

Figure 41 - von Mises Stress Distribution of the Traditional Structure at 60 km/h (Initial Contact Point)

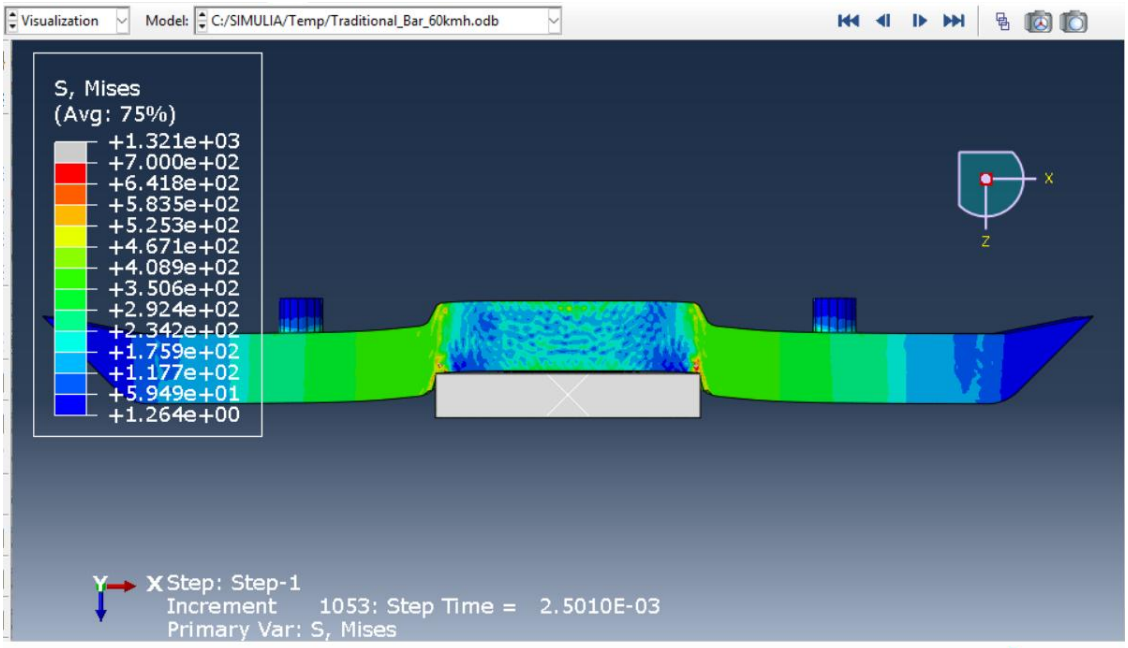

Figure 42 - von Mises Stress Distribution of the Traditional Structure at 60 km/h (Middle Point)

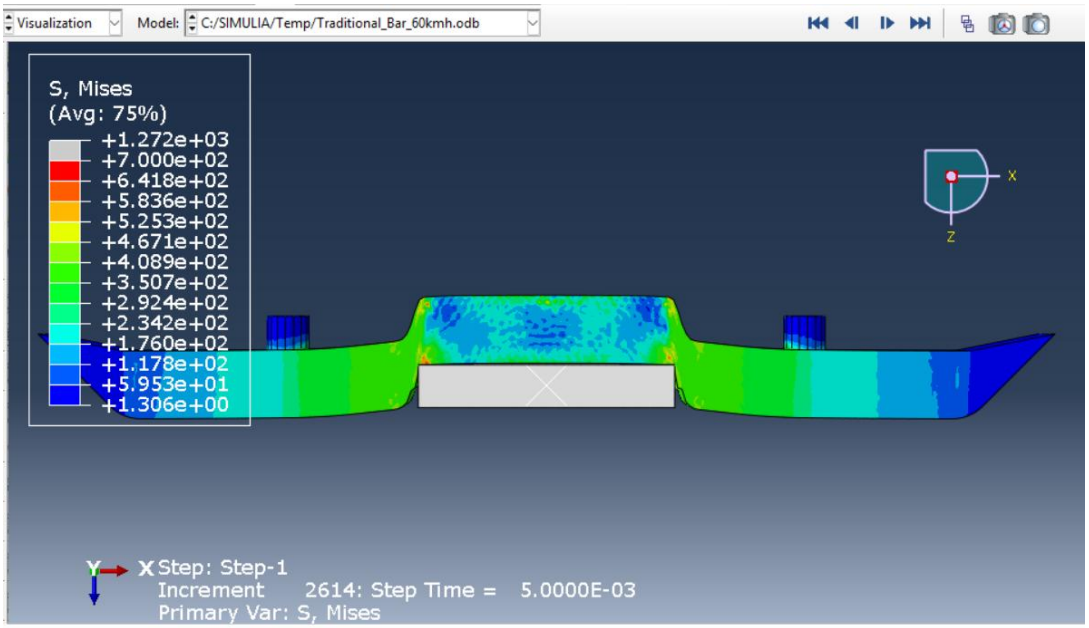

Figure 43 - von Mises Stress Distribution of the Traditional Structure at 60 km/h (Final Point)

4.5.3 Equivalent Plastic Strain (PEEQ)

Figures 44 to 49 present the distribution of equivalent plastic strain (PEEQ) at the onset of densification for the G-Honeycomb, P-Honeycomb, and traditional crash bar structures. The densification point was identified from the force displacement curves as the stage where the force begins to rise sharply after the plateau region.(Rapaka et al., 2021)

G-Honeycomb crash bar

At 40 km/h, the PEEQ contour shows low to moderate plastic strain distributed across the entire G-Honeycomb core. The deformation starts at the central contact zone and spreads along the length of the structure. Most of the geometry remains in blue to green levels, indicating gradual and uniform plastic deformation.

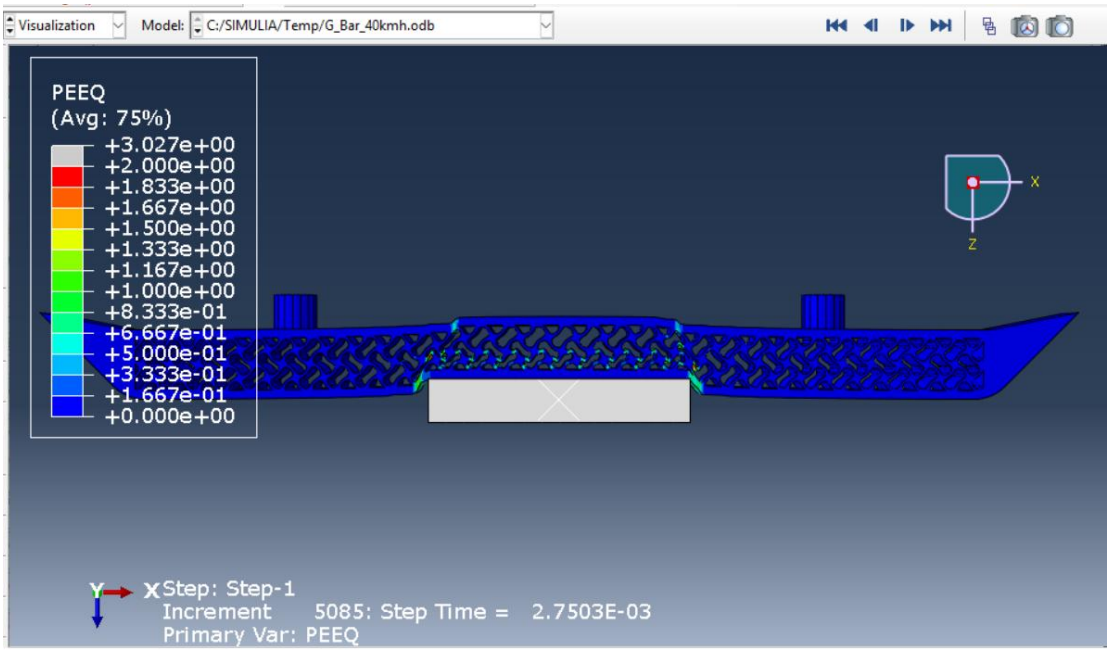

Figure 44 - PEEQ distribution: G-Honeycomb crash bar at 40 km/h.

At 60 km/h, the plastic strain increases, with higher values appearing near the impact region. Compared to the 40 km/h contour, the area of the more yellow/green regions has increased. However, the deformation is still spreading across the lattice indicating progressive collapse.

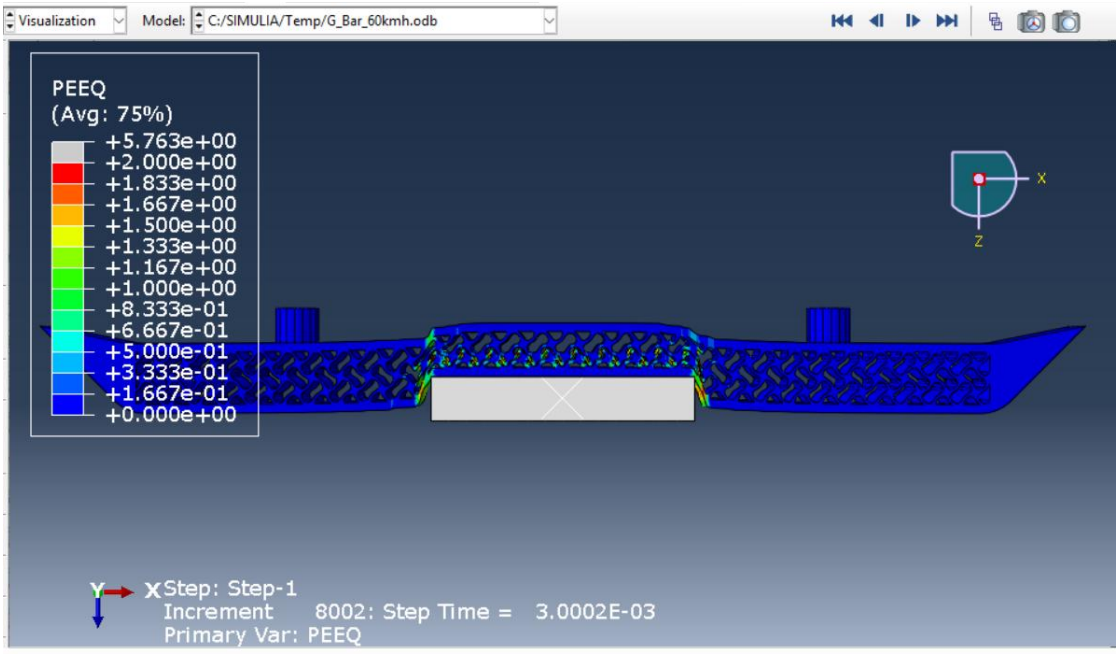

Figure 45 - PEEQ distribution: G-Honeycomb crash bar at 60 km/h.

P-Honeycomb crash bar

At 40 km/h, the PEEQ distribution shows clear concentration near the contact area. Higher strain values (green to yellow) are also observed in the central region of the structure. In contrast, much of the structure remains mostly blue. This indicates that deformation is more localized compared to the G-Honeycomb structure.

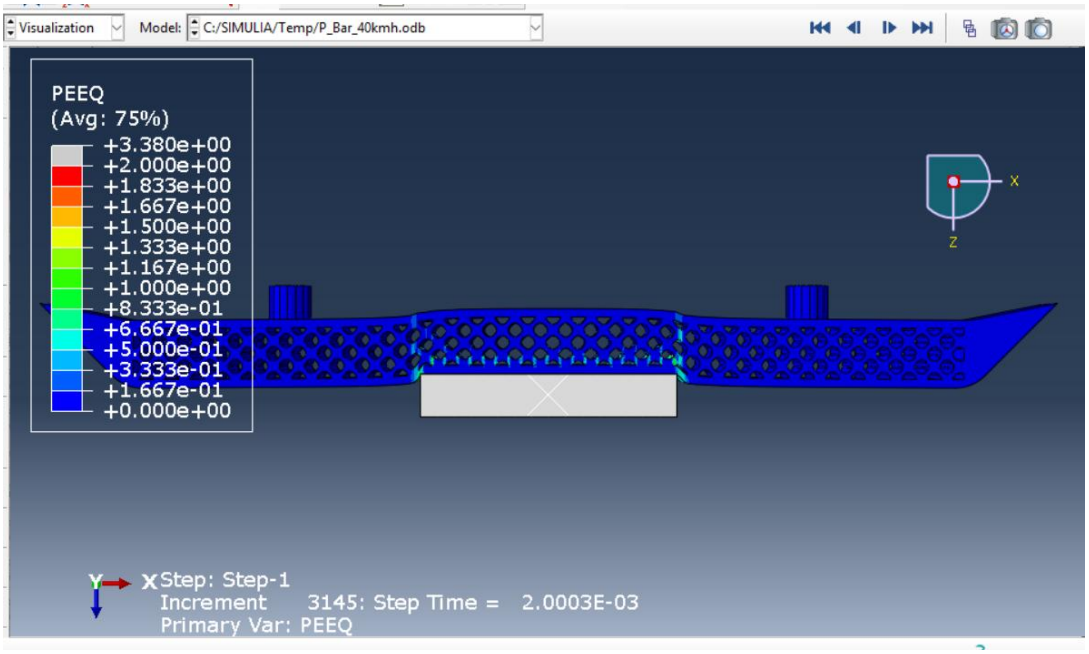

Figure 46 - PEEQ distribution: P-Honeycomb crash bar at 40 km/h.

When impacting at 60 km/h the strain concentration becomes stronger, with the central area recording the highest values and the area of deformed zone increasing in size. Nevertheless a large proportion of the structure remain to record low levels of strain confirming uneven deformation behavior.

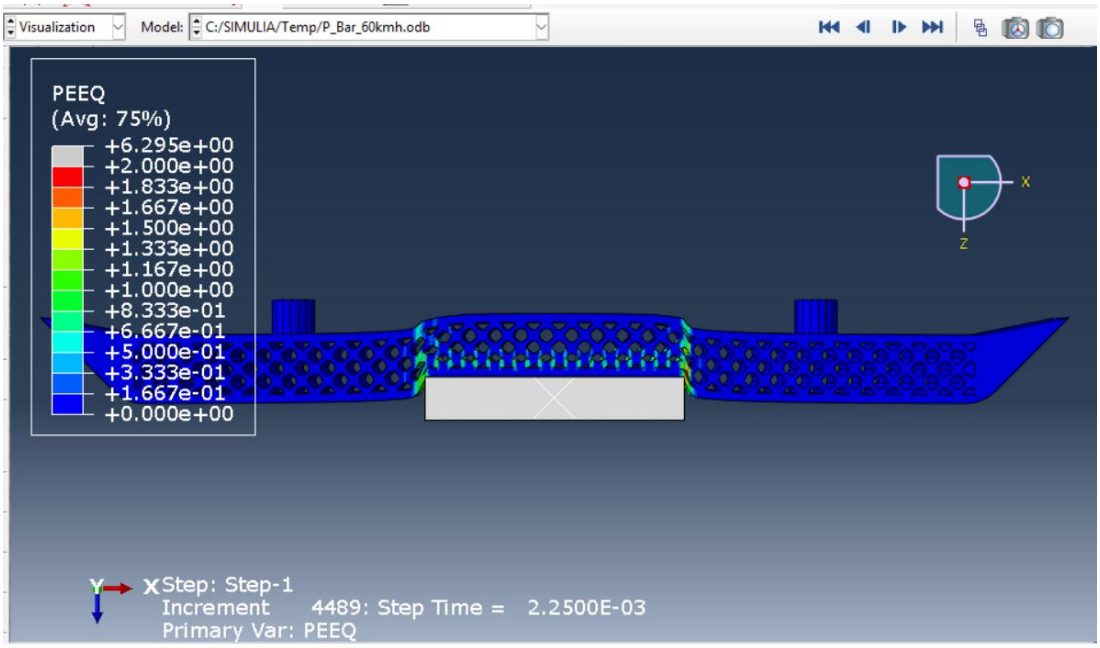

Figure 47 - PEEQ distribution: P-Honeycomb crash bar at 60 km/h

Traditional crash bar

At 40 km/h, the PEEQ contour of the structure shows very limited deformation, and most of the structure remains in blue, indicating highly localized plastic deformation limited to a very thin band around the contact point. At 60 km/h, the same pattern continues, with slightly higher strain values at the center. There remains confined deformation in a small region with the majority of the structure showing minimal plastic strain.

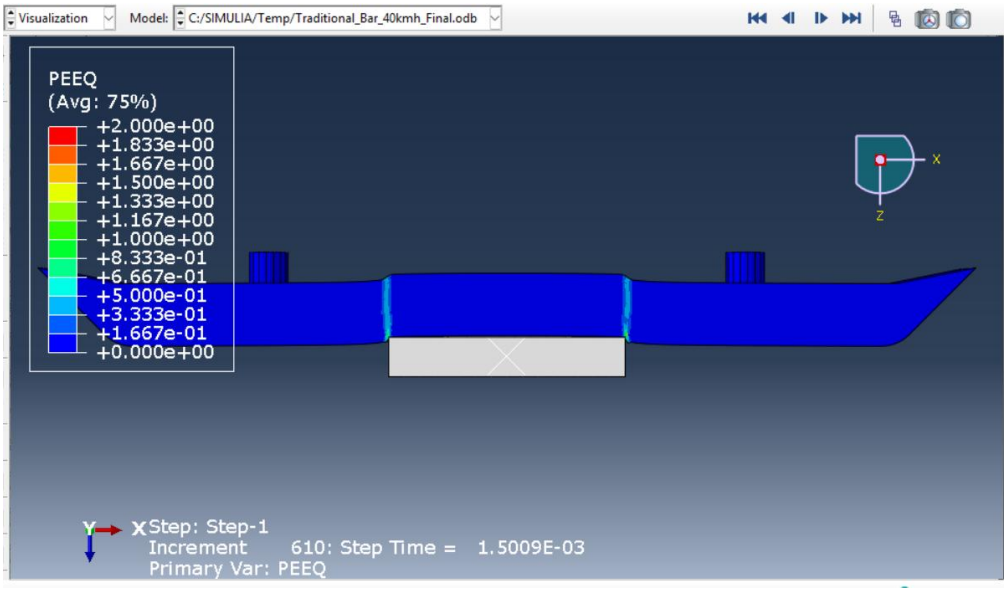

Figure 48 - PEEQ distribution: Conventional crash bar at 40 km/h.

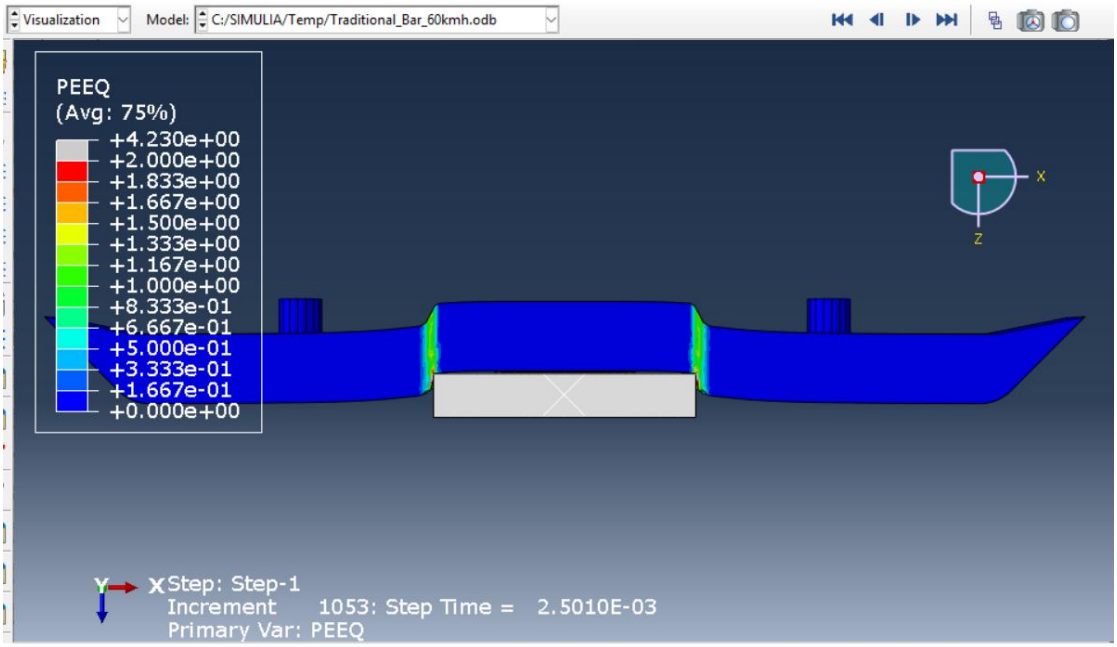

Figure 49 - PEEQ distribution: Conventional crash bar at 60 km/h.

4.6 Velocity Sensitivity Analysis

The influence of the impact velocity on the dynamic behavior of the structures has been studied on the basis of the Dynamic Amplification Ratio.

$$DAR = \frac{Value\ at\ 60km/h}{Value\ at\ 40km/h}$$

The DAR results indicate that the response of the structures varies significantly with velocity. The G-Honeycomb and conventional crash bar show a notable increase in energy absorption, with EA and SEA values increasing by factors of 1.73 and 1.76, respectively. The P-Honeycomb showed the lowest velocity scaling in energy absorption, with a DAR of 0.91. The peak crushing force increased for Gyroid and traditional structures, most for the traditional structure at a 1.84-fold increase. In contrast, the peak force for the Primitive structure decreased by 0.53-fold. The mean crushing force showed only very slight variations between the three geometries and showed limited sensitivity to velocity. The results revealed that the crush force efficiency decreased for the Gyroid and traditional models, whereas for the Primitive

model there was a slight increase. Overall, the effect of velocity varies across different structural configurations and performance metrics.

Table 9 provides the DAR values for key performance metrics: energy absorption (EA), specific energy absorption (SEA), peak crushing force (PCF), mean crushing force (MCF), and crush force efficiency (CFE).

Table 9 - Dynamic Amplification Ratio (DAR) for key crashworthiness metrics.

Structure	EA	SEA	PCF	MCF	CFE
Gyroid (G)	109.2 / 63.3 = 1.73	9.6 / 5.55 = 1.73	3.49 / 2.53 = 1.38	1.6 / 1.46 = 1.10	0.46 / 0.58 = 0.79
Primitive (P)	127 / 139.4 = 0.91	9.4 / 10.3 = 0.91	7.04 / 13.4 = 0.53	1.9 / 3.45 = 0.55	0.27 / 0.26 = 1.04
Traditional	108.6 / 61.8 = 1.76	10.75 / 6.1 = 1.76	13.4 / 7.30 = 1.84	1.6 / 1.5 = 1.07	0.12 / 0.21 = 0.57

4.7 Energy Balance Verification

The accuracy and numerical stability of the simulations were evaluated using the energy conservation principle. In explicit dynamic analysis, the total energy of the system should remain approximately constant throughout the simulation. The energy balance can be expressed as:

$$ETOTAL=ALLIE+ALLKE+ALLAE$$

Here, ALLIE denotes the internal energy, ALLKE denotes the kinetic energy, and ALLAE denotes the artificial strain energy of the system, respectively. The plastic dissipation energy (ALLPD) is included within the internal energy and therefore is not considered separately in the energy balance equation. (Boulbes, 2020)

Figure 50 to 55 show in the verification graphs below.

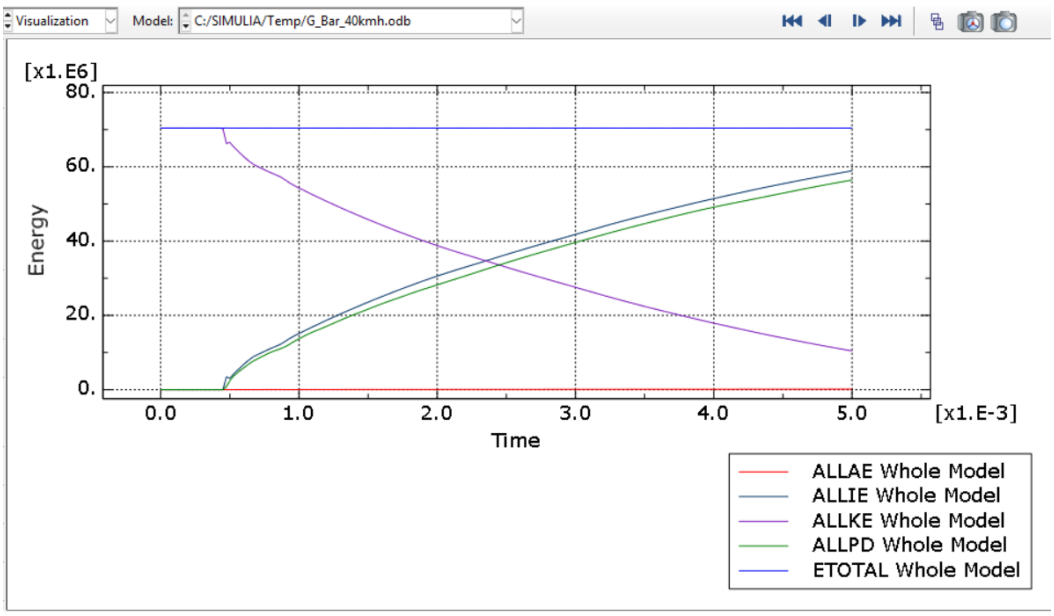

Figure 50 - Energy Balance Verification of Gyroid bar at 40km/h

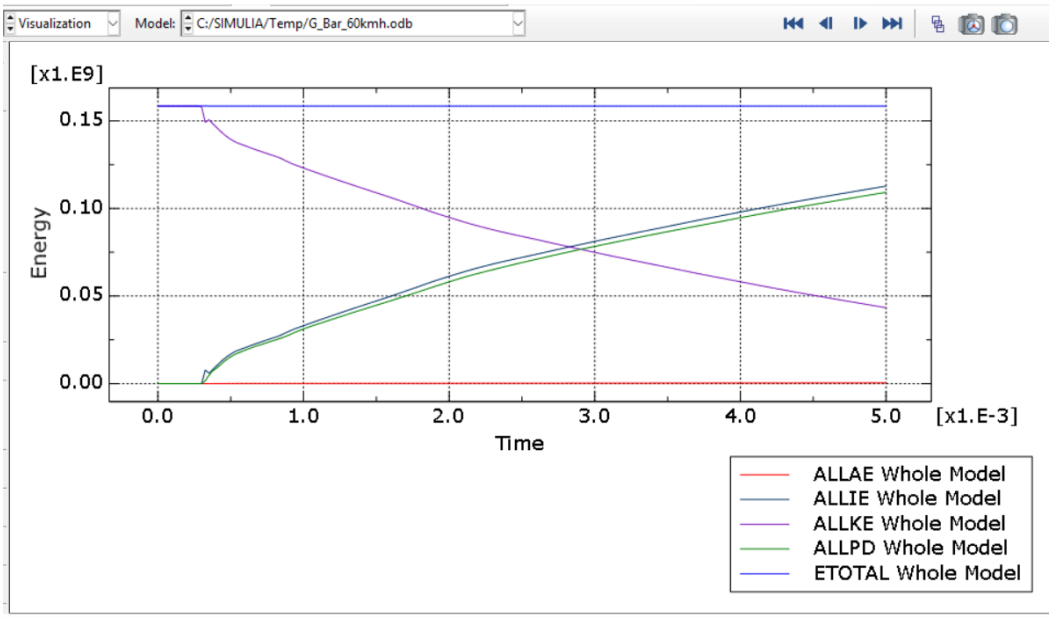

Figure 51 - Energy Balance Verification of Gyroid bar at 60km/h

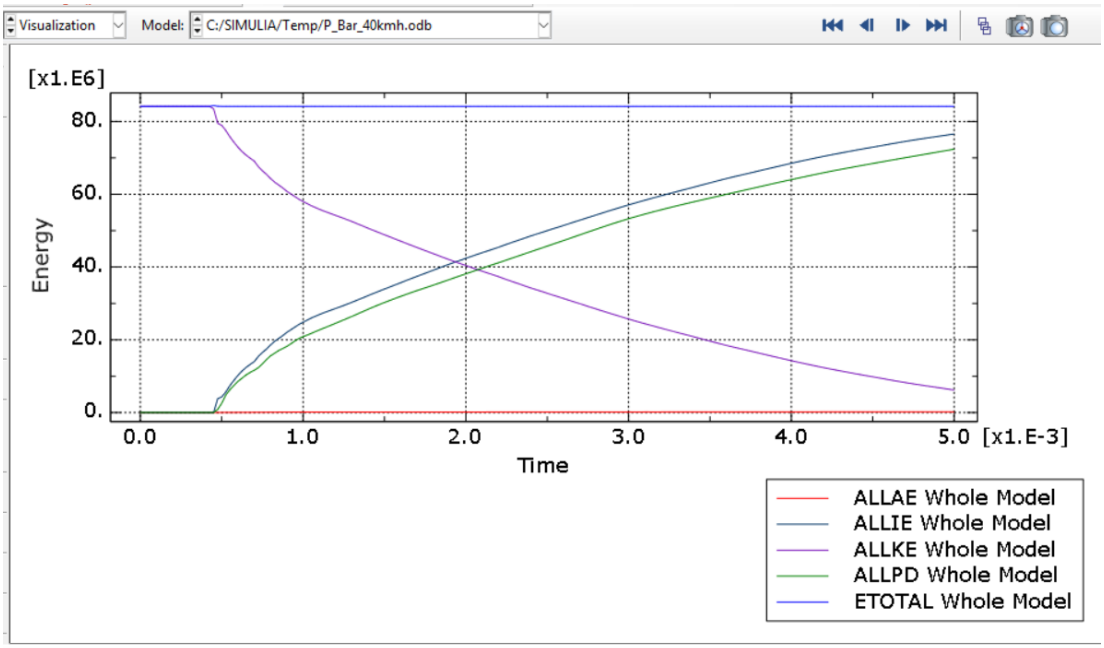

Figure 52 - Energy Balance Verification of Primitive bar at 40km/h

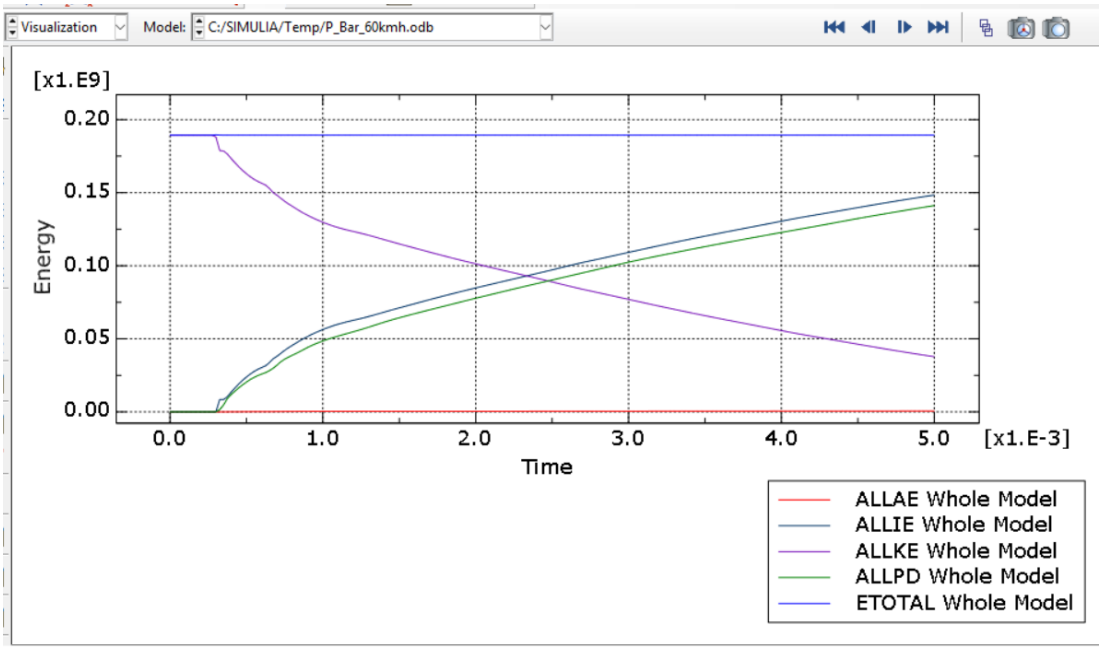

Figure 53 - Energy Balance Verification of Primitive bar at 60km/h

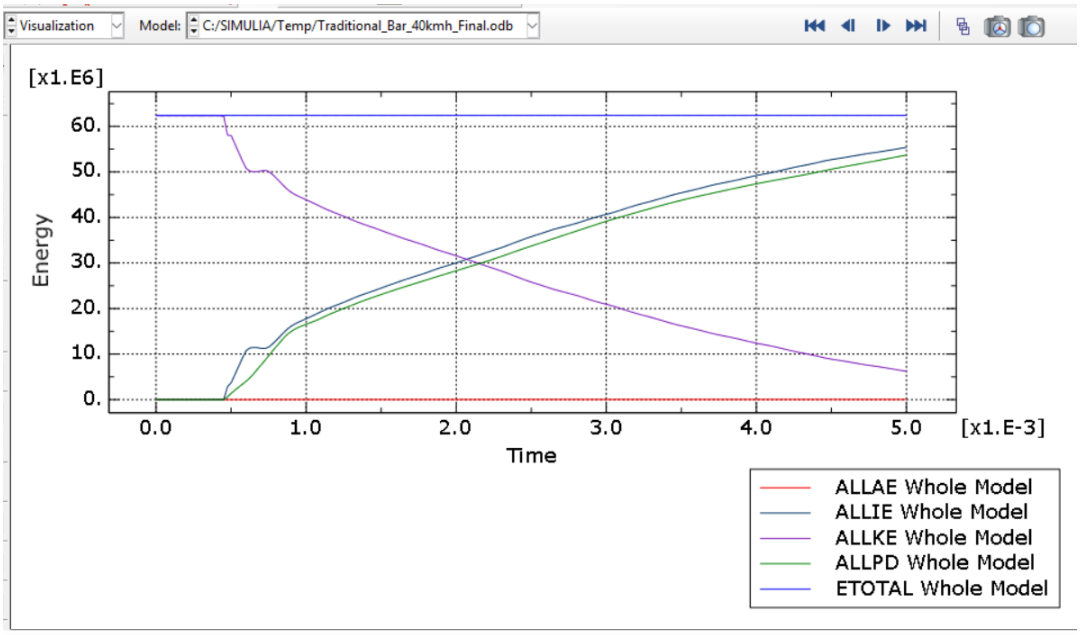

Figure 54 - Energy Balance Verification of Traditional bar at 40km/h

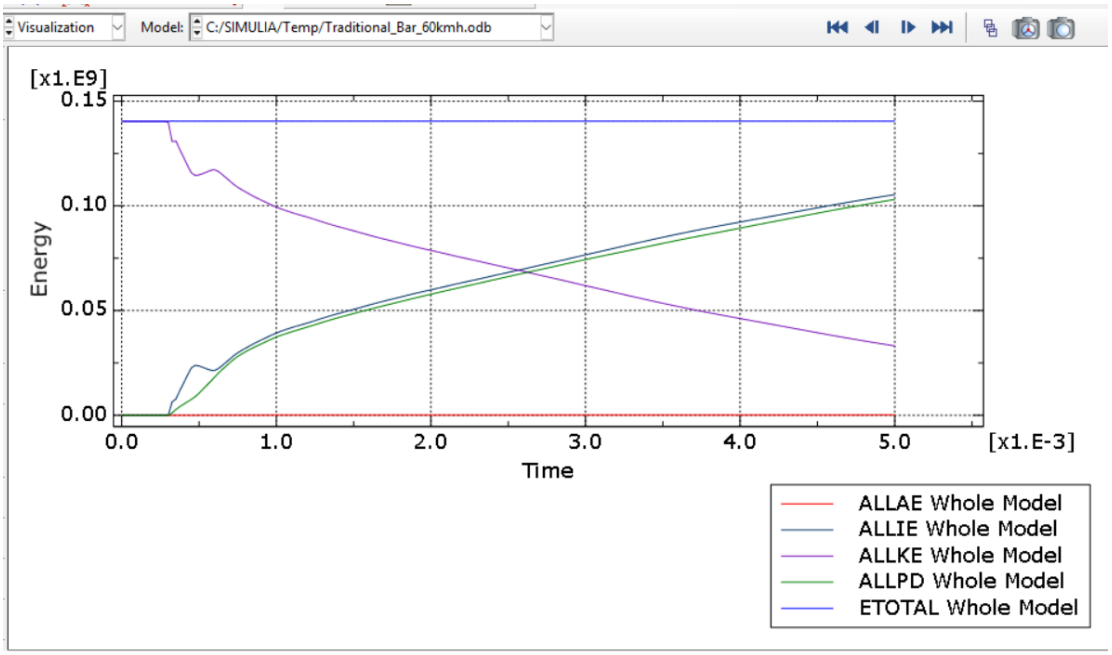

Figure 55 - Energy Balance Verification of Traditional bar at 60km/h

After reviewing all of the simulation results the following trends were observed. The total energy (ETOTAL) remained nearly constant for all the cases, confirming that energy is conserved throughout the simulation. The solution was both stable and physically consistent. The kinetic energy ALLKE is high at the beginning and then drops down as deformation is built up, demonstrating that kinetic energy is effectively converted into deformation energy. The internal energy ALLIE increases steadily along

the simulation history, indicating that the structure is absorbing energy as it crushes. The increase of internal energy ALLIE is very close to the total plastic dissipation energy ALLPD. This is a desired crashworthiness behavior for a structure designed to crush favorably. This relationship is expressed as ALLIE ≈ ALLPD, which confirms that most of the internal energy is dissipated through permanent plastic deformation rather than elastic recovery. Regarding numerical accuracy, the accuracy of the results has also been checked by calculating the artificial energy (ALLAE) which is found to be close to zero and to be significantly lower than the internal energy. The ratio of the ALLAE to the internal energy is well below 5%, validating the applied mass scaling approach. The energy curves show a good energy transfer from the kinetic energy to the internal (plastic) energy and a total energy conservation. Therefore, the results of the simulation are considered reliable and suitable for further analysis.

5 DISCUSSION

While many results show trends consistent with established behavior for damage and response, it is important to consider the underlying mechanisms responsible for the dynamic behavior of structures subject to axial loading, where the impact force acts along the longitudinal Z-axis of the crash bar, in a crash scenario. The effects of internal structure or topology upon the response of the three configurations studied are greater than those induced by variations in the dynamic crash environment, such as, crash velocity.

The force displacement response recorded at both test velocities for the G-Honeycomb consisted of a steadily increasing force reaching a moderate maximum, followed by a fluctuating plateau. This behaviour arises from the cross-sectional geometry derived from the Gyroid level set equation, which contains no straight channels. As a result, every internal load path has curvature and out of plane bending, leading to a deformation mechanism whereby several curved ligaments across the cross section are simultaneously subjected to deformation. This avoids the typical localized buckling of discrete columns observed in structures with straight channels. A typical von Mises stress distribution across the section is shown in Fig. 27. At the onset of impact, high stress developed progressively across the full length of the G-Honeycomb crash bar as the internal core began to deform. As the loading continued, this region of high stress transferred along the section from the impact face to the distal end of the specimen. The deformation mode and corresponding plastic strain distribution were consistent with previous results. At 40 km/h, the G-Honeycomb core experienced low to moderate strain levels, with plastic work distributed broadly throughout the internal structure. At 60 km/h, overall strain magnitudes increased; however, the distribution remained relatively uniform across the core. The average peak crushing force was found to be 2.53 MN at 40 km/h and 3.49 MN at 60 km/h. These values correspond to CFE values of 0.58 and 0.46 respectively. The highest CFE values for any of the tested structures were achieved at both test velocities. The 58% CFE at 40 km/h indicates that the mean crushing force is 0.58 times the peak force, meaning that this structure achieves the most desirable force profile for a crash energy absorber; high average force levels with minimal peak forces. From an occupant safety perspective, the G-Honeycomb delivers the least severe instantaneous deceleration within the vehicle

structure due to the peak force seen at the beginning of the crush stroke, whilst still benefitting from the full crush stroke energy absorption.

The P-Honeycomb collapses in a very different manner to the other structures, and its energy absorption and efficiency must therefore be discussed accordingly. The 2D cross sectional profile of the P-Honeycomb contains large open regions connected through narrow nodal junctions, derived from the Schwartz Primitive level-set equation. The 2D cross-sectional profile of the P-Honeycomb includes straight load-carrying wall segments aligned with the loading axis. The high axial compression stiffness generated by these aligned walls produces a high initial force peak of 13.4 MN at 40 km/h. This high force however is generated over a very small displacement of 5.56 mm due to a sharp force spike occurring due to buckling of the load carrying columns. This sudden softening of the structure results in a sharp decrease of force as the structure is allowed to deform through the more compliant inter cavity necks. Stress contour plots pick out localized stress concentrations but then allow variability over longer distances. For the P-Honeycomb structure the first instances of high stress concentrations were found to be located within discrete localized areas of the lattice. The distributions of PEEQ show high green to yellow strains concentrated within the centre of contact areas extending into the higher-pressure areas around them. It can be seen that the majority of the structure's volume is associated with the peripheral regions of the components, yet these regions are responsible for a very small percentage of energy dissipation. The efficiency of the load-carrying behaviour is reflected in the CFE, which was only 0.26 for the P-Honeycomb. This P-Honeycomb had achieved a total strain energy release of 139.4 kJ to 40 km/h. The localized nature of the first peak force for the P-Honeycomb structure is striking. The maximum force achieved was 13.4 MN within the contacting area. This was 5.2 times greater than that obtained for the G-Honeycomb at the same test velocity. The first peak force for the P-Honeycomb structure will initially have travelled with the structure through the car chassis, seat, door trims, floor structure and on to any back seat occupants. The resulting acceleration pulse would be associated with higher risk of thoracic and head injury according to current methods of crash assessment. It is not just a case of achieving the greatest amount of energy dissipation within future car structures for them to attain superior crashworthiness. The way this energy is dissipated is of equal

importance. It must be achieved in a progressive rather than catastrophic manner, or in a uniform rather than impulsive fashion.

The conventional crash bar represents the baseline case of localised, bending-dominated collapse, in which the absence of an internal lattice results in a plastic hinge forming at the impact point rather than progressive distributed crushing. The conventional crash bar, consisting of a hollow cylindrical tube, was evaluated under impact loading at two velocities of 40 km/h and 60 km/h. The conventional crash bar has no internal lattice structure to enforce lateral stress redistribution, and therefore the load-displacement response is governed by localised collapse behaviour. Significant plastic deformation occurred in a small area at the center of impact. The strain PEEQ distributions supported this finding, and the geometry yielded into a localized plastic hinge rather than undergoing global fold induced collapse. The test results showed a sharp initial force peak of 7.30 MN at 40 km/h at a displacement of 5.57 mm, followed by a very rapid decline in force. The outer regions of the bar remained largely undeformed for the remainder of the test. Crush Force Efficiency for the lightest configuration was 0.21 at 40 km/h, which is the lowest CFE of the three configurations. This structure provides most of its resistance in a short single stroke and then offers only a minimum of static load carrying capacity for the remainder of the stroke.

Effect of different impact velocities on crashworthiness responses of Gyroid and Primitive topologies was investigated. Both designs have their own merits and demerits at 40 km/h and 60 km/h impact velocities. The results obtained in this study provide valuable insights on the crashworthiness responses of these two designs at different velocity conditions and are important for engineering design practicability. The G-Honeycomb performed consistently well and with improved energy absorption at the higher impact velocity of 60 km/h. The energy absorption (EA) of the structure was increased from 63.3 kJ to 109.2 kJ. The Dynamic Amplification Ratio for energy absorption and specific energy absorption was 1.73. The average peak and mean crushing force increased by 1.38 and 1.10 times, respectively. The crush force efficiency decreased from 0.58 to 0.46, though it should be noted that this reduction is a plausible physical explanation rather than a mechanism directly demonstrated by the available simulation outputs. Importantly, the PCF has increased at a slightly reduced rate to the EA%, leading to a favourable increase in the ratio of absorbed

energy/transmitted peak force load at 60 km/h. The G-Honeycomb achieved a 65.3% reduction in PCF at 40 km/h (2.53 MN vs. 7.30 MN for the conventional crash bar), and an even greater 73.9% reduction at 60 km/h (3.49 MN vs. 13.4 MN for the conventional crash bar). Therefore, the improved deformation characteristics, along with the topology driven resistance to localised failure, have been demonstrated to be consistent and even enhanced at higher dynamic loading conditions.

For the P-Honeycomb, the response to increasing impact velocity is anomalous. The energy absorption for the Primitive structure decreases with increasing velocity from 139.4 kJ at 40 km/h to 127 kJ at 60 km/h (DAR = 0.91). The peak crushing force for the Primitive structure decreases with increasing velocity from 13.4 MN to 7.04 MN (DAR = 0.53). The mean crushing force also decreases with increasing velocity from 3.45 MN to 1.90 MN (DAR = 0.55). For all cases, energy balance verification confirms that this trend is unlikely to be due to numerical artefact; the artificial energy to internal energy ratio was 0.26% for the 40 km/h case and 0.40% for the 60 km/h case, well below the 5% threshold. The total energy for the two simulations was constant to within 0.01%. The data for the Primitive structure suggests that the structure has undergone a velocity induced change in collapse mechanism. At low velocity the Primitive structure displayed partial progressive collapse with alternating load bearing behaviour, achieving a relatively high mean crushing force of 3.45 MN and high total energy absorption of 139.4 kJ. However, at high velocity the structure displayed a collapse mode transition occurring between the first and second folding, resulting in catastrophic localised buckling and bending leading to a premature loss of load carrying capacity. The structure achieved a low mean force of 1.90 MN and total energy absorption of 127 kJ.

The P-Honeycomb model accumulated 1,506 mesh warnings (approximately 0.95% of all elements), with the majority localising to the most highly curved regions of the geometry. These areas experience the largest post buckling distortion and at high velocity are highly susceptible to over stress and over distortion, potentially leading to loss of physical realism in the post peak load carrying capacity. A separate mesh refinement study would be required to quantify the relative contributions of this collapse mode transition, and the numerical issues due to the results. The lack of a strain rate sensitive material model for AA6061-T6 means that dynamic work hardening at higher strain rates is not included in the model, which would tend to increase both the peak

and mean crushing forces and energies. Consequently, the results obtained here provide only a lower bound estimate of these parameters. This is particularly significant at the higher strain rates associated with a design velocity of 60 km/h. As a result, it is likely that the anomalous velocity for the P-Honeycomb structure corresponds to a dynamically unstable fold rather than some unusual dynamic collapse characteristic. As such, confidence in the performance of the P-Honeycomb at multiple design velocities is limited.

The conventional crash bar had the worst velocity scaling in terms of PCF, with results increasing from 7.30 MN at 40 km/h to 13.4 MN at 60 km/h (DAR = 1.84), in marked contrast to the DAR for total energy absorption of 1.76. The local yielding mechanism of the cylinder wall was further exacerbated by the absence of an internal lattice. The impulsive load wave could not be transferred to other areas of the bar and was absorbed by a localised collapse that increased with velocity. While the total energy absorbed by the conventional crash bar did increase with velocity at a DAR of 1.76, the CFE of the conventional bar decreased from 0.21 at 40 km/h to 0.12 at 60 km/h, being the lowest CFE of any simulation. This CFE value corresponds to a peak force greater than eight times the mean force, showing that the conventional crash bar delivers virtually all of its resistance in a single brief single impulse and provides almost no resistance at other times. The local peak load transfer is 13.4 MN at 60 km/h reached within a displacement of 8.35 mm only. In the vehicle context this corresponds to a very high instantaneous deceleration of the vehicle front structure in the first few milliseconds after the first strike. This is exactly the parameter, which influences injury criteria such as chest acceleration and head injury criterion (HIC) in dynamic full scale test procedures according to present regulations. However, the slowly falling CFE of the conventional bar indicates that the weaknesses of its crashworthiness are by no means restricted to low speed. To the contrary, the weaknesses are increased and become more critical at higher speeds.

For the three architectural designs, the same performance hierarchy is observed for mass normalized safety performance at 40 and 60 km/h. Specifically, for energy absorption, The G-Honeycomb achieved the lowest PCF of 2.53 MN with the highest CFE of 0.58 at 40 km/h, with an SEA of 5.55 kJ/kg, which is 54% lower than that of the P-Honeycomb (10.3 kJ/kg), and 10% less than that of the conventional bar (6.1 kJ/kg). Notably, the mass of the G-Honeycomb (11.4 kg) was 12.9% greater than that of the

conventional crash bar (10.1 kg). However, the same volume of material can be used to absorb 9.6 kJ/kg of energy at 60 km/h, which is only 10.7% less than that of the conventional bar (10.75 kJ/kg). Moreover, the average PCF is reduced by 73.9% and the average CFE is increased by 283%. The performance of the Primitive specimen showed a similar SEA of 9.4 kJ/kg, but with the worst PCF of 7.04 MN and the lowest CFE of 0.27, which indicates that achieving high one-off performance of mass normalized energy absorption through catastrophic initial collapse is not sufficient to provide good crashworthiness performance. Using design requirements for suitable car crash components, a single metric (CFE) can be used to compare and rank the performance of different architectures. The results indicate that the Gyroid performed best achieving the highest CFE at both velocities for all orientations.

The findings presented here have some limitations, primarily due to the methodology adopted. The absence of strain rate hardening in the material model means the calculated forces represent lower-bound estimates, and the non-mass-equivalent structures mean SEA is used as the primary comparison metric rather than total EA. A full discussion of limitations is provided in Chapter 6.

6 CONCLUSION

In this thesis, a comprehensive numerical analysis was performed to evaluate the crashworthiness performance of two newly introduced TPMS inspired honeycomb crash bars: the G-Honeycomb and the P-Honeycomb. The performance of these two types of designs was compared with that of the conventional hollow cylindrical type. Numerical models of the three types of crash bars were designed and evaluated under dynamic impact loading at two automotive relevant testing speeds (40 km/h and 60 km/h). A comparative study was conducted to address five fundamental gaps in the current knowledgebase regarding the design of crashworthy components. Numerical experiments were performed using Abaqus/Explicit to compare the performance of the three designs under uniform test conditions. All three configurations were modelled using AA6061-T6 aluminium alloy.

Which topology results in the best crashworthiness performance? For the three performance criteria SEA, CFE and PCF, the best performance in terms of crush efficiency was achieved by the G-Honeycomb. The CFE achieved by the G-Honeycomb at 40 km/h was 0.58, with a moderate PCF of 2.53 MN and average SEA of 5.55 kJ/kg. At 60 km/h the CFE achieved was 0.46, with a PCF of 3.49 MN and average SEA of 9.6 kJ/kg. In contrast, the CFE achieved by the P-Honeycomb was significantly lower, with an extremely high initial peak force of 13.4 MN at 40 km/h and 7.04 MN at 60 km/h. The force history therefore includes an extremely high force spike that would result in an unacceptable instantaneous deceleration pulse in a real world crash event. Although the SEA achieved by the P-Honeycomb at 40 km/h of 10.3 kJ/kg is higher than that achieved by the G-Honeycomb, the results show that the collapse of the P-Honeycomb tested here results in highly localised and mechanically unstable behaviour that is not suitable as impact-responsive mechanical structure. Topology had the greatest influence on crashworthiness performance. The G-Honeycomb was found to be the optimal configuration among those studied for the design of automotive energy-absorbing crash bar components under the given boundary conditions.

Results were also compared based on the relative ranking of performance. The ranking for CFE and force management were both better for the G-Honeycomb at 60 km/h. In addition, the percent change in force due to energy was further improved for the G-Honeycomb with a PCF reduction relative to absorbed energy. The dynamic

amplification ratio (DAR) for the Energy Absorption (EA) of the G-Honeycomb increased moderately and consistently with a DAR of 1.73 between the two velocities. The DAR for SEA was likewise 1.73, reflecting favourable and predictable velocity scaling. The average increase factor for the PCF was 1.38, indicating a more moderate increase in force for the G-Honeycomb. In contrast, the P-Honeycomb structure exhibited an anomalous decrease in both EA and PCF with increasing velocity. The DAR for EA was 0.91, and the DAR for PCF was 0.53. This result indicated that there exists a velocity below which the P-Honeycomb structure undergoes a partially progressive folding collapse and a higher velocity above which it undergoes premature localised buckling. The results clearly show that the crashworthiness performance of the P-Honeycomb undergoes a change in collapse mechanism with increasing impact energy, and that quasi-static or low-rate results are insufficient to predict the performance of TPMS derived 2D structures at automotive crash velocities.

For the third research question, based on the above numerical results, the quantitative performance margins between the G-Honeycomb, P-Honeycomb, and the conventional crash bar are discussed. The results indicate that although the conventional crash bar achieved comparable SEA values to the G-Honeycomb and P-Honeycomb, it exhibited the poorest force efficiency with CFE values of 0.21 and 0.12 at 40 km/h and 60 km/h respectively. Most concerning is that the PCF for the conventional bar increased significantly with velocity, reaching 13.4 MN at 60 km/h compared to the initial value of 7.30 MN at 40 km/h. This is due to the localised bending and plastic hinge occurring in the hollow section of the conventional bar without the internal lattice achieving high SEA values through focused deformation in the central impact area and high impulsive forces transmitted to the vehicle structure in the first milliseconds of the crash event. In contrast, the results for the G-Honeycomb design were favourable from an occupant protection perspective, achieving lower SEA at 40 km/h and lower peak forces with higher force efficiency. Specifically, the SEA value of 9.6 kJ/kg achieved at 60 km/h represents a reduction of approximately 10.7% on the conventional bar result. The corresponding PCF for the G-Honeycomb was reduced by 73.9% compared to the conventional bar. The CFE for the G-Honeycomb was 0.46, which is significantly greater than that of the conventional bar (0.12).

Sequential von Mises stress contours and equivalent plastic strain (PEEQ) distributions are presented for the G-Honeycomb, P-Honeycomb, and conventional

crash bar samples tested at 40 km/h and 60 km/h. The deformation mechanisms of the G-Honeycomb arise from its cross-sectional geometry derived from the Gyroid level set equation, which contains no straight axial channels. This promotes the simultaneous deformation of multiple curved wall segments across the cross-section, leading to a well distributed stress field and stable progressive crushing. At 40 km/h, this mechanism resulted in a broadly distributed plastic strain field with low to moderate strain levels across the internal core. As velocity increased to 60 km/h, the same fundamental mechanism was preserved; however, the overall magnitude of strain increased while the distribution remained relatively uniform, demonstrating that the G-Honeycomb deformation mechanism is stable and consistent across the tested velocity range. In contrast, the P-Honeycomb exhibited early, high-stress concentrations at specific locations corresponding to the nodal junctions of its cross-sectional profile, resulting in sharp force spikes and a post peak load drop. At 40 km/h, this manifested as partial progressive collapse with alternating load bearing behaviour. At 60 km/h, the mechanism evolved into a catastrophic collapse mode transition between the first and second folding, resulting in premature loss of load carrying capacity and a significant reduction in both EA and PCF. The conventional crash bar sample produced the most localized response where significant plastic deformation occurred within a narrow band at the impact point, with most of the sample not participating in the crush test. With increasing velocity, this localised plastic hinge mechanism intensified, resulting in a disproportionate increase in PCF from 7.30 MN to 13.4 MN, while contributing no improvement in deformation distribution. These field-level analyses of the structural deformation mechanisms elucidate the mechanisms behind observed global differences in behaviour as extracted from force-displacement data, addressing one of the research gaps identified from the literature review.

Based on the available literature, this study presents the first direct, controlled computational comparison of G-Honeycomb, P-Honeycomb, and conventional crash bar geometries under identical automotive boundary conditions and impact loading at 40 km/h and 60 km/h, using AA6061-T6, the wrought aluminium alloy most widely employed in extruded automotive crash bars. The results from two vehicle speeds, 40 and 60 km/h, show that although the G-Honeycomb did not achieve the maximum mass-specific energy absorption for all cases, it performed the best in terms of force smoothing, stable deformation and overall crash management. Therefore, the G-

Honeycomb can be considered the preferred design solution among those studied for future automotive frontal impact applications where the protection of occupants and consistent, predictable response of critical vehicle structures are of utmost importance. The velocity dependent behaviour of the P-Honeycomb highlights the need to refine design methodologies for TPMS-derived 2D structures that rely solely on quasi static performance criteria when applied to automotive crash loading conditions.

This thesis describes a number of limitations, primarily that the employed material model is assumed to be rate independent elastic plastic, not capturing strain rate hardening for the employed material AA6061-T6, which would be expected to increase both peak and mean crushing forces by approximately 10-15% at the studied velocities. The model does not reflect real world structures, as no physical testing and fabrication was conducted. It is expected that the model produces lower-bound estimates for the structural resistance. The G-Honeycomb and P-Honeycomb are three dimensional in their overall crash bar geometry. However, their internal topology originates from 2D level set cross sectional profiles extruded longitudinally, rather than from a fully three dimensional level set implementation. This may result in a slight overestimation of axial stiffness relative to a true three dimensional TPMS lattice. The employed idealised CAD models do not incorporate any manufacturing defects. It is known that as built TPMS produced by Additive Manufacturing can have a significantly reduced performance, of 10-25% lower than the computational upper bounds reported. The results presented in this thesis, therefore, provide upper bounds to the performance that can be expected from such structures. No effect of fracture initiation was included, nor were any thermal or oblique load effects assessed. Also, no full vehicle system level effects were considered.

Several additional avenues can be pursued in future work to enhance the scope and applicability of the current study. A strain-rate sensitive constitutive model (e.g. Johnson Cook, Cowper Symonds) with proper calibration of material constants for the AA6061-T6 material should be incorporated into the finite element simulations to obtain absolute EA and PCF predictions for on-road automotive impacts. To further validate the simulation-based results, G-Honeycomb and P-Honeycomb crash bar cores or their fully three dimensional TPMS equivalents can be fabricated by laser powder bed fusion and subjected to drop tower and/or sled impact tests. In addition to the in-line (off-axis) performance, the current design can be tested under oblique and multi-axial

loading conditions typical of non-standard design configurations for crash worthy applications. Functionally graded and hybrid G-Honeycomb and P-Honeycomb designs in which the cross-sectional density or topology varies along the crash bar length can be considered to further enhance the CFE beyond the results obtained in the uniform relative density study presented herein. In addition, the combination of surrogate modelling and multi objective optimisation methods could enable efficient numerical exploration of the TPMS derived 2D structural design space across different topological, dimensional, and material parameters relevant to automotive crashworthiness.

References

Abueidda, D. W., Elhebeary, M., Shiang, C.-S. (Andrew), Pang, S., Abu Al-Rub, R. K., & Jasiuk, I. M. (2019). Mechanical properties of 3D printed polymeric Gyroid cellular structures: Experimental and finite element study. *Materials & Design*, *165*, 107597. https://doi.org/10.1016/j.matdes.2019.107597

AlMahri, S., Santiago, R., Lee, D.-W., Ramos, H., Alabdouli, H., Alteneiji, M., Guan, Z., Cantwell, W., & Alves, M. (2021). Evaluation of the dynamic response of triply periodic minimal surfaces subjected to high strain-rate compression. *Additive Manufacturing*, *46*, 102220. https://doi.org/10.1016/j.addma.2021.102220

Ashby, M. F. (2006). The properties of foams and lattices. *Philosophical Transactions of the Royal Society A: Mathematical, Physical and Engineering Sciences*, *364*(1838), 15–30. https://doi.org/10.1098/rsta.2005.1678

Bahrami Babamiri, B., Askari, H., & Hazeli, K. (2020). Deformation mechanisms and post-yielding behavior of additively manufactured lattice structures. *Materials & Design*, *188*, 108443. https://doi.org/10.1016/j.matdes.2019.108443

Boulbes, R. J. (2020). *Troubleshooting Finite-Element Modeling with Abaqus: With Application in Structural Engineering Analysis*. Springer International Publishing. https://doi.org/10.1007/978-3-030-26740-7

Cai, Z., Wu, J., & Deng, X. (2025). Mechanical properties and deformation behavior of triply periodic minimal surface lattices under quasi-static compression and low-to-medium velocity impact loads. *Mechanics of Advanced Materials and Structures*, *0*(0), 1–18. https://doi.org/10.1080/15376494.2025.2494241

Dagdeviren, S., Yavuz, M., Kocabas, M. O., Unsal, E., & Esat, V. (2016). Structural crashworthiness analysis of a ladder frame chassis subjected to full frontal and pole side impacts. *International Journal of Crashworthiness*, *21*(5), 477–493. https://doi.org/10.1080/13588265.2015.1135522

Demirci, H. E., Bhattacharya, S., Karamitros, D., & Singh, R. M. (n.d.). *FINITE ELEMENT MODEL OF BURIED PIPELINES CROSSING STRIKE-SLIP FAULTS BY ABAQUS/EXPLICIT*.

European Commission. (2023, October 19). *Road safety: 20,640 people died in a road crash last year – progress remains too slow*. European Commission. European Commission – Mobility and Transport. https://transport.ec.europa.eu/news-events/news/road-safety-20640-people-died-road-crash-last-year-progress-remains-too-slow-2023-10-19_en

European Commission / European Road Safety Observatory. (2023). *Road Safety Thematic Report – Consequences of Crashes*. European Commission, Directorate-General for Transport. https://road-safety.transport.ec.europa.eu/system/files/2023-03/Road_Safety_Thematic_Report_Consequences_of_crashes_2023.pdf

Global Status Report on Road Safety 2023 (1st ed). (2023). World Health Organization.

Guo, X., Zheng, X., Yang, Y., Yang, X., & Yi, Y. (2019). Mechanical behavior of TPMS-based scaffolds: A comparison between minimal surfaces and their lattice structures. *SN Applied Sciences*, *1*. https://doi.org/10.1007/s42452-019-1167-z

Hossain, M. S., Hossain, M. M., & Nilufar, S. (2025). An Overview of Additive Manufacturing of Triply Periodic Minimal Surface (TPMS) Structures. *Polymers*, *17*(24), 3307. https://doi.org/10.3390/polym17243307

Jackowski, J., Posuniak, P., Zielonka, K., & Jurecki, R. (2023). Experimental Testing of Energy-Absorbing Structures Used to Enhance the Crashworthiness of the Vehicles. *Energies*, *16*(5), 2183. https://doi.org/10.3390/en16052183

Liang, Y., He, H., Yin, J., Huang, J., Wu, Z., Yao, X., & Liu, Y. (2024). Dynamic compressive behavior of functionally graded triply periodic minimal surface cellular structures. *Engineering Structures*, *312*, 118260. https://doi.org/10.1016/j.engstruct.2024.118260

Liu, Q., Li, W., Zhu, L., Gao, Y., Xing, L., Duan, Y., & Ke, L. (2022). Temperature-dependent friction coefficient and its effect on modeling friction stir welding for aluminum alloys.

Journal of Manufacturing Processes, *84*, 1054–1063. https://doi.org/10.1016/j.jmapro.2022.10.068

L.J. Gibson and M.F. Ashby, Cellular solids: Structure & properties, Oxford: Pergamon Press, ISBN: 0-08-036607-4, 1988, 357 + ix pages, $35.00. (1989). *Advances in Polymer Technology*, *9*(2), 165–166. https://doi.org/10.1002/adv.1989.060090207

Ma, X., & Guo, C. (2024). Dynamic compressive behavior of functionally graded triply periodic minimal surface meta-structures. *Thin-Walled Structures*, *205*, 112544. https://doi.org/10.1016/j.tws.2024.112544

Maskery, I., Aboulkhair, N. T., Aremu, A. O., Tuck, C. J., & Ashcroft, I. A. (2017). Compressive failure modes and energy absorption in additively manufactured double gyroid lattices. *Additive Manufacturing*, *16*, 24–29. https://doi.org/10.1016/j.addma.2017.04.003

MatWeb LLC. (2024). *Aluminum 6061-T6; 6061-T651*. MatWeb Material Property Data. https://www.matweb.com/errorUser.aspx?msgid=8

Novak, N., Tanaka, S., Hokamoto, K., Mauko, A., Yilmaz, Y. E., Al-Ketan, O., Vesenjak, M., & Ren, Z. (2023). High strain rate mechanical behaviour of uniform and hybrid metallic TPMS cellular structures. *Thin-Walled Structures*, *191*, 111109. https://doi.org/10.1016/j.tws.2023.111109

Ogmaia, D., & Tasel, S. E. T. (2015). *Simulation of vehicle crash into bridge parapet using Abaqus/Explicit*. https://urn.kb.se/resolve?urn=urn:nbn:se:kth:diva-169436

Özen, İ., & Aslan, M. (2023). Investigation of Energy Absorbing and Damage Behavior of Gyroid and Diamond Cell Based Lattice Structures Manufactured through Powder Bed Fusion Technology. *International Journal of Automotive Science and Technology*, *7*(4), 372–383. https://doi.org/10.30939/ijastech..1360762

Özen, İ., Çava, K., İpek, H., Sezer, R., & Aslan, M. (2024). Crushing response of triply periodic minimal surface structures fabricated by investment casting and powder bed fusion method. *Materials Today Communications*, *38*, 107638. https://doi.org/10.1016/j.mtcomm.2023.107638

Peng, C., Marzocca, P., & Tran, P. (2023). Triply periodic minimal surfaces based honeycomb structures with tuneable mechanical responses. *Virtual and Physical Prototyping*, *18*(1), e2125879. https://doi.org/10.1080/17452759.2022.2125879

Rapaka, S. D., Pandey, M., & Annabattula, R. K. (2021). Theoretical analysis on the dynamic compressive behavior of cellular solids with non-linear variation in cross-sectional area. *International Journal of Impact Engineering*, *155*, 103921. https://doi.org/10.1016/j.ijimpeng.2021.103921

Rezapourian, M., Darabi, A. C., Khoshbin, M., Schmauder, S., & Hussainova, I. (2025). Surrogate-Model Prediction of Mechanical Response in Architected Ti6Al4V Cylindrical TPMS Metamaterials. *Metals*, *15*(12), 1372. https://doi.org/10.3390/met15121372

Sebaey, T. A. (2020). Effect of Exposure Temperature on the Crashworthiness of Carbon/Epoxy Composite Rectangular Tubes Under Quasi-Static Compression. *Polymers*, *12*(9), 2028. https://doi.org/10.3390/polym12092028

Shinde, M., Ramirez-Chavez, I. E., Anderson, D., Fait, J., Jarrett, M., & Bhate, D. (2022). Towards an Ideal Energy Absorber: Relating Failure Mechanisms and Energy Absorption Metrics in Additively Manufactured AlSi10Mg Cellular Structures under Quasistatic Compression. *Journal of Manufacturing and Materials Processing*, *6*(6), 140. https://doi.org/10.3390/jmmp6060140

Sombatmai, A., Tapracharoen, K., Uthaisangsuk, V., Msolli, S., & Promoppatum, P. (2024). Post-yielding and failure mechanism of additively manufactured triply periodic minimal surface lattice structures. *Results in Engineering*, *23*, 102364. https://doi.org/10.1016/j.rineng.2024.102364

Sun, L. L., Milenkovski, N., Awasthi, K., Nghiem, X. B., Mongelli, N., Kirchner, E., & Mittelstedt, C. (2025). Design and Comparative Numerical Analysis of AlSi10Mg PBF-LB/M Manufactured TPMS Lattice Structures for Improved Mechanical Performance. *Materials*, *18*(21), 4934. https://doi.org/10.3390/ma18214934

Wagner, J., Hall, J., Billings, C., & Liu, Y. (2025). Comparison of Compressive Properties of 3D-Printed Triply Periodic Minimal Surfaces and Honeycomb Lattice Structures. *Journal of Composites Science*, *9*(11), 586. https://doi.org/10.3390/jcs9110586

Wan, L., Hu, D., Wan, M., Yang, Z., Zhang, H., & Pi, B. (2023). Lateral crushing behavior of tubular lattice structures with triply periodic minimal surface architectures. *Thin-Walled Structures*, *189*, 110905. https://doi.org/10.1016/j.tws.2023.110905

Xia, P., Liu, Q., Fu, H., Yu, Y., Wang, L., Wang, Q., Yu, X., & Zhao, F. (2023). Mechanical properties and energy absorption of 3D printed double-layered helix honeycomb under in-plane compression. *Composite Structures*, *315*, 116982. https://doi.org/10.1016/j.compstruct.2023.116982

Yin, H., Liu, Z., Dai, J., Wen, G., & Zhang, C. (2020). Crushing behavior and optimization of sheet-based 3D periodic cellular structures. *Composites Part B: Engineering*, *182*, 107565. https://doi.org/10.1016/j.compositesb.2019.107565

Yılmaz, Y. E., Novak, N., Al-Ketan, O., Erten, H. I., Yaman, U., Mauko, A., Borovinsek, M., Ulbin, M., Vesenjak, M., & Ren, Z. (2024). Mechanical Behaviour of Photopolymer Cell-Size Graded Triply Periodic Minimal Surface Structures at Different Deformation Rates. *Materials*, *17*(10), 2318. https://doi.org/10.3390/ma17102318

Yu, S., Sun, J., & Bai, J. (2019). Investigation of functionally graded TPMS structures fabricated by additive manufacturing. *Materials & Design*, *182*, 108021. https://doi.org/10.1016/j.matdes.2019.108021

Zhang, X., Yan, S., Xie, X., Li, Y., Wang, C., & Wen, P. (2024). Multi-dimensional hybridized TPMS with high energy absorption capacity. *International Journal of Mechanical Sciences*, *273*, 109244. https://doi.org/10.1016/j.ijmecsci.2024.109244

Zhou, H., Zhao, M., He, N., Zhang, T., Ma, X., & Zhang, D. Z. (2024). Compressive response and energy absorption of additive manufactured Ti-6Al-4V triply periodic minimal surface honeycomb structure. *Journal of Alloys and Compounds*, *982*, 173744. https://doi.org/10.1016/j.jallcom.2024.173744